

International Journal of Thermodynamics

Editor-in-Chief

L. Kuddusi

Honorary Editors

A. Bejan

M. J. Moran

J. Szargut

G. Tsatsaronis

A. Valero

M. R. von Spakovsky

Abstracting and Indexing:

Chemical Abstracts Services, Copernicus, DOAJ, EBSCO, Emerging Sources Citation Index, Engineering Index, Google Scholar, Scopus, and ULAKBIM



*International Centre for
Applied Thermodynamics*

Editor-in-Chief

Prof. Dr. Lütfullah KUDDUSİ

Associate Editor-in-Chief

Assoc. Prof. Dr. Patrice ESTELLÉ

Prof. Dr. Enrico SCIUBBA

Associate Editor

Prof. Dr. Ali KOSAR

Prof. Dr. Derya Burcu ÖZKAN

Prof. Dr. Mustafa ÖZDEMİR

Prof. Dr. Ahmet DURMAYAZ

Assoc. Prof. Dr. Onur TAYLAN

Prof. Dr. Mehmet ARİK

Prof. Dr. Ayşegül ABUŞOĞLU

Prof. Dr. G. Reza VAKİLİ-NEZHAAD

Prof. Dr. Bayram ŞAHİN

Assoc. Prof. Dr. Murat ÇAKAN

Editorial Board

Prof. Dr. Yasar DEMİREL

Prof. Dr. Lütfullah KUDDUSİ

Prof. Dr. Ahmet DURMAYAZ

Prof. Dr. Derya Burcu ÖZKAN

Prof. Dr. Mustafa ÖZDEMİR

Prof. Dr. Ali KOSAR

Prof. Dr. Mehmet ARİK

Assoc. Prof. Dr. Abdussamet SUBASI

Prof. Dr. Daniel FAVRAT

Prof. Silvia Azucena NEBRA

Prof. Dr. Luis SERRA

Assoc. Prof. Dr. Onur TAYLAN

Prof. Dr. Francois MARECHAL

Prof. Dr. Gian Paolo BERETTA

Prof. Dr. Ayşegül ABUŞOĞLU

Prof. Dr. Abel HERNANDEZ-GUERRERO

Prof. Dr. Silvio DE OLIVEIRA JUNIOR

Prof. Dr. Sean WRIGHT

Prof. Dr. Nilufer EGRİCAN

Prof. Dr. G. Reza VAKİLİ-NEZHAAD

Prof. Dr. Bayram ŞAHİN

Prof. Dr. Vittorio VERDA

Assoc. Prof. Dr. Murat ÇAKAN

Publishing Editor

Assoc. Prof. Dr. Abdussamet SUBASI

Assist. Prof. Dr. Mustafa Yasin GÖKASLAN

Res. Assist. Ali Murat BİNARK

Res. Assist. Kasım ERDEM

Language Editor

Assoc. Prof. Dr. Abdussamet SUBASI

Journal Contacts

Editor-in-Chief

Prof. Dr. Lütfullah Kuddusi

ISTANBUL TECHNICAL UNIVERSITY

kuddusi@itu.edu.tr

*Department of Mechanical Engineering
Istanbul Technical University
Gumussuyu, 34437 Istanbul Turkey*

Volume: 28

Issue: 1

Web: <https://dergipark.org.tr/tr/pub/ijot>

International Journal of Thermodynamics (IJoT)

ISSN:1301-9724 / e-ISSN:2146-1511

International Journal of Thermodynamics

<https://dergipark.org.tr/tr/pub/ijot>

ISSN 1301-9724 / e-ISSN 2146-1511

Volume: 28 / No: 1 – March / 2025

CONTENTS

Research Article

1. Excess Molar Viscosities and Excess Molar Gibbs Energies of The Mixtures of Tire Pyrolytic Oil + Diesel Fuel at 293.15 K and 303.15 K 1-6

U. S. Vural

Research Article

2. Exact Thermodynamic Solution of Gas Behavior in Propellant Tanks and Storage Capsules During Pressurization 7-16

M. Mohseni

Research Article

3. 3E Analysis of a Hybrid Biomass / Solar System for Power Generation and Desalination 17-28

E. M. Leal, E. A. Teixeira

Research Article

4. General Thermodynamically Unification of the First and Second Laws of Thermodynamics 29-34

S. Shahsavari, S. M. A. Boutorabi

Research Article

Excess Molar Viscosities and Excess Molar Gibbs Energies of The Mixtures of Tire Pyrolytic Oil + Diesel Fuel at 293.15 K and 303.15 K

*U. S. Vural 

¹Selcuk University, Faculty of Science, Department of Chemistry (Retired)
E-mail: *usvural@gmail.com

Received 14 September 2023, Revised 7 February 2024, Accepted 26 March 2024

Abstract

Diesel-like fuel mixtures are obtained by blending the pyrolytic oil obtained from the pyrolysis of tires and diesel fuel. The excess thermodynamic properties of blended fuel mixtures give a preliminary idea about the transport, storage and combustion properties of the fuel mixture. In this study, pyrolytic oil and diesel fuel were mixed in different proportions at temperatures of 293.15 K and 303.15 K and their excess molar properties were determined. A positive deviation was observed in the excess molar volume and excess molar Gibbs energy values of the two-component mixture, and a negative deviation was observed in the excess molar viscosity values. Volumetric expansion and flow rate of the mixture were found to be higher at 303.15 K. It has been observed that at low pyrolytic oil concentrations, dispersive and physical forces are dominant between molecules, while at high pyrolytic oil concentrations, π - π interactions are more dominant for the molecules.

Keywords: *Excess molar; Gibbs energy; viscosity; molar volume; tire derived fuel; diesel.*

1. Introduction

In parallel with the increase in tire production worldwide, the amount of scrap tires is also increasing. Scrap tires are a type of waste that threatens biological life and pollutes the atmosphere as a result of fire [1]. Pyrolysis technique has recently started to gain importance among the methods of reducing scrap tires [2-3]. Thermal cracking of hydrocarbons under oxygen-free conditions is called pyrolysis, and as a result of pyrolysis of tires, 35-50% pyrolytic oil (TPO), 30-40% pyrolytic carbon black (CBp) and 10-15% non-condensed gases are obtained [4,5]. Pyrolytic oil is a type of fuel rich in aromatic compounds, somewhat similar to diesel, with a high calorific value [5]. Pyrolytic oils obtained from the pyrolysis of tires or mixtures of TPO and known fuels, which meet the energy requirements of transportation vehicles and industry, are generally called tire derived fuel (TDF) [6-7]. Remarkable research has been carried out on the use of fuel obtained by blending a certain amount of pyrolytic oil and diesel fuel (DF) in diesel vehicles. Hamzah et al. blended TPO and diesel fuel at a ratio of 10%-50% and tested it in a single-cylinder diesel engine operating at 1200-2400 rpm [6]. They obtained the highest performance values in the 10% TPO mixture, and observed that as the TPO ratio increased, the exhaust gas temperature, engine power and torque, and gas combustion pressure decreased. Mohan et al. purified crude pyrolytic oil with petroleum ether and silica gel and stated that a mixture of 50% diesel, 40% upgraded TPO and 10% ethyl levulinate showed the best performance and emission values in single-cylinder diesel engines [7]. Mia et al. fractionally distilled TPO and subjected it to desulfurization and color removal processes [8]. They found that the fraction between 40°C and 120°C was similar to kerosene, while other fractions differed from diesel fuel.

Vural et al. succeeded in obtaining diesel-like fuel by using advanced purification techniques in catalytic pyrolysis experiments [5]. From these studies, it is understood that crude pyrolytic oil can be mixed with diesel fuels in certain proportions with simple purification techniques.

The excess molecular properties of fuel mixtures are very useful for understanding the conformational stability and unfolding behavior of molecules [9]. Determining the volumetric and some thermodynamic properties of the fuel mixture is important in terms of giving an idea about the transportation and ignition and combustion of the fuel mixture. Excess properties can be defined as the difference between the ideal volumetric properties of the mixture and the observed volumetric properties as a result of the molecular interactions between the components that make up the mixture and in the solution [9,10]. The excess volumes (V^E) are defined as volume of real solutions - volume of pure components (ideal solution). Excess thermodynamic properties, which can also be understood as deviations from ideal thermodynamic behaviors, provide a better understanding of the behavior of components in chemical and physicochemical events, and their roles in production and application processes. In general, the excess properties result from three types of interactions between the constituent molecules of liquid mixtures [9,11,12].

- *Positive effects:* Physical interactions consisting of dispersion forces or weak dipole-dipole interaction,
- *Negative effects:* chemical or specific interactions, including charge transfer, H-bonds, and other complex formation interactions, and
- *Structural effects:* These are the structural contributions arising from the differences in the size and shape of the

component molecules in the mixture depending on the structure of their molecules.

In this study, some excess molar properties of the mixture of upgraded pyrolytic oil (*UTPO*) and diesel fuel (*DF*) were investigated at 293.15 K and 303.15 K. It was observed that unstable, weak physical interactions occurred in the mixture due to the increase in temperature, and no chemical interactions occurred between the molecules.

2. Material and Methods

Scrap tire crumbs, 1-2 cm in size, were obtained from the local recycling company. Diesel fuel was obtained from local Lukoil fuel sales point. Some physicochemical properties of the components are given in Table 1. In previous pyrolysis experiments, researchers stated that thermal cracking reactions were largely completed at 450°C, and that the thermal cracking rate decreased between 450°C and 550°C [13,14]. In this study, asphaltenes, organic residues, carbon and water were removed from the pyrolytic oil by the adsorption method without using advanced purification techniques such as distillation, desulfurization and chemical refining.

2.1. Tire Pyrolysis

300 g of tire crumbs were put into a 1000 mL balloon connected to a condenser and thermometer. It was heated to 450°C with a jacketed heater. Pyrolytic gases were passed through the condenser and 120 mL of pyrolytic oil was obtained.

2.2. Upgraded Pyrolytic Oil (UTPO)

10 g of acid-active bentonite was added to the pyrolytic oil, stirred at 50°C for half an hour and filtered. 10 g of silica gel was added, stirred at 50°C for half an hour and filtered again. Thus, 100 mL of upgraded pyrolytic oil (*UTPO*) was obtained by removing water, carbon residues and polymeric impurities (Figure 1).

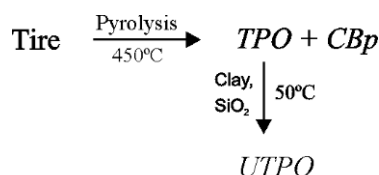


Figure 1. Tire pyrolysis and upgrade of TPO.

2.3. Fuel Blends

Fuel mixtures were prepared as $v_{UTPO} + (10 - v_{UTPO})$ by volume, increasing 1 mL of *UTPO*, making a total of ten pieces of 10 mL each. The sample tubes were mixed with a magnetic stirrer for 5 min at room temperature by closing the mouth with a Teflon cap. Then, the supernatant in the mixtures was separated by filtration. The filtered solutions were kept in a thermostatic water bath at 293.15±0.1 K and 303.15±0.1 K.

2.4. Density and Viscosities of Fuel Blends

The densities of fuel blends were measured by Anton Paar DMA 35N Denismeter. Calibration of the density meter was performed in four replicates with triple distilled water. It was measured as 1.9980 g/cm³ at 20°C and is compatible with the literature [15]. Kinematic viscosity measurements were made with an Ostwald viscometer. The viscometer was calibrated with toluene. The viscosity of spectroscopically pure toluene was measured as 0.5858 mPa·s at 20°C, in

accordance with the literature [16]. Four replicate flow times were measured for each sample and the arithmetic mean was used for calculations. The repeatability of viscosity measurements was 0.005 mPa·s. The samples were placed in the viscometer and the viscometer was immersed in the thermostatic bath kept constant at a temperature of 293.15 K and 308.15 K, respectively. The viscometer was left for 15 min for its content to reach thermal equilibrium. Flow time was measured with a stopwatch to an accuracy of 10⁻² seconds. Dynamic viscosity values were calculated from kinematic viscosity using measured density values (v/d).

Table 1. Some physical parameters of *DF*, *UTPO* and *TPO*.

| Properties | <i>TPO</i> | <i>UTPO</i> | <i>DF</i> |
|----------------------------|------------------|-------------|------------------|
| Density, g/cm ³ | 0.9123 | 0.9056 | 0.8256 |
| Viscosity, mPa·s | 4.7842 | 4.3319 | 3.1819 |
| Molar mass, g/mol | 430 ^a | - | 280 ^b |

^a[17], ^b[18]

2.5. Calculation of Excess Molar Properties

Excess molar properties of a liquid solution are defined by the following equation [19]:

$$Y^E = Y - \sum_{i=0} x_i Y_i^0 \quad (1)$$

where Y^E is excess molar properties of the solution, y is the molar properties of the solution, x_i is the mole fractions of components, and Y_i is the molar properties of pure components, respectively. Eq 1 is written as Eq .2 for excess molar volume (V^E).

$$V^E = \sum_{i=1} x_i M_i \left(\frac{1}{\rho} - \frac{1}{\rho_i} \right) \quad (2)$$

in which M_i is the molar masses of components, ρ is the density of the mixture, and ρ_i is represent the densities of pure components, respectively. The excess molar properties (Y^E) can be correlated using the Redlich–Kister equation [19]:

$$Y^E = x_i (1 - x_i) \sum_{i=0} A_i (2x_i - 1)^i \quad (3)$$

The values of the coefficient A_i were calculated by method of least squares along with the standard deviation $\sigma(Y^E)$. The coefficients A_i are adjustable parameters for a better fit of the excess functions. The standard deviations, $\sigma(Y^E)$, calculated by using Eq. (4):

$$\sigma(Y^E) = \left[\frac{\sum_{i=1}^{i=n} (Y_{cal,i}^E - Y_{exp,i}^E)^2}{n-p} \right]^{1/2} \quad (4)$$

where n is the number of experimental data points, p is the number of parameters, Y_{exp} and Y_{cal} are the experimental and calculated parameters, respectively. In this study, the density and excess molar properties of the mixture of $x_{UTPO} + (1-x) DF$ at 293.15 K and 303.15 K were investigated. The densities of the mixtures over the entire range of compositions at temperatures of 293.15 K and 303.15 K are listed in Table 2. Matlab 2021b was used to calculate the coefficients of polynomial equations and draw graphs.

3. Result and Discussions

Diesel fuel consists of 72% branched alkanes, 10% saturated cycloalkanes, 8-9% alkylbenzenes, 5% alkylated *PAHs* and low amounts of *PAHs*, aromatic acids and

alkanoic acids [20]. Most of diesel fuel has a stable linear alkane structure. *TPO* structure contains 49.54% aliphatic compounds and 16.65% aromatic compounds [21,22]. The largest fraction of aromatic compounds in *TPO* are limonene and monoaromatic compounds. Monoaromatic compounds are more reactive and mobile than polyaromatic compounds. Limonene also has aromatic π -electrons and an unsaturated $-C=C-$ bond. Since *UTPO* contains monoaromatic components that make intramolecular bonds with π -electrons, the electronegativity of *DF*, which contains a larger amount of aliphatic and polynuclear aromatic components, is higher than *UTPO*.

The excess molar volumes of the binary mixtures of $xUTPO + (1-x)DF$ were calculated from Eq. (2) over the entire composition range and at $T=293.15$ K and 303.15 K, and given in Table 2. The density values of the binary mixture increases depending on the increase in *UTPO* concentration. Since both components contain highly stable alkane molecules, there was no significant increase in the volumetric expansion of the mixture with a 10°C increase in temperature, and a slight decrease in density values was observed. As seen in Figure 2, a positive deviation was observed in the V^E values of the binary mixture. The backbone of *DF* has a more stable structure than *UTPO* due to its cycloalkane and alkane structures containing strong C-C bonds. *UTPO*, which contains more π -electrons such as monoaromatic components and limonene, has an electron donor character. Additionally, strong intramolecular π - π bonds (charge-transfer bonds) occur between π -electrons of monoaromatic molecules and limonene in the *UTPO*. As seen in Figure 3, limonene also contains an alkene molecule ($-C=C-$) in addition to aromatic π -electrons. As seen in Figure 3, electrons on the aromatic structure can be easily dispersed, and π -electrons in parallel, eclipsed or T-shaped edge to face aromatic planes form strong dipole interactions [23]. The reason for the positive deviation in V^E values at low *UTPO* concentrations is the dipole interactions between *UTPO*, which consists of smaller molecules, and *DF*, which has polyaromatic compounds. When *UTPO* concentration increases, due to the π -electrons localized on *UTPO* molecules, strong intramolecular bonds are formed between the monoaromatic components in *UTPO*. In the *UTPO*+*DF* mixture, when the *UTPO* concentration is more than 50%, the positive deviation in V^E values decreases because the intramolecular chemical interactions of *UTPO* become stronger than the intermolecular physical interactions between *UTPO* and *DF*. No significant volumetric expansion of the mixture was observed at a temperature increase of 10°C due to the intramolecular bonds of *UTPO*, which are stronger than the dipole interaction between *DF* and *UTPO* molecules. However, it is possible to say that at higher temperatures, volumetric expansion will become more pronounced as intramolecular π - π interactions will weaken. Figure 2 show the excess molar volumes calculated from experimental data and Redlich–Kister equation. Redlich–Kister equation coincided with the experimental results in great agreement.

Dynamic viscosities (η) of the mixtures of *UTPO* and *DF* at 293.15 and 303.15 K were calculated by the measured densities and kinematic viscosities. The viscosity deviation was calculated [19] by Eq. (5) are given in Table 3.

$$\Delta\eta = \eta - \sum x_i \eta_i \quad (5)$$

where η is the viscosities of the mixture and x_i and η_i are the mole fraction and the viscosities of pure components, respectively. The Redlich–Kister equation given in Eq. (3) is written in terms of viscosity as in Eq. (6). The Redlich–Kister coefficients in Eq. (6) were calculated by the least squares method and are given in Table 4.

$$\eta^E = x_i(1 - x_i) \sum_{i=1} A_i (2x_i - 1)^i \quad (6)$$

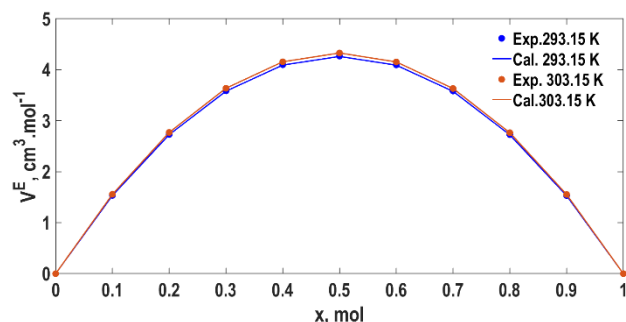


Figure 2. The experimental and calculated excess molar volume of the mixture of $xUTPO+(1-x)DF$ at 293.15 K and 303.15 K.

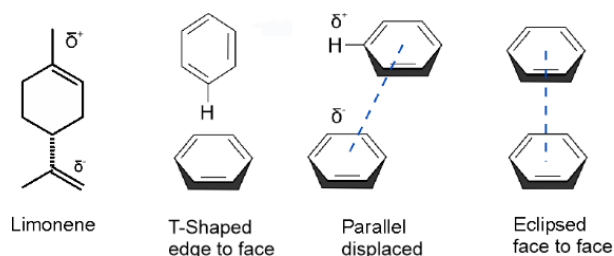


Figure 3. π -electrons interactions according to the geometry of the aromatic structure.

Table 2. Densities, viscosities, excess molar volume, of the mixture of $xUTPO+(1-x)DF$ at 293.15 K and 303.15 K.

| X | 293.15 K | | | 303.15 K | | |
|-----|----------------------------|----------------|------------------------------|----------------------------|----------------|------------------------------|
| | ρ , g/cm ³ | η , mPa.s | V^E , cm ³ /mol | ρ , g/cm ³ | η , mPa.s | V^E , cm ³ /mol |
| 0.0 | 0.8256 | 3.1819 | 0.0000 | 0.8189 | 2.6621 | 0.0000 |
| 0.1 | 0.8327 | 3.2699 | 1.5358 | 0.8260 | 2.6961 | 1.5578 |
| 0.2 | 0.8400 | 3.3639 | 2.7319 | 0.8333 | 2.7381 | 2.7710 |
| 0.3 | 0.8475 | 3.4639 | 3.5869 | 0.8408 | 2.7881 | 3.6379 |
| 0.4 | 0.8552 | 3.5699 | 4.0998 | 0.8485 | 2.8461 | 4.1578 |
| 0.5 | 0.8631 | 3.6819 | 4.2701 | 0.8564 | 2.9121 | 4.3302 |
| 0.6 | 0.8712 | 3.7999 | 4.0979 | 0.8645 | 2.9861 | 4.1552 |
| 0.7 | 0.8795 | 3.9239 | 3.5837 | 0.8728 | 3.0681 | 3.6335 |
| 0.8 | 0.8880 | 4.0539 | 2.7283 | 0.8813 | 3.1581 | 2.7660 |
| 0.9 | 0.8967 | 4.1899 | 1.5331 | 0.8900 | 3.2561 | 1.5542 |
| 1.0 | 0.9056 | 4.3319 | 0.0000 | 0.8989 | 3.3621 | 0.0000 |

The reason for viscosity deviation depends on two factors [19]. (1) The difference in size and shape of the molecules and the loss of dipolar coupling cause the viscosity to decrease. (2) Specific interactions between components, such as hydrogen bonding and charge-transfer complexes, cause the viscosity of the mixture to increase.

As seen in Figure 4, the viscosity decreases as the *UTPO* concentration increases up to 50%. *UTPO* at low concentrations, consisting of smaller molecules, is easily dispersed in *DF*. As the *UTPO* concentration increases, the dispersion of *UTPO* in diesel becomes difficult and the viscosity begins to increase, since the π -electron density and intramolecular π - π bonds in *UTPO* increase. It has been understood that dispersive and physical forces (dipole interactions) are effective in decreasing the viscosity of the

mixture up to 50% *UTPO* concentration, and intramolecular charge-transfer bonds (chemical interactions) are effective in increasing the viscosity at higher *UTPO* concentrations. As the temperature increases, the density of localized π -electrons on the aromatic structure in *UTPO* decreases, and the freer *UTPO* molecules are more easily dispersed within the *DF*.

Table 3. The excess molar viscosities and excess molar Gibbs energies of the binary mixture of $xUTPO+(1-x)DF$ at 293.15 K and 303.15 K.

| x | 293.15 K | | 303.15 K | |
|-----|------------------------|-------------------------|------------------------|-------------------------|
| | $\Delta\eta^E$, mPa.s | ΔG^{*E} , J/mol | $\Delta\eta^E$, mPa.s | ΔG^{*E} , J/mol |
| 0.0 | 0.0000 | 0.0000 | 0.0000 | 0.0000 |
| 0.1 | -0.0270 | 0.0061 | -0.0360 | 0.0010 |
| 0.2 | -0.0480 | 0.0106 | -0.0640 | 0.0019 |
| 0.3 | -0.0630 | 0.0136 | -0.0840 | 0.0026 |
| 0.4 | -0.0720 | 0.0152 | -0.0960 | 0.0030 |
| 0.5 | -0.0750 | 0.0156 | -0.1000 | 0.0031 |
| 0.6 | -0.0720 | 0.0147 | -0.0960 | 0.0029 |
| 0.7 | -0.0630 | 0.0127 | -0.0840 | 0.0024 |
| 0.8 | -0.0480 | 0.0096 | -0.0640 | 0.0017 |
| 0.9 | -0.0270 | 0.0053 | -0.0360 | 0.0009 |
| 1.0 | 0.0000 | 0.0000 | 0.0000 | 0.0000 |

Table 4. A coefficients and $\sigma(Y^E)$ values in the Redlich and Kister equation.

| Parameter | V^E , cm ³ /mol | 293.15 K | |
|---------------|------------------------------|------------------------|-------------------------|
| | | $\Delta\eta^E$, mPa.s | ΔG^{*E} , J/mol |
| A0 | 1.71E+01 | -0.2971 | 0.06298 |
| A1 | -1.93E-02 | -1.28E-09 | -5.22E-03 |
| A2 | -4.83E-02 | 2.09E-08 | 2.65E-03 |
| A3 | 1.17E-03 | 8.51E-09 | -4.20E-04 |
| $\sigma(Y^E)$ | 1.90E-02 | 1.81E-03 | 5.13E-04 |
| 303.15 K | | | |
| A0 | 1.73E+01 | -3.96E-01 | 0.01282 |
| A1 | -2.69E-02 | 2.32E-08 | -1.28E-03 |
| A2 | -4.94E-02 | 7.64E-08 | -3.48E-03 |
| A3 | 2.82E-03 | -3.50E-08 | 8.14E-04 |
| $\sigma(Y^E)$ | 4.78E-04 | 2.31E-03 | 2.09E-04 |

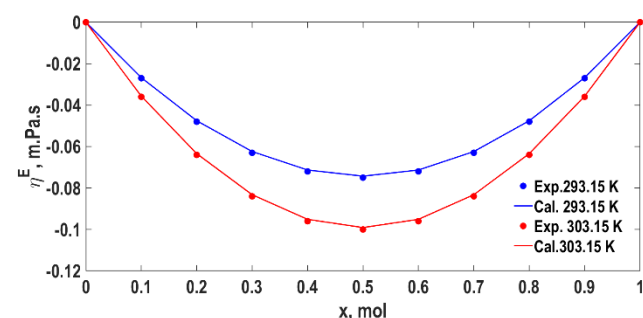


Figure 4. The experimental and calculated excess molar viscosities of the binary mixture of $xUTPO+(1-x)DF$ at 293.15 K and 303.15 K.

In Figure 4, it is seen that the excess viscosity values calculated from the Redlich–Kister equation are in agreement with the experimental values, and the deviation in the experimental excess viscosities is greater at 293.15 K. Experimental excess viscosities at 303.15 K were found to be lower than the values calculated from the Redlich–Kister equation. Deviations in excess viscosity values calculated from the polynomial equation are probably due to the increase in dispersive forces and dipole interactions at low temperatures and the increase in charge-transfer forces at high temperatures. As a result, a decrease in viscosity values was observed due to volumetric expansion as a result of the increase in intramolecular chemical bonds and the decrease

in dispersive forces and dipole bonds. As seen in Figure 4, as the temperature increase disperses localized π -electrons, π -bonds weaken and a more homogeneous mixture forms, and the flow of the liquid mixture accelerates. The negative values in the viscosity deviations of binary mixtures support weak interactions between *UTPO* and *DF* molecules. It is seen that the viscosity deviation becomes more clearly negative depending on the temperature increase. The reason for this is the acceleration of free flow due to the weakening of intermolecular interaction due to volumetric expansion.

The excess Gibbs energy of the binary mixture of *UTPO* + *DF* is given in Eq. (7) depending on viscosity

$$\frac{\Delta G^{*E}}{RT} = \ln\left(\frac{\eta v}{\eta_1 v_1}\right) - x_1 \ln\left(\frac{\eta_1 v_1}{\eta_2 v_2}\right) \quad (7)$$

where v is the molar volume of the mixture, v_1 and v_2 is the molar volume of the pure component, R is the gas constant, T is the absolute temperature, x_1 is mole fraction [19]. The dynamic viscosity of the mixture and pure components are η , η_1 and η_2 , respectively. The excess Gibbs energy values of binary mixture at 273.15 K and 303.15 K are given in Table 3. Figure 5 show the excess molar Gibbs energies calculated from experimental data and Redlich–Kister equation.

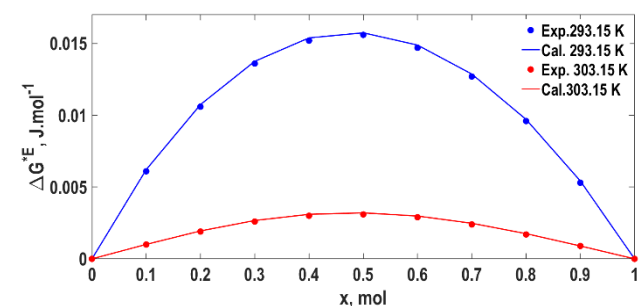


Figure 5. The experimental and calculated excess molar Gibbs energies of the mixture of $xUTPO+(1-x)DF$ at 293.15 K and 303.15 K.

A larger positive deviation was seen in the excess Gibbs energy at 273.15 K. At low temperature, higher activation energy is required for the flow of the mixture due to dispersive and dipole interactions between molecules. At 303.15 K, the activation energy required for the flow of the mixture decreased due to intramolecular charge-transfer in *UTPO*. A positive deviation in the ΔG^{*E} indicates that there is no exothermic interaction in the mixture. As seen in Figure 4, viscous flow is slower at low temperature. Since chemical interactions become more dominant as *UTPO* concentration increases, the positive deviation in ΔG^{*E} decreases at *UTPO* concentrations greater than 50%. ΔG^{*E} obtained from the Redlich and Kister equation and calculated from experimental data are more compatible with each other. A coefficients and standard deviation values in the Redlich and Kister equation are given in Table 4. Redlich–Kister equation coincided with the experimental results in great agreement.

4. Conclusion

The interactions between pyrolytic oil and diesel fuel occur depending on the concentration of both components, molecular structure and temperature. At low *UTPO* concentrations, dispersive forces and physical interactions dominate between *DF* and pyrolytic oil molecules. At high

UTPO concentrations, the disordered π -electrons in the aromatic structure in UTPO become localized and intramolecular π - π bonds between aromatic structures become more dominant than physical forces.

The increase in temperature caused a decrease in the viscosity of the binary mixture and reduced the activation energy required for flow. From these data, it was understood that there were no chemical interactions in mixtures of UTPO and DF in amounts less than 50%, and the volumetric expansion increased slightly with temperature.

Nomenclature

| | |
|------------------|---------------------------------------|
| A_i | Redlich–Kister equation Coefficients |
| M_i | Molar masses of components, |
| $\rho_{\bar{u}}$ | Densities of pure components |
| ρ | Density of the mixture, |
| $\sigma(V^E)$ | Standard deviation |
| η | Viscosity of binary mixture, |
| η_i | Viscosity of component, |
| $\Delta\eta$ | Viscosity deviation of binary mixture |
| ΔG^{*E} | Excess molar Gibbs energy |
| v | Molar volume of the solution |
| v_i | Molar volumes of pure components |
| V^E | Excess molar volume |
| exp. | Experimental |
| cal. | Calculated |
| x_i | Mole fractions of components |
| x | Mole fractions of mixture |
| TPO | Tire pyrolytic oil |
| UTPO | Upgraded tire pyrolytic oil |
| DF | Diesel fuel |
| v_{UTPO} | Pyrolytic oil volume in mixture |

References:

[1] G. C. d. Olivera Neto, L. E. C. Chaves, L. F. R. Pinto, J. C. C. Santana, M. P. C. Amorim, M. J. F. Rodrigues, "Economic, Environmental and Social Benefits of Adoption of Pyrolysis Process of Tires: A Feasible and Ecofriendly Mode to Reduce the Impacts of Scrap Tires in Brazil," *Sustainability*, vol. 11, no.7, p. 2076, 2019, [doi:10.3390/su11072076](https://doi.org/10.3390/su11072076).

[2] W. C. Wang, C. J. Bai, C. T. Lin, S. Prakash, "Alternative fuel produced from thermal pyrolysis of waste tires and its use in a DI diesel engine," *Appl. Therm. Eng.*, vol. 93, no. 1, pp. 330-338, 2016, [doi:10.1016/j.applthermaleng.2015.09.056](https://doi.org/10.1016/j.applthermaleng.2015.09.056).

[3] W. Li, C. Huang, D. Li, P. Huo, M. Wang, L. Han, G. Chen, H. Li, X. Li, Y. Wang, M. Wang, "Derived oil production by catalytic pyrolysis of scrap tires," *Chinese J. Catal.*, vol. 37, no. 4, pp. 526-532, 2016, [doi:10.1016/S1872-2067\(15\)60998-6](https://doi.org/10.1016/S1872-2067(15)60998-6).

[4] X. Zhang, H. Li, Q. Cao, J. Li, F. Wang, "Upgrading pyrolytic residue from waste tires to commercial carbon black," *Waste Management and Research*, Vol. 36, no. 5, pp. 436-444, 2018, [doi:10.1177/0734242X18764292](https://doi.org/10.1177/0734242X18764292).

[5] U. S. Vural, S. Uysal and A. Yinanc, "The improved diesel-like fuel from upgraded tire pyrolytic oil," *J. Serbian Chem. Soc.*, vol. 87, no. 10, pp. 1219-1235, 2022, [doi:10.2298/JSC211108048V](https://doi.org/10.2298/JSC211108048V).

[6] M. H. Hamzah, A. Alias, R. Mamat, A. A. Abdullah, A. Sudrajad, N. A. Ramlan, N. F. Jaharudin, "Diesel Engine Performance Operating with Tire Derived Fuel," *MATEC Web of Conferences*, vol. 225, pp. 04025, 2018, [doi:10.1051/mateconf/201822504025](https://doi.org/10.1051/mateconf/201822504025).

[7] A. Mohan, S. Dutta, S. Balusamy and V. Madav, "Liquid fuel from waste tires: novel refining, advanced characterization and utilization in engines with ethyl levulinate as an additive," *RSC Adv*, vol. 11, pp. 9807-9826, 2022, [doi:10.1039/d0ra08803j](https://doi.org/10.1039/d0ra08803j).

[8] M. Mia, A. Islam, R. I. Rubel, M. R. Islam, "Fractional Distillation & Characterization of Tire Derived Pyrolysis Oil," *Int. J. Eng. Technol.-IJET*, vol. 3, pp. 1-10, 2017, [doi:10.19072/ijet.280568](https://doi.org/10.19072/ijet.280568).

[9] U. S. Vural and S. Uysal, "Excess Molar Volumes, Apparent Molar Volumes, Partial Molar Volumes of Methionine, An Amino Acid, in Water+Ethanol and Water+Methanol Solutions at 298.15 K," *Int. J. Therm.*, vol. 25, no. 1, pp. 1-6, 2022, [doi:10.5541/ijot.1015207](https://doi.org/10.5541/ijot.1015207).

[10] A. Shalmashi and F. Amani, "Densities And Excess Molar Volumes For Binary Solution Of Water + Ethanol, + Methanol And + Propanol From (283.15 To 313.15) K," *Lat. Am. Appl. Res.*, vol. 44, pp. 163-166, 2014, [doi:10.52292/j.laar.2014.435](https://doi.org/10.52292/j.laar.2014.435).

[11] A. Ali, A. K. Nain, V. K. Sharma and S. Ahmad, "Molecular interactions in binary mixtures of tetrahydrofuran with alkanols (C6, C8, C10): an ultrasonic and volumetric study," *Indian J Pure Appl Phys*, vol. 42, pp. 666-673, 2004, [Online.] Available: <https://api.semanticscholar.org/CorpusID:55183104>.

[12] H. Iloukhani, M. Rezaei-Sameti and J. Basiri-Parsa, "Excess molar volumes and dynamic viscosities for binary mixtures of toluene ? n-alkanes (C5–C10) at T = 298.15 K, comparison with Prigogine-Flory-Patterson theory. *J Chem Thermodyn.*, vol. 38, pp. 975-982, 2006, [doi:10.1016/j.jct.2005.10.011](https://doi.org/10.1016/j.jct.2005.10.011).

[13] E. Yazdani, S. H. Hashemabadi and A. Taghizadeh, "Study of waste tire pyrolysis in a rotary kiln reactor in a wide range of pyrolysis temperature" *Waste Manage.*, vol. 85, pp. 195-201, 2019, [doi:10.1016/j.wasman.2018.12.020](https://doi.org/10.1016/j.wasman.2018.12.020).

[14] T. Menares, J. Herrera, R. Romero, P. Osorio and L. E. Arteaga-Pérez, "Waste tires pyrolysis kinetics and reaction mechanisms explained by TGA and Py-GC/MS under kinetically-controlled regime" *Waste Manage.*, vol. 102, pp. 21-29, 2020, [doi:10.1016/j.wasman.2019.10.027](https://doi.org/10.1016/j.wasman.2019.10.027).

[15] J. A. Dean, *Lange's Handbook of Chemistry*, 14th ed. New York, McGraw-Hill, 1992.

[16] B. P. Levitte, *Findlay's Practical Physical Chemistry*, 9th ed., Longman, New York, 1973.

[17] F. Campuzano, A. G. Abdul Jameel, W. Zhang, A.H. Emwas, A. F. Agudelo, J. D. Martínez and S. M. Sarathy, "Fuel and Chemical Properties of Waste Tire Pyrolysis Oil Derived from a Continuous Twin-Auger Reactor," *Energy and Fuels*, vol. 34, no. 10, pp. 12688-12702, 2020, [doi:10.1021/acs.energyfuels.0c02271](https://doi.org/10.1021/acs.energyfuels.0c02271).

- [18] B. Glavinčevski, L. Gardner, "An Expression for the Average Molecular Weight of Diesel Fuels," *SAE Technical Paper*, no. 861523, 1986, [doi:10.4271/861523](https://doi.org/10.4271/861523).
- [19] A. R. Mahajan and S. R. Mirgane, "Excess Molar Volumes and Viscosities for the Binary Mixtures of n-Octane, n-Decane, n-Dodecane, and n-Tetradecane with Octan-2-ol at 298.15 K", *J. Therm.*, vol. 2013, 2013, Art. No. 571918, [doi:10.1155/2013/571918](https://doi.org/10.1155/2013/571918).
- [20] F. Liang, M. Lu, T. C. Keener, Z. Liua and S. Khangb, "The organic composition of diesel particulate matter, diesel fuel and engine oil of a non-road diesel generator," *J. Environ. Monit.*, vol. 7, pp. 983-988, 2005, [doi:10.1039/B504728E](https://doi.org/10.1039/B504728E).
- [21] T.J Pilusa, M. Shukla, and E. Muzenda, "Pyrolitic Tyre Derived Fuel: A Review," in Proc. *International Conference on Chemical, Mining and Metallurgical Engineering (CMME'2013)*, Johannesburg (South Africa), Nov. 2013, pp. 27-28, [doi:10.13140/2.1.4533.1524](https://doi.org/10.13140/2.1.4533.1524).
- [22] A. Mohan, P. Kumar K P, V. Madav, "Investigation on Tire Pyrolysis Oil (Tpo) as a Fuel For Cook Stove And Lamps," in *IOP Conf. Series: Mater. Sci. Eng.*, March 2018, pp. Vol. 376, pp. 012036, [doi:10.1088/1757-899X/376/1/012036](https://doi.org/10.1088/1757-899X/376/1/012036).
- [23] Z. A. Tehrani and K. S. Kim, "Functional molecules and materials by π -Interaction based quantum theoretical design," *Int. J. Quant. Chem.*, vol. 116, pp. 622-633, 2016, [doi:10.1002/qua.25109](https://doi.org/10.1002/qua.25109).

Research Article

Exact Thermodynamic Solution of Gas Behavior in Propellant Tanks and Storage Capsules During Pressurization

*M. Mohseni 

Department of Mechanical Engineering, Qom University of Technology, Qom 37181 46645, Iran
E-mail: *m.mohseni@qut.ac.ir

Received 20 July 2024, Revised 15 September 2024, Accepted 15 November 2024

Abstract

The gas properties, particularly the pressure within the propellant tanks of a liquid-fueled rocket, play an essential role in the performance of the propulsion system. This study examines the thermodynamic behavior of the gas inside the propellant tanks and gas storage capsules of a class of pressurized systems. To this end, the governing thermodynamic equations were extracted, and exact thermodynamic solutions for the changes in the gas properties were obtained. The changes in the gas properties have been studied during the whole operation of the propulsion system, i.e. in the pre-pressurization period and before and after the gas cut-off time. A comparison of the analytical modelling results with the experimental data indicates a good agreement between the two, with the total mass of gas required for tank pressurization being approximately 4% higher than the experimental data. Additionally, the approximate changes in the throat area of the pressure-reducing valve were obtained. The simple thermodynamic model developed in this study allows for the rapid design and observation of the pressurization system's performance.

Keywords: Propulsion system; pressurization system; thermodynamic modeling; analytical solution, rapid design.

1. Introduction

The transient flow of two phases of gas and liquid in a tank is present in many cases, including the propellant tanks of a liquid fuel rocket [1], [2]. Liquid rockets require a pressurization system to pressurize the fuel and oxidizer in order to transfer them to the propellant pumps at the required flow and pressure [3]. The gas is placed in the upper space of the tanks, which is called ullage [2], [3]. The gas properties within the ullage, particularly the pressure, have been demonstrated to exert a substantial influence on the system's performance. This assertion has been the subject of extensive research, the findings of which are discussed in the following section.

In et al. [3] studied a liquid helium pressurization system that utilized an electrical heater to improve the performance of the system with thermodynamic and experimental methods. Majumdar et al. [4] developed a numerical model of self-pressurization of a cryogenic tank in ground operation using GFSSP code. In their model, the effect of liquid phase evaporation is considered in a relatively simple way. Zilliac [5] developed a thermodynamic model for changing the properties of gas in a pressurization system which models the self-pressurizing oxidizer system of a moderate-size hybrid rocket. In his model, the effect of mass and heat transfer between the two phases as well as heat transfer between the gas and the tank wall is considered. Karimi et al. [6] developed a thermodynamic model for a neutral gas storage type pressurization system in a liquid fuel rocket. Comparison with experimental data shows that the performance of their model is satisfactory. Using thermo-fluid relationships, Gieras, and Gorgeri [7] developed a mathematical model for the discharge of gas and liquid in the

propulsion tank and the combustion rate of fuel in a hybrid liquid-solid rocket engine. Their model was calibrated using experimental results and could be used for preliminary design. Wang et al. [8] investigated the pressurization process in a liquid hydrogen tank during discharge using the Fluent 6.3 CFD code. They examined the effect of phase change and the structure of the injector (direction of gas to enter the tank). According to their results, phase change has little influence on the behavior of the system so it can be ignored for convenience in numerical simulation. In another study, Wang et al. [9] investigated the effects of inlet temperature, injector structure, ramp time, wall thickness, and outflow rate on the performance of a pressurization system in a cryogenic tank. They showed that the effect of gas inlet temperature, and injector structure are high. Zuo et al. [10] numerically examined the flow of two liquid-vapor phases into a cryogenic tank of self-pressurization. They used Open Foam as a programming environment. According to their results, the speed of calculations of this program is several times faster than conventional software.

Given the numerous advantages of hydrogen (H₂), including high energy density, cleanliness, and carbon neutrality, Ali et al. [11] conducted an investigation into the potential opportunities for H₂ storage technologies, including physical and chemical storage, as well as the recent developments and challenges regarding hydrogen storage. The insulation of fuel storage tanks represents a significant topic of investigation, as evidenced by the work of Yin et al. [12]. A review of the recent progress in passive thermal protection technologies employed in the insulation structure of LH₂ storage tanks was conducted. One method of insulation or controllable release of energy is the application

of a coating to the storage tank, as demonstrated by Fan et al. [13]. The impact of fluidized bed coating temperature, air velocity, flow speed, and atomization pressure on the adhesion rate, coating integrity, and coating uniformity of the coated spherical propellant was examined in the study. Wang et al. [14] established a CFD model to investigate the wall insulation of a cryogenic tank during discharge on the pressurization system. Their results show that the inner insulation layer can significantly reduce the gas requirement which is more significant with the increase of inlet gas temperature. Li et al. [15] numerically examined the operating process in the spherical tank of a hydrogen liquid rocket. They performed their solution in two dimensions using the ANSYS Fluent 17 commercial software. This software is utilized extensively for the analysis of fluid mechanics issues, encompassing a multitude of physical phenomena, including multiphase and turbulent flows. In the study of Li et al. [15], the VOF model is used to solve the two-phase flow and the RNG $k-\epsilon$ to model the turbulent flow. According to their results, fluid phase change leads to an increase in the amplitude of temperature fluctuations. In another study, Li and Liang [16] simulated the mass and heat transfer between the two phases of gas and liquid inside the hydrogen tank during the pressurization process. They investigated the effect of temperature and mass flow rate of the inlet gas as well as its direction of spraying on the problem. In the work of Wang et al. [17], in addition to heat transfer inside the tank, the effect of aerodynamic heating is also considered. Based on their results, in ordinary conditions outside aerodynamic heating cannot penetrate the foam layer to facilitate the pressurization performance. In other words, if the thermal performance of the outer surface of the tank wall does not have a specific case, the effect of aerodynamic heating in the CFD simulation of a foam-insulated tank can be ignored. Mitikov and Shynkarenko [18] suggested a method to reduce the final mass of the pressurization system by two commands from the control system to open the drain valve and close it. In this regard, energy management equipment can be employed to enhance system performance and reduce its weight, as demonstrated by Yilmaz et al. [19]. Barsi, and Kassemi [20] developed a two-phase lumped vapor CFD model which was used to describe the self-pressurization behavior of a tank partially filled with LH_2 in normal gravity. Their model is somewhat consistent with the experimental data. Numerical results of Panzarella, and Kassemi [21] which investigated the pressurization of a large cryogenic storage tank indicate that in microgravity both buoyancy and natural convection are still important and play a significant role in phase distribution and tank pressurization. Fester and Bingham [22] studied numerous propellant combinations to form a small combustion zone. The resulting hot combustion gases were used to pressurize the tank to operating pressure and then maintain this pressure during outflow. One method for enhancing the efficiency of combustion energy release is to optimize the detonation process, which is the focus of Yang's [23] research. In light of these findings, it may be posited that high-performance heritage solid fuels for pyrotechnics, such as boron, titanium hydride, and carbon, could be employed as injectants for the enhancement of detonation performance, thereby mitigating the effects of transients in high-pressure, high-rate gaseous injection, as exemplified by scramjets. In a recent publication, Scholl et al. [24] presented a novel concept of microencapsulated hydrocarbon fuels for the development of a monopropellant system. This system is

employed in rocket engines when the requisite reliability and technical simplicity are paramount.

While the research conducted thus far has yielded valuable insights, it is imperative to continue investigating this field to gain a more comprehensive understanding. Previous studies have typically employed the use of commercial software for the detailed examination of flow patterns. Other researchers have developed a thermodynamic model that necessitates a numerical solution. Moreover, the majority of existing research has focused on self-pressurization systems, with comparatively limited investigation of pressurization systems for gas storage. Accordingly, the present study employs a straightforward analytical thermodynamic model to examine the functionality of a pump-fed gas storage pressurization system in a liquid fuel rocket. To this end, the behavior of the gas within the propellant tanks and the gas storage capsules has been examined, and the quantity of gas necessary for each tank has been determined.

2. Problem Description

Figure 1 depicts a schematic representation of the pump-fed gas storage type pressurization system in a liquid rocket.

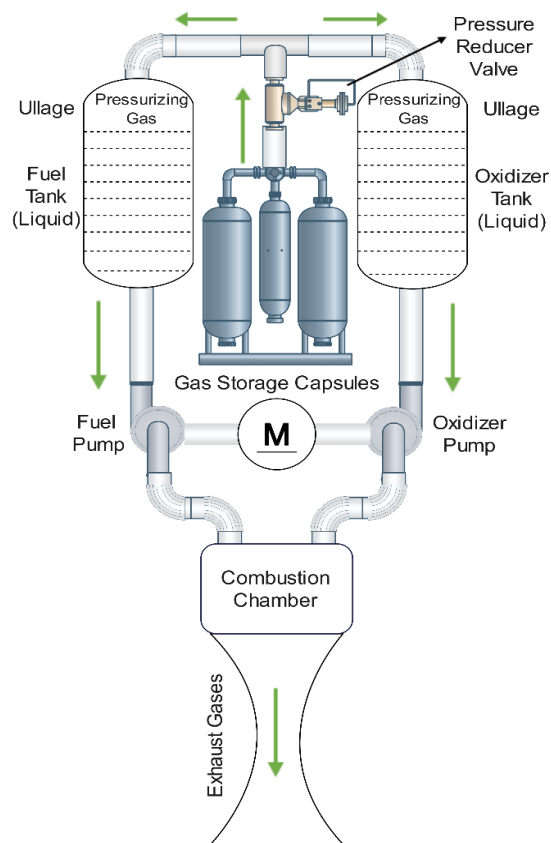


Figure 1. Schematic of the gas-storage pressurization system.

The operation of this system is as follows: the pressurizing gas, after flowing from its storage capsules in which it is kept under high pressure, passes through a pressure-reducing valve and then enters the fuel and oxidizer tanks, where it exerts pressure on them. This pressure is essential for the prevention of cavitation in engine pumps during operation. It is crucial to acknowledge that the storage of gas at high pressure in capsules serves the purpose of reducing the overall volume and mass of the system. The gas is utilized in a gradual manner throughout the course of the flight.

In liquid fuel rockets, the gas typically flows around the engine in order to gain heat before entering the tanks, thereby elevating its temperature and, consequently, its pressure. This process results in a reduction in the quantity of gas required for pressurization and cooling of the engine wall, although it introduces additional complexity into the system.

As illustrated in Figure 1, the upper portion of the tank depicts the volume of the pressurizing gas. As previously stated, the term "ullage" is used to describe the space above the liquid fuel or oxidizer within the tanks into which the gas is introduced. The selection of the pressurizing gas is also a significant factor, with implications for the overall mass of the rocket. This indicates that gases with a lower molar mass than air, such as helium, can be an effective means of reducing the mass of the system, provided that the system is adequately sealed. For a more thorough examination of the system's functionality, readers are directed to consult reference [25].

3. Thermodynamic Modeling

The first law of thermodynamics for a control volume in the transient state is as follows [26].

$$\dot{Q} - \dot{W} + \sum \dot{m}_i \theta_i - \sum \dot{m}_e \theta_e = \frac{dE}{dt} \quad (1)$$

where

$$\theta = h + \frac{v^2}{2} + gz \quad (2)$$

is the energy of a flowing fluid and

$$\Delta E = \Delta U + \Delta Ke + \Delta Pe \quad (3)$$

is the change of system energy. In Eq. (1), \dot{Q} and \dot{W} are the rate of heat transfer and rate of work, respectively. Additionally, h , V , z , U , Ke , and Pe represent enthalpy, velocity, elevation, internal energy, kinetic energy and potential energy.

By ignoring the changes in kinetic and potential energies of the system as well as the heat transfer term Eq. (1) can be simplified as follows.

$$-\dot{W} + \sum \dot{m}_i h_i - \sum \dot{m}_e h_e = \frac{dU}{dt} \quad (4)$$

It should be noted that although changes in kinetic and potential energies alone can be significant, they are negligible in comparison to changes in enthalpy. Additionally, while heat transfer does influence the outcomes to a degree, its intricate mechanism which encompasses both natural and forced convection, as well as the aerodynamic heating of the flying device's outer wall makes it challenging to model with precision.

As mentioned before, two important elements of the pressurization system are the gas storage capsules and the propellant tanks which their equations discuss separately in the two following sections.

3.1 Propellant Tanks

Considering the ullage as the control volume and with one input to the ullage, Eq. (4) becomes as follows.

$$\frac{dU}{dt} = \dot{m}_i h_i - p \dot{V} \quad (5)$$

In the above equation, p is gas pressure inside the tank, \dot{m}_i is the mass flow rate of the gas entering the tank, and \dot{V} is the gas volume expansion rate. Considering the temperature and pressure range in the tank, the ideal gas equation of state can be used. Under these conditions, the internal energy of the gas is obtained from the following relation.

$$U = m C_v T = \frac{pV}{k-1} \quad (6)$$

By differentiating the above relation with respect to time and combining the result with Eq. (5), the following equation is obtained for changes in gas pressure inside the tank.

$$\frac{dp}{dt} = \frac{k-1}{V(t)} \dot{m}_i h_i - \frac{kp}{V(t)} \frac{dV}{dt} \quad (7)$$

In deriving Eq. (7), the following assumptions have been made.

- 1- $k = C_p/C_v$ has a constant value in which C_p and C_v are gas specific heats.
- 2- The different properties of the gas inside the ullage are homogeneous and uniform. In other words, they change only with time.
- 3- The mass transfer between liquid and gas phases due to evaporation and condensation is neglected. It should be noted that in the pressurization system of the neutral gas storage type, unlike the self-pressurization type, this assumption is reasonable.
- 4- Heat transfer between gas and its environment has been neglected.

In addition to the numerical solution, for the conditions of the present study, Eq. (7) has an analytical solution. To do this, Eq. (7) can be written as Eq. (8).

$$\frac{dp}{dt} + f(t)P = g(t) \quad (8)$$

where,

$$f(t) = k \frac{\dot{V}}{V(t)} \quad (9)$$

and

$$g(t) = \frac{k-1}{V(t)} \dot{m}_i h_i \quad (10)$$

For an ideal gas, Eq. (10) may be written as Eq. (11).

$$g(t) = \frac{k-1}{V(t)} \dot{m}_i c_p T_i \quad (11)$$

Equation (8) is a first-order linear ordinary differential equation with the following answer [27].

$$p(t) = \frac{1}{\lambda} \int g(t) \lambda dt + \frac{p_0}{\lambda} \quad (12)$$

where,

$$\lambda = e^{\int f(t) dt} \quad (13)$$

During the entire engine operation time, the mass flow rate of the liquid from the tanks is constant. As a result, the volume of the gas in the tank will be a linear function of time, which is obtained from the following equation.

$$V(t) = V_0 + \dot{V}t \quad (14)$$

In Eq. (14) V_0 is initial volume of the gas. Also in this study, based on experimental results [6] and for modeling convenience, the mass flow rate of the inlet gas is considered a constant or a linear function of time depending on the period of the pressurization process. For these conditions, it can be written as:

$$\dot{m}_i = a + bt \quad (15)$$

where a and b are constant.

Using the equations above, we can find the answer to Eq. (8). This answer shows the changes in gas pressure inside the tank during engine operation.

$$p(t) = \frac{RT_i}{V(t)^k} \left\{ \dot{m}_i(t)V(t)^k - \dot{m}_{i0}V_0^k - \frac{b}{(k+1)V} [V(t)^{k+1} - V_0^{k+1}] \right\} + p_0 \left[\frac{V_0}{V(t)} \right]^k \quad (16)$$

In the above equation, R is the gas constant, and p_0 is the initial pressure of the gas. In general, the answer to Eq. (8) is obtained by numerical calculation methods such as Euler or Range-Kutta [28].

The density of the gas inside the tank is also obtained from the following equation.

$$\rho(t) = \frac{m(t)}{V(t)} = \frac{1}{V(t)} (m_0 + \int \dot{m}_i dt) \quad (17)$$

where m_0 is the initial mass of the gas inside the tank. To obtain the temperature at any instant in time, the ideal gas equation of state can be used as follows.

$$T(t) = \frac{p(t)}{\rho(t)R} \quad (18)$$

3.2 Gas Storage Capsules

For gas-storage capsules with no work, Eq. (4) becomes as follows.

$$-\dot{m}_e \left(h_e + \frac{V_e^2}{2} \right) = \frac{dU}{dt} \quad (19)$$

Using the ideal gas equation and the definition of internal energy, i.e. Eq. (4), Eq. (19) can be written as

$$-\dot{m}_e \left(C_p T_e + \frac{V_e^2}{2} \right) = C_v m \frac{dT}{dt} + C_v T \frac{dm}{dt} \quad (20)$$

Due to the large difference between the gas pressure inside the capsules and the outlet pressure of the reducer valve, flow chokes at the outlet of the valve, and the Mach number becomes equal to 1 [29]. This means that the speed of the gas is equal to the speed of sound. As a result, we will have:

$$-\dot{m}_e \left(\frac{kR}{k-1} T_e + \frac{kRT_e}{2} \right) = C_v m \frac{dT}{dt} - C_v T \dot{m}_e \quad (21)$$

By simplifying the above equation and the relationship between the outlet static temperature and the stagnation temperature inside the capsule, we can write [29]:

$$(1-k)\dot{m}_e T = m \frac{dT}{dt} \quad (22)$$

In the case of choked flow, the mass flow rate of the gas is obtained from the following relation [29].

$$\dot{m} = f A^* \frac{p}{\sqrt{T}} \quad (23)$$

where,

$$f = \sqrt{\frac{k}{R} \left(\frac{2}{k+1} \right)^{\frac{k+1}{k-1}}} \quad (24)$$

Here A^* is the area of the critical throat where the Mach number is equal to 1. Thus, Eq. (22) can be written as

$$(1-k)fA^* \frac{\rho RT}{\sqrt{T}} T = \rho V \frac{dT}{dt} \quad (25)$$

or

$$-\frac{(k-1)}{V} f A^* R T^{3/2} = \frac{dT}{dt} \quad (26)$$

By solving the above equation and a little algebraic operation, the temperature changes of the gas inside the capsule will be as follows.

$$T = \frac{T_0}{\left\{ \left[\frac{(k-1)}{2V} f A^* R \sqrt{T_0} \right] t + 1 \right\}^2} \quad (27)$$

where T_0 is the initial temperature of the gas and V is the capsule volume. The Eq. (27) can be written as a simple form as Eq. (28).

$$\frac{T}{T_0} = (1+Bt)^{-2} \quad (28)$$

where,

$$B = \left[\frac{(k-1)}{2V} f A^* R \sqrt{T_0} \right] \quad (29)$$

The changes in gas density are equal to

$$\frac{d\rho}{dt} = -\frac{\dot{m}}{V} \quad (30)$$

Using the mass flow rate formula and the ideal gas equation, we will have

$$\frac{d\rho}{\rho} = -\frac{f A^* R}{V} \frac{T}{\sqrt{T}} dt \quad (31)$$

which can be written as Eq. (32) by applying the temperature equation.

$$\frac{d\rho}{\rho} = -\frac{f A^* R \sqrt{T_0}}{V} \frac{dt}{(1+Bt)} \quad (32)$$

By solving the above equation, the gas density changes inside the capsule are obtained as follows.

$$\frac{\rho}{\rho_0} = (1+Bt)^{-\frac{2}{k-1}} \quad (33)$$

where B is defined in Eq. (29). By applying the ideal gas equation, the gas pressure variations are obtained as Eq. (34).

$$\frac{p}{p_0} = (1 + Bt)^{-\frac{2k}{k-1}} \quad (34)$$

By knowing the amount of mass of the gas required for pressurization, the number of gas storage capsules can be obtained. In this instance, the following relationship exists between the pressure, temperature, volume, mass, and number of gas storage capsules (N), whereby Z represents the gas compressibility factor.

$$p(NV) = mZRT \quad (35)$$

It is important to note that V represents the volume of each individual capsule. Therefore, NV represents the total volume of all capsules. For calculating the compressibility factor, the famous Lee-Kesler equation of state can be used [30].

$$Z = \frac{P_r v_r}{T_r} = 1 + \frac{B}{v_r} + \frac{C}{v_r^2} + \frac{D}{v_r^3} + \frac{c_4}{T_r^3 v_r^2} \left(\beta + \frac{\gamma}{v_r^2} \right) \exp\left(-\frac{\gamma}{v_r^2}\right) \quad (36)$$

in which

$$B = b_1 - \frac{b_2}{T_r} - \frac{b_3}{T_r^2} - \frac{b_4}{T_r^3} \quad (37)$$

$$C = c_1 - \frac{c_2}{T_r} + \frac{c_3}{T_r^3} \quad (38)$$

$$D = d_1 + \frac{d_2}{T_r} \quad (39)$$

and

$$T_r = \frac{T}{T_{cr}}, P_r = \frac{p}{P_{cr}}, v_r = \frac{v P_{cr}}{RT_{cr}} \quad (40)$$

where $T_{cr} = 132.5 \text{ K}$, $P_{cr} = 37.7 \text{ bar}$, and $\rho_{cr} = 11.325 \text{ kg/m}^3$ are the critical temperature, critical pressure, and critical density of the gas, respectively. Also, the constants utilized in the aforementioned equation can be found in Ref. [30].

4. Results and Discussion

In this section, the performance of the obtained thermodynamic model is evaluated by comparing its results with experimental data [6]. The conditions utilized for the calculation of the results, as well as the properties of the liquids and the gas, are presented in Tables 1 and 2.

Table 1. Liquid properties and solution conditions.

| Quantity | Upper tank | Lower tank |
|--------------------------|-----------------------|------------------------|
| Density | 804 kg/m ³ | 1596 kg/m ³ |
| Mass flow rate | 25 kg/s | 92 kg/s |
| Initial temperature | 300 K | 300 K |
| Initial pressure | 1.4 bar | 0.86 bar |
| Required ullage pressure | 6 bar | 6.2 bar |

Table 2. Gas properties and solution conditions.

| Quantity | Upper tank | Lower tank |
|------------------------|---------------------|--------------------|
| Density | Ideal gas | Ideal gas |
| Specific heat capacity | 1005 J/kg.K | 1005 J/kg.K |
| Initial volume | 0.19 m ³ | 0.3 m ³ |
| Inlet temperature | 425 K | 425 K |
| Initial temperature | 300 K | 300 K |
| Relative cut-off time | 0.29 | ---- |

In accordance with the aforementioned conditions, the variations in gas pressure within the ullage of the lower and upper tanks are illustrated in Figures 2 and 3. The relative time represented in these figures is obtained by dividing the instantaneous time by the total time of engine operation.

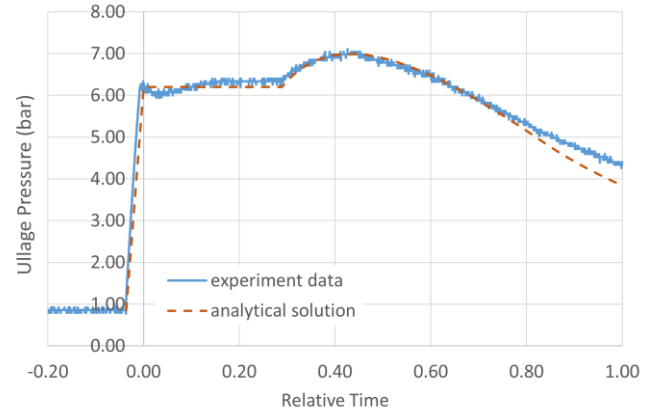


Figure 2. Comparison of changes in gas pressure inside the lower tank obtained from the thermodynamic model with experimental data [6].

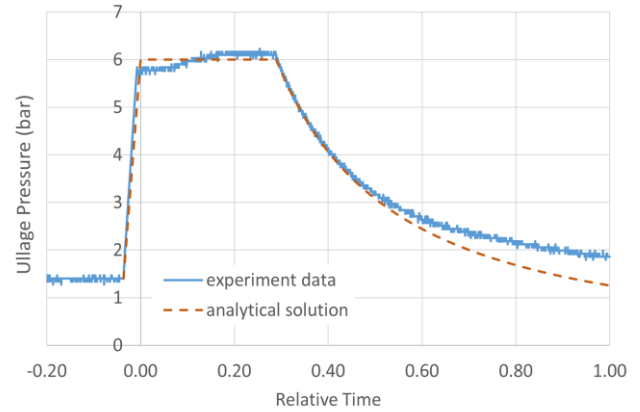


Figure 3. Comparison of changes in gas pressure inside the upper tank obtained from the thermodynamic model with experimental data [6].

According to these figures, the total operating time of the pressurization system is divided into three parts. The first section of the figures is the pre-pressurization period until the tank pressure reaches the nominal value of about 6 bar and then the engine starts. The second stage is from the time the engine is started until the gas is cut to the upper tank. And the third part is from the time of cutting the gas to the end of the engine operation. It should be noted that the reason for cutting off the inlet gas to the upper tank is to provide the required ullage pressure by the amount of gas entering the tank up to this point and the effect of acceleration of the rocket. As a result, to reduce the mass of the gas, its inlet to the upper tank is cut off after a while. In these situations, the efficacy of sensors and the reliability of a robust model for their estimation can have a significant impact on the management of rocket engine health [31].

It is observed from Figures 2 and 3 that after shutting off the inlet gas to the upper tank its pressure decreases while for the lower tank, on the contrary, its pressure increases. This is because after cutting off the gas in the upper tank, the total mass flow of the gas enters the lower tank. Also, as can be seen, except for the final moments of the engine operation,

where the difference between the modeling results and the experimental data for the upper tank is significant, in other cases, there is a good agreement between the two. The reason for this difference is the heat transfer from the tank walls, which is affected by aerodynamic heating, to the internal gas, which has been neglected in thermodynamic modeling. More explanation is that a reduction in gas pressure within the upper tank at the end time of the system's operation, as illustrated in Fig. 3, results in a decline in gas temperature, reaching a point below that of the tank wall temperature. This phenomenon initiates a heat transfer from the wall, which has been subjected to aerodynamic heating and is consequently at a higher temperature, to the gas, leading to an increase in its temperature and pressure. According to Figure 3, this difference increases as the engine runs out of time when the pressure and consequently the upper tank temperature are significantly reduced. Given that the modeling results predict the pressure to be less than the actual value, this can be considered a reliability factor for designing the pump inlet pressure.

To see the gas temperature changes, diagrams for both the upper and lower tanks are plotted in Figure 4. As can be seen, the gas temperature of the upper tank drops to about 260 K (-13 °C) due to the cut-off of the inlet gas.

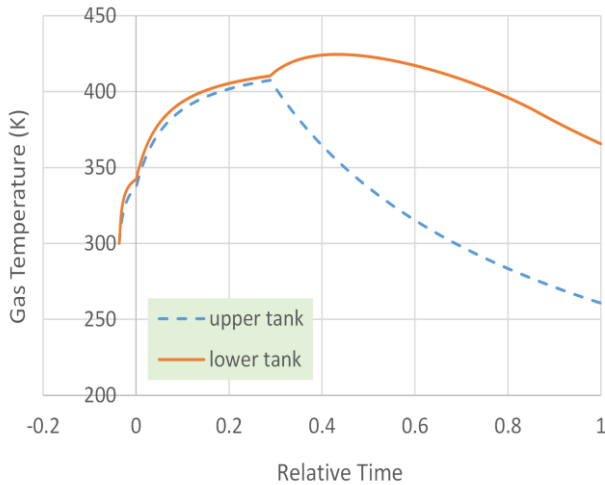


Figure 4. Changes in gas temperature inside the propellant tanks using the present model.

Using Eq. (7), the required mass flow rate of the gas in the pre-pressurization process can be calculated from the following equation.

$$\dot{m}_{i1} = \frac{(p-p_0)V_0}{kRT_i t_1} \quad (41)$$

where t_1 is the pre-pressurization time and p is the pressure required at the end of the pre-pressurization time to start the engine. Also, the mass flow rate of the gas in the second stage, when the gas pressure remains almost constant, is obtained approximately from the following equation.

$$\dot{m}_{i2} = \frac{P}{RT_i} \cdot \frac{\dot{m}_l}{\rho_l} \quad (42)$$

where \dot{m}_l and ρ_l are the output mass flow rate of the liquid propellant and its density, respectively. In a real problem, the liquid fuel discharge from the tank is obtained based on the needs of the engine. Also, the inlet gas flow rate to the tank is determined based on the need for inlet pressure to the

pumps. This pressure can be calculated from the following equation [6].

$$P_p = P_u + \rho H a - 0.58\rho V_p^2 - \rho h_L \quad (43)$$

where,

$$a = g \sin\theta + \ddot{x} \quad (44)$$

is the acceleration of the flying device and

$$H = H_0 - \frac{\dot{m}_l}{\rho_l A_t} t \quad (45)$$

is the height of the fluid from the level of the liquid propellant in the tanks to the pump inlet. In addition, V_p is the liquid velocity at the pump inlet and ρh_L is the pressure loss in the pipeline before the pump. It should be noted that the mass flow rate obtained from the Eq. (42) is the required mass flow rate or is an average value while it decreases almost linearly in the pre-pressurization period as follows.

$$\dot{m}_i = a + bt \quad (46)$$

Since the pre-pressurization time is before the zero time, so at the time $t=0$, $\dot{m}_i = \dot{m}_{i2}$. Thus, the constant 'a' will equal to \dot{m}_{i2} . To obtain the constant 'b' in Eq. (46), the Eq. (7) can be written as

$$\frac{dp}{dt} = \frac{k-1}{v_0} \dot{m}_i C_p T_i \quad (47)$$

By integrating the above equation and using Eqs. (42), (43), and (44), the value of 'b' is obtained as

$$b = 2 \frac{(\dot{m}_{i1} - \dot{m}_{i2})}{t_1} \quad (48)$$

And thus, the relation for pre-pressurization mass flow rate can be written as the following equation.

$$\dot{m}_i = \dot{m}_{i2} + 2 \frac{\dot{m}_{i1} - \dot{m}_{i2}}{t_1} t \quad (49)$$

According to previous discussions, changes in the mass flow rate of the inlet gas to the upper and lower tanks are shown in Figures 5 and 6 and compared with the experimental data. Such changes in mass flow rate occur in the type of liquid fuel rocket whose pressurization system uses gas storage capsules.

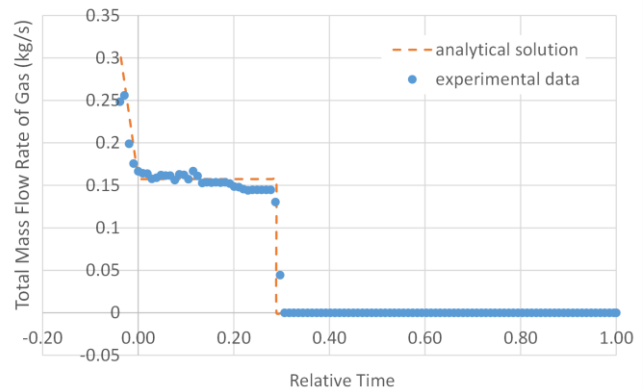


Figure 5. Changes in the mass flow rate of the inlet gas to the upper tank [6].

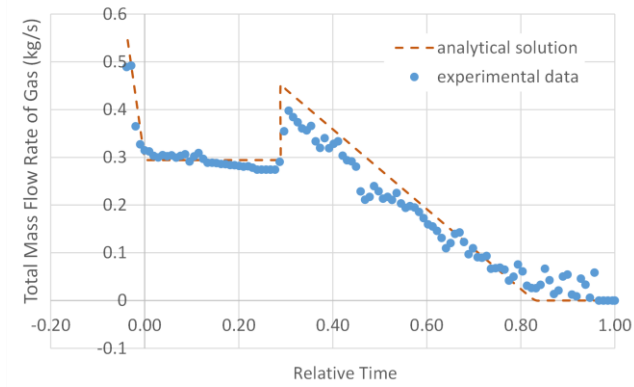


Figure 6. Changes in the mass flow rate of the inlet gas to the lower tank [6].

As mentioned earlier, the pre-zero time section is for the pre-pressurization period until the tank pressure reaches the nominal value and then the engine starts. The mass flow is then reduced to an almost constant value so that the tank pressure is maintained at its nominal value. It is observed that after cutting off the gas of the upper tank, the total mass flow rate enters the lower tank, and its flow rate increases at once.

Figure 7 shows the changes in the total mass flow rate to the tanks based on modeling results and experimental data. The values of this figure are equal to the sum of the values of the two Figures 5 and 6, which come out of the gas storage capsules and pass through the pressure-reducing valve.

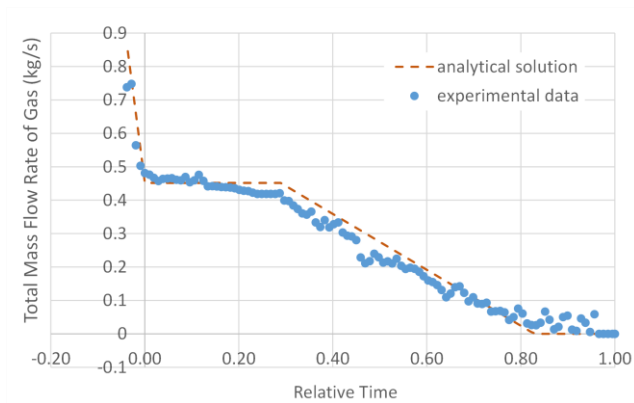


Figure 7. Changes in the total mass flow rate of the gas entering the tanks [6].

By integrating the above diagrams with respect to time, the mass of the consumed gas as a function of time is obtained which is shown in Figure 8. As can be seen, the difference in the final mass of the gas for the two diagrams is about 4%. By knowing the amount of mass of the gas required for pressurization, the number of gas storage capsules can be obtained.

Depending on the amount of mass consumed and the volume of the ullage at any given time, changes in gas density can be obtained during engine operation. The results so obtained for the gas density variations are plotted in Figures 9 and 10 for both lower and upper tanks. In this case, the maximum difference that occurs for the lower tank is less than 8%. Generally speaking, there is a good agreement between the results of thermodynamic modeling and the experimental data. Table 3 shows the maximum difference for the various quantities including mass, pressure, and

density of the gas for both upper and lower tanks during the whole time of engine operation.

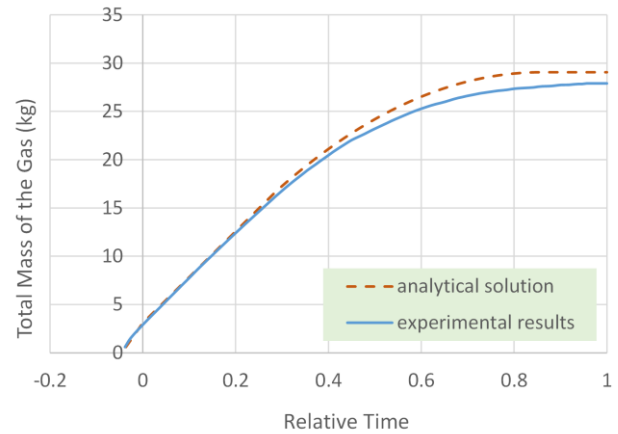


Figure 8. Changes in the total mass of the incoming gas to the tanks.

In the following, based on the relationships derived in Sec. 3.2, the time variations of the pressure and temperature of the gas inside the gas storage capsules are plotted in Figures 11 and 12 and compared with the experimental data [6]. As can be seen, there is a good agreement between these graphs except in the last moments. This difference can be caused by the effect of heat transfer that occurs when the temperature of the gas inside the capsules drops.

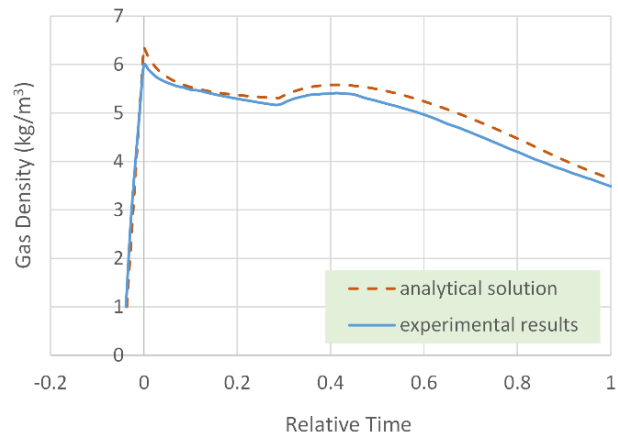


Figure 9. Changes in gas density inside the lower tank using the present model and experimental data.

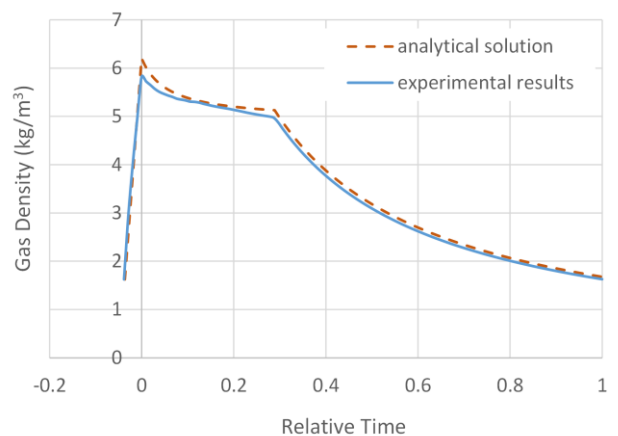


Figure 10. Changes in gas density inside the upper tank using the present model and experimental data.

Table 3. The maximum difference between thermodynamic modeling results and experimental data [6].

| Quantity | Tank | Model | Exp. [6] | Error (%) |
|----------|-------|------------------------|------------------------|-----------|
| Mass | Lower | 23.26 kg | 22.14 kg | 5.09 |
| | Upper | 5.93 kg | 5.76 kg | 2.98 |
| | Total | 29.06 kg | 27.89 kg | 4.17 |
| Pressure | Lower | 3.82 bar | 4.4 bar | 13.18 |
| | Upper | 1.25 bar | 1.86 bar | 32.53 |
| Density | Lower | 6.2 kg/m ³ | 5.82 kg/m ³ | 6.53 |
| | Upper | 5.32 kg/m ³ | 4.95 kg/m ³ | 7.47 |

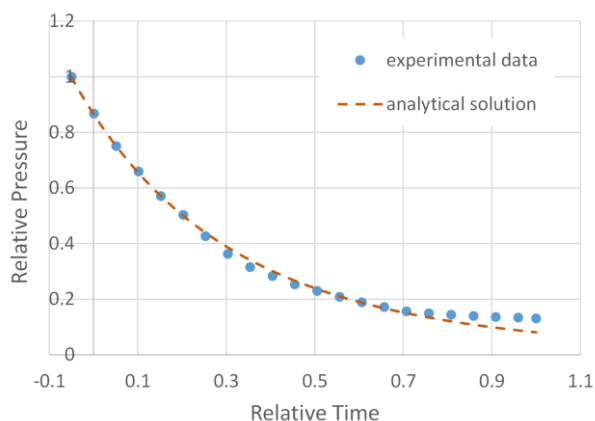


Figure 11. Pressure variations inside the gas-storage capsules using the present model and experimental data [6].

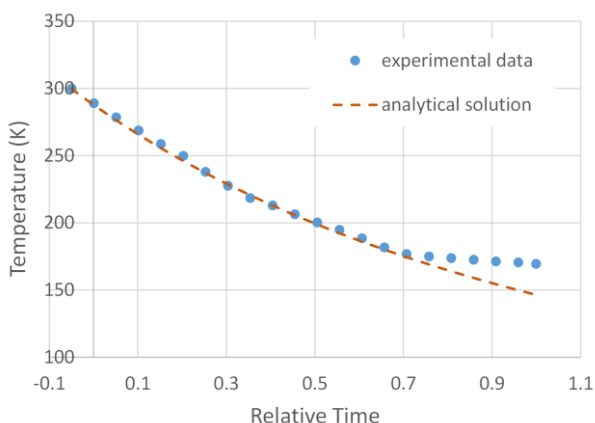


Figure 12. Temperature variations inside the gas storage capsules using the present model and experimental data [6].

Based on the obtained results, the final mass of the gas inside the capsules is about 7.5 kg, which shows the total initial mass of the gas with the amount of mass used for the propellant tanks. Figure 13 shows the time variations of the gas mass inside the capsules for both ideal gas behavior and when the gas compressibility factor, Z , is considered. It should be noted that due to the gas pressure loss when passing through the reducing valve and the path until it reaches the tanks, some gas remains inside the capsules. In cases where there is a pressure-reducing valve after the capsules, this valve while reducing the high pressure of the capsules, is responsible for controlling the ullage pressure of the propellant tanks at the nominal value. In the beginning, when the pre-pressurization of the tanks starts and the pressure of the tanks increases, the cross-sectional area of the valve throat decreases until it reaches its minimum value. When the engine starts at time $t=0$, due to the increase in the volume of the ullage on one side and the decrease in the pressure of the gas storage capsules on the other side, the

valve increases its cross-sectional area to reach its initial maximum value to prevent the decrease in the pressure of the tanks. From here on, the cross-section of the valve remains constant and the pressure of the propellant tanks gradually decreases due to the decrease in the inlet mass flow rate. Figure 14 shows the changes in the cross-section of the valve's throat.

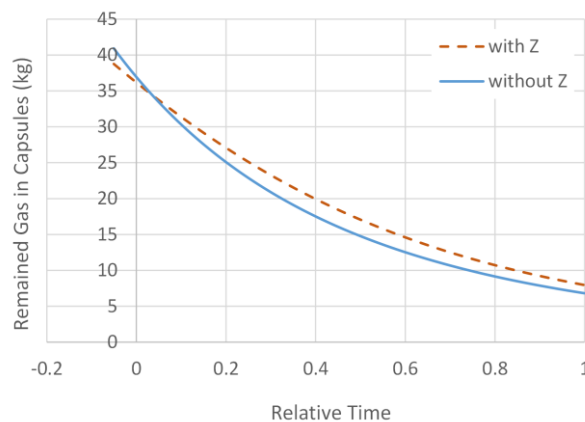


Figure 13. Time variations of gas mass inside the gas storage capsules with and without compressibility factor effect, Z .

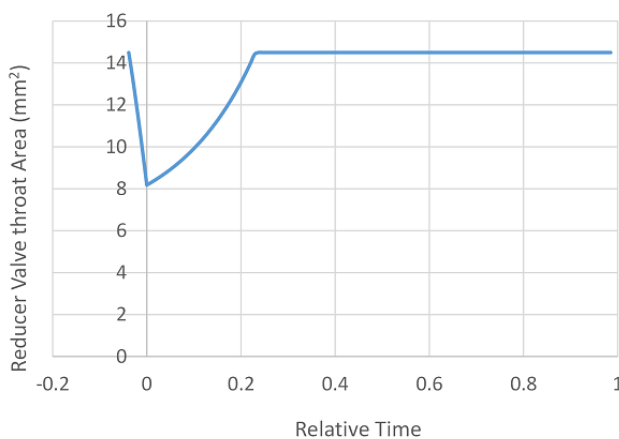


Figure 14. Variations of the cross-sectional area of the valve throat.

5. Conclusions

The objective of this study is to examine the alterations in the properties of the gas within the pressurization system of a liquid fuel rocket by developing an analytical thermodynamic model. The process encompasses the entirety of the engine's operational duration. To validate the performance of the thermodynamic model, the results are compared with the experimental data for the gas properties inside the ullage as well as the gas storage capsules. The following are the most notable outcomes of this study.

- A comparison of the results reveals that the discrepancy in outcomes is most pronounced for the upper tank gas pressure in the last moments, due to ignoring the impact of heat transfer from the wall. This discrepancy reaches approximately 32%. At other times, however, the modeling results predict well the experimental data. In addition, the modeling results show that the mass of the gas used to pressurize the tanks is only about 4% higher than the experimental value.
- For the gas storage capsule, there is also a good agreement between the modeling results and the experimental data except at the end moments due to the

ignoring heat transfer such as propellant tanks. Using the obtained results, it is possible to specify the initial mass of the gas as well as the remained gas in the capsules. In addition, one can observe the approximate changes in the critical cross-sectional area of the pressure-reducing valve, which also acts as an ullage pressure controller.

- As a consequence, the derived model can be employed with an acceptable degree of precision to examine temporal alterations in gas characteristics throughout the course of engine operation. The determination of the system's behavior requires only a few minutes, given the relationships obtained.

Nomenclature

| | |
|------------|--|
| a | acceleration (m/s^2) |
| C_p | specific heat at constant pressure (J/kg.K) |
| C_v | specific heat at constant volume (J/kg.K) |
| g | gravity acceleration (m/s^2) |
| h | specific enthalpy (J/kg) |
| H | fluid height (m) |
| k | gas-specific heat ratio |
| Ke | kinetic energy (J) |
| m | mass (kg) |
| \dot{m} | mass flow rate (kg/s) |
| N | number of capsules |
| p | pressure (Pa) |
| Pe | potential energy (J) |
| \dot{Q} | rate of heat transfer (W) |
| R | gas constant (J/kg.K) |
| t | time (s) |
| T | temperature (K) |
| U | internal energy (J/kg) |
| V | volume (m^3) |
| \dot{V} | volume expansion rate (m^3/s) |
| \dot{W} | work per time or power (W) |
| \ddot{x} | acceleration (m/s^2) |
| z | height (m) |
| Z | gas compressibility factor |

Greek Symbols

| | |
|-------------|-----------------------------|
| ρ | density (kg/m^3) |
| ϑ | pith angle (rad) |

Subscripts

| | |
|---|--------------------|
| e | exit |
| i | inlet |
| g | gas |
| l | liquid |
| 0 | initial conditions |
| p | pump |
| u | ullage |

References:

- [1] M. Mohseni and M. K. Domfeh, "Numerical analysis of transient vortex formation at the outlet of a tank containing gas-liquid phases," *J. Appl. Fluid Mech.*, vol. 16, no. 11, pp. 2235–2248, 2023, doi: 10.47176/jafm.16.11.1942.
- [2] P. Adnani and R. W. Jennings, "Pressurization analysis of cryogenic propulsion systems," in *Proc. 36th AIAA/ASME/SAE/ASEE Joint Propulsion Conf. Exhibit*, 2000, doi: 10.2514/6.2000-3788.
- [3] S. In, S. Jeong, and H. Kim, "Investigation on liquid helium pressurization process using a heater in a liquid propellant rocket," *Cryogenics*, vol. 44, no. 6, pp. 467–474, 2004, doi: 10.1016/j.cryogenics.2004.02.010.
- [4] A. Majumdar, J. Valenzuela, A. Leclair, and J. Moder, "Numerical modeling of self-pressurization and pressure control by a thermodynamic vent system in a cryogenic tank," *Cryogenics*, vol. 74, pp. 113-122, 2016, doi: 10.1016/j.cryogenics.2015.12.001.
- [5] G. Zilliac and M. Arif Karabeyoglu, "Modeling of propellant tank pressurization," in *Proc 41st AIAA/ASME/SAE/ASEE Joint Propulsion Conf. and Exhibit*, 2005, doi: 10.2514/6.2005-3549.
- [6] H. Karimi, A. Nassirharand, and M. Mohseni, "Modeling and simulation of a class of liquid propellant engine pressurization systems," *Acta Astronaut.*, vol. 66, no. 3–4, pp. 539-549, 2010, doi: 10.1016/j.actaastro.2009.07.018.
- [7] M. Gieras and A. Gorgeri, "Numerical modelling of the hybrid rocket engine performance," *Propulsion and Power Res.*, vol. 10, no. 1, pp. 15-22, 2021, doi: 10.1016/j.jppr.2021.03.001.
- [8] L. Wang, Y. Li, C. Li, and Z. Zhao, "CFD investigation of thermal and pressurization performance in LH₂ tank during discharge," *Cryogenics*, vol. 57, pp. 63-73, 2013, doi: 10.1016/j.cryogenics.2013.05.005.
- [9] L. Wang, Y. Li, Z. Zhao, and J. Zheng, "Numerical investigation of pressurization performance in cryogenic tank of new-style launch vehicle," *Asia-Pac. J. Chem. Eng.*, vol. 9, no. 1, pp. 63-74, 2014, doi: 10.1002/apj.1797.
- [10] Z. Zuo, W. Jiang, X. Qin, and Y. Huang, "A numerical model for liquid-vapor transition in self-pressurized cryogenic containers," *Appl. Therm. Eng.*, vol. 193, 2021, Art. no. 117005, doi: 10.1016/j.applthermaleng.2021.117005.
- [11] S. Ali, N. Abbas, S. A. Khan, I. Malik, and M. Mansha, "Chemical-based hydrogen storage systems: Recent developments, challenges, and prospectives," *Chem. Asian J.*, vol. 19, no. 16, p. e202400320, 2024, doi:10.1002/asia.202400320.
- [12] L. Yin, H. Yang, and Y. Ju, "Review on the key technologies and future development of insulation structure for liquid hydrogen storage tanks," *Int. J. Hydrogen Energy*, vol. 57, pp. 1302-1315, 2024, doi: 10.1016/j.ijhydene.2024.01.093.
- [13] W. Fan, Y. Ding, and Z. Xiao, "A brand new green coating technology for realizing the regulation of

- spherical propellant energy release process,” *Def. Technology*, vol. 36, pp. 78-94, 2024, doi: 10.1016/j.dt.2024.02.008.
- [14] L. Wang, Y. Ma, Y. Wang, F. Xie, and Y. Li, “Investigation on pressurization behaviors of two-side-insulated cryogenic tank during discharge,” *Int. J. Heat Mass Transf.*, vol. 102, pp. 703-712, 2016, doi: 10.1016/j.ijheatmasstransfer.2016.06.045.
- [15] J. Li, G. Liang, P. Zhu, and X. Wang, “Numerical investigation of the operating process of the liquid hydrogen tank under gaseous hydrogen pressurization,” *Aerosp. Sci. Technol.*, vol. 93, 2019, Art. no. 105327, doi: 10.1016/j.ast.2019.105327.
- [16] J. Li and G. LIANG, “Simulation of mass and heat transfer in liquid hydrogen tanks during pressurizing,” *Chin. J. Aeronaut.*, vol. 32, no. 9, pp. 2068-2084, 2019, doi: 10.1016/j.cja.2019.05.008.
- [17] L. Wang, Y. Li, Z. Zhao, and Z. Liu, “Transient thermal and pressurization performance of LO₂ tank during helium pressurization combined with outside aerodynamic heating,” *Int. J. Heat Mass Transf.*, vol. 62, no. 1, pp. 263-271, 2013, doi: 10.1016/j.ijheatmasstransfer.2013.03.021.
- [18] Y. Mitikov and O. Shynkarenko, “Reduction of the Pressurization System Final Mass for a Modern Rocket Launcher,” *J. Aerosp. Technol. Manage.*, vol. 14, 2022, Art. No. e0122, doi: 10.1590/jatm.v14.1238.
- [19] S. H. Yilmaz, E. Taskesen, K. Roshanaei, and M. Ozkaymak, “Energy Management with Intelligent Plug and Socket,” *Gazi Univ. J. Sci.*, vol. 35, no. 3, pp. 969-978, 2022, doi: 10.35378/gujs.933310.
- [20] S. Barsi and M. Kassemi, “Numerical and experimental comparisons of the self-pressurization behavior of an LH2 tank in normal gravity,” *Cryogenics*, vol. 48, no. 3, pp. 122-129, 2008, doi: 10.1016/j.cryogenics.2008.01.003.
- [21] C. H. Panzarella and M. Kassemi, “Self-pressurization of large spherical cryogenic tanks in space,” *J. Spacecr. Rockets*, vol. 42, no. 2, pp. 299-308, 2005, doi: 10.2514/1.4571.
- [22] D. A. Fester and P. E. Bingham, “Main Tank Injection (MTI) pressurization of liquid rocket propellant tanks,” in *Proc. 54th Int. Astronaut. Congr. Int. Astronaut. Fed. (IAF), Int. Acad. Astronaut., Int. Inst. Space Law*, 2003, doi: 10.2514/6.iac-03-iaa.2.3.06.
- [23] L. C. Yang, “Relevant mechanisms affecting the efficiency in detonation of energetic gaseous mixtures,” in *Proc. AIAA SciTech Forum Expo.*, 2024, doi: 10.2514/6.2024-2161.
- [24] R. Scholl, D. Freudenmann, and S. Schlechtriem, “Microencapsulation of hydrocarbon fuels for monopropellant creation with hydrogen peroxide,” *Fuel*, vol. 356, p. 129520, 2024, doi: 10.1016/j.fuel.2023.129520.
- [25] F. W. Childs, T. R. Horowitz, W. Jenisch, and B. Sugarman, “Design guide for pressurization system evaluation liquid propulsion rocket engines,” NASA, Tech. Rep. 2334, Nov. 1962.
- [26] Y. A. Cengel and M. A. Boles, *Thermodynamics: An Engineering Approach*, 9th ed. New York, NY, USA: McGraw-Hill, 2019.
- [27] M. R. Spiegel, S. Lipschutz, and J. Liu, *Schaum’s Outline: Mathematical Handbook of Formulas and Tables*, 2nd ed. New York, NY, USA: McGraw-Hill, 1998.
- [28] G. F. Pinder, *Numerical Methods for Solving Partial Differential Equations: A Comprehensive Introduction for Scientists and Engineers*, 1st ed. Hoboken, NJ, USA: Wiley, 2018.
- [29] A. F. El-Sayed, *Aircraft Propulsion and Gas Turbine Engines*, 2nd ed. New York, NY, USA: CRC Press, 2017, doi:10.1201/9781315156743.
- [30] C. Borgnakke and R. E. Sonntag, *Fundamentals of Thermodynamics*, 8th ed. Hoboken, NJ, USA: Wiley, 2013.
- [31] Z. Wang, Z. Shao, and H. Chen, “Robust sensor optimization for liquid propellant rocket engine model parameter estimation,” *IEEE Trans. Aerosp. Electron. Syst.*, vol. 60, no. 4, pp. 4994–5009, 2024, doi:10.1109/TAES.2024.3384176.

Research Article

3E Analysis of a Hybrid Biomass / Solar System for Power Generation and Desalination

¹* E. M. Leal , ²E. A. Teixeira 

¹ Department of Mechanical Engineering, School of Mining, Federal University of Ouro Preto, MG, Brazil.

² Graduate Program in Mechanical Engineering, School of Mining, Federal University of Ouro Preto, MG, Brazil.

E-mails: ¹*elisangelamleal@ufop.edu.br, edilberto.teixeira@aluno.ufop.edu.br

Received 27 July 2024, Revised 15 January 2025, Accepted 28 January 2025

Abstract

The study addresses global energy challenges by proposing a hybrid biomass and solar energy system for power generation and water desalination. A model is applied to two cities in Northeast Brazil (Natal-RN and Fortaleza-CE), targeting urban centers with waste and sunny coastal regions. Key variables include residue composition, heating value, and quantity, essential for energy efficiency assessment. Energy, exergy, and economic (3E) analyses using Scilab software compare four configurations: the base Rankine cycle, Rankine with an external superheater (ESH), Rankine with concentrated solar power (CSP), and Rankine with CSP integrated with desalination. Results show that higher pressures and temperatures enhance efficiency, reducing solar field area by 16% when pressure and temperature increase from 4.5 MPa/400°C to 6.5 MPa/500°C. Fortaleza-CE, with higher solar irradiation, requires smaller solar fields than Natal-RN. Integrating desalination into CSP cycles increases Levelized Cost of Energy (LCOE) by up to 7.6% and solar field area due to higher energy demands but provides potable water, with water recovery rates around 10% of seawater input. The findings underscore the importance of optimizing operating conditions and leveraging local solar resources to maximize socio-economic benefits.

Keywords: Hybrid system; biomass; solar energy; power generation; desalination.

1. Introduction

The increasing demand for energy highlights the need to implement renewable sources as safe, reliable, and economical alternatives while reducing greenhouse gas emissions and ensuring system resilience to fluctuations [1].

Renewable energy systems are categorized as single-source or hybrid systems. Single-source systems rely on one energy source, like wind or solar, supported by storage and electrical devices. Hybrid systems, however, combine two or more power generation options, integrating renewable and non-renewable sources along with storage and electrical components [2].

This paper explores renewable solutions for electricity generation and desalination in Brazil, emphasizing solar systems for fuel cost savings in regions with high solar potential. However, intermittency and battery life challenges necessitate integrating continuous energy sources such as geothermal, biomass, or ocean thermal energy [3].

Studies on thermodynamic and economic analyses of hybrid systems demonstrate their cost-effective and sustainable potential. Combined heat and power (CHP) systems improve efficiency through heat utilization for both power and heating. Advanced heat transfer strategies, including hybrid nanofluids (e.g., Al₂O₃-SiO₂/water) and magnetite nanofluids, significantly enhance convective heat transfer and reduce energy losses, showcasing innovative approaches in renewable energy systems [4], [5], [6], [7].

Table 1 highlights diverse applications of hybrid renewable energy systems that integrate solar, wind, biomass, and fuel cell technologies. These studies underline improvements in

efficiency, cost reduction, carbon footprint minimization, and innovative technological approaches to address energy demands and environmental goals.

Desalination is a key focus of this research due to water scarcity, with Earth's water being 96.5% oceanic. The Humidification-Dehumidification (HDH) process is chosen for its simpler design, lower temperatures, and atmospheric pressure operation, making it a cost-effective option for decentralized applications. However, HDH has lower energy efficiency and water recovery rates compared to advanced technologies like Reverse Osmosis (RO) [28], [29].

Reverse Osmosis (RO) is the most widely used desalination method due to its efficiency and scalability, with recovery rates of 40–60%. However, its higher energy consumption (2–6 kWh/m³ for seawater) and complex pre-treatment requirements increase costs. In contrast, HDH offers lower energy demands, making it suitable for regions with solar energy and limited infrastructure [29], [30].

Alternative desalination methods include Membrane Distillation (MD), which uses low-grade heat and achieves high salt rejection rates, and Electrodialysis (ED), effective for brackish water with lower energy consumption than RO. However, MD's higher costs and ED's limitations with high-salinity water make RO the preferred choice, while HDH remains a practical solution for decentralized regions with high-salinity water [31], [32].

Wind-powered desalination systems paired with RO or ED offer renewable solutions but require energy storage due to wind

intermittency, raising costs. HDH integrates seamlessly with solar energy, aligning with natural solar cycles, making it more cost-effective and sustainable for sun-rich, decentralized communities [33].

Biomass is highlighted as a renewable energy source capable of simultaneously producing energy, fuels, and bio-based materials. In Brazil, 81.8 million tons of municipal solid waste (MSW) were produced in 2022, with 61% disposed of in landfills. Biomass conversion to energy can be achieved via thermochemical and biochemical technologies, supporting the food-energy-water nexus [34], [35], [36].

The paper shows a novel energy, exergy, and economic (3E) approach of a hybrid biomass-solar system for electricity generation and desalination. The methodology includes literature review, technical analysis, and economic modeling to evaluate energy efficiency, heat transfer rates, and cost-effectiveness of the proposed system [37].

The study proposes a model applied to two cities in Brazil's Northeast, using Scilab software to compare hybrid and conventional cycles. Results show reduced fuel consumption and savings during peak sunlight hours. Solar integration in the desalination unit using HDH technology achieves approximately 10% efficiency, addressing energy challenges and water scarcity through innovative solutions.

2. Materials and Methods

To provide a clear overview of the study's workflow, Table 2 summarizes the steps followed for the technical, exergy, and economic analyses.

2.1 Characterization of the areas

The average daily global horizontal solar irradiation in Brazil ranges from 3.5 to 6.25 kWh/m² per year [38]. Figure 1 illustrates a solar map of Brazil displaying the values of global horizontal irradiance (GHI).

The study focuses on two Brazilian cities, Natal-RN (5°47'42"S, 35°12'32"W) and Fortaleza-CE (3°43'06"S, 38°32'34"W), both located in the northeastern region of Brazil, as shown in Figure 1.

Both cities (Fortaleza-CE and Natal-RN) benefit from high solar irradiation, with annual Global Horizontal Irradiance (GHI) values ranging between 5.5 to 6.5 kWh/m² per day (Figure 2), making them suitable for solar energy integration. Figure 2 shows that Fortaleza consistently exhibits slightly higher GHI values compared to Natal, offering an advantage in solar energy applications [39].

Regarding municipal solid waste (MSW) amount and biogas potential, both cities generate significant amounts of MSW. Natal produces 728.58 tons per day (tpd), with an estimated lower heating value (LHV) of 7,725.7 kJ/kg, while Fortaleza generates approximately 3,750.79 tpd with an LHV of 8,297.5 kJ/kg [40]. These waste streams are rich in organic matter, plastics, and paper, as described in Table 3, which are key contributors to biogas production. The average biogas composition includes 60% methane, 30% carbon dioxide, and minor components, yielding an LHV of 30 MJ/kg [41].

Table 3 shows the average gravimetric composition of municipal solid waste in Natal-RN and Fortaleza-CE, along with the results of the LHV value, which is calculated using equation (1), according to Kumar and Samader [42].

$$LHV_w = \sum_i x_i LHV_i \quad (1)$$

Where: x_i is the mass fraction of the residue and LHV_i is the lower heating value of each waste type.

Table 2. Summary of this work.

| Step | Description | Tools/Models | Outputs |
|-----------------------|---|-------------------------------|--|
| Area Characterization | Identification of solar and biomass potential in selected locations (Natal-RN, Fortaleza-CE). | Solar and waste data analysis | Input parameters for energy modeling. |
| Technical Analysis | Simulation of Rankine cycles under different configurations (base, CSP, desalination, etc.). | Scilab | System efficiency and performance metrics. |
| Exergy Analysis | Assessment of irreversibilities and second-law efficiencies for all components. | Exergy balance equations | Irreversibility hotspots and efficiency metrics. |
| Economic Analysis | Calculation of Levelized Cost of Energy (LCOE) and feasibility of each configuration. | LCOE formula | Financial feasibility and cost comparison |

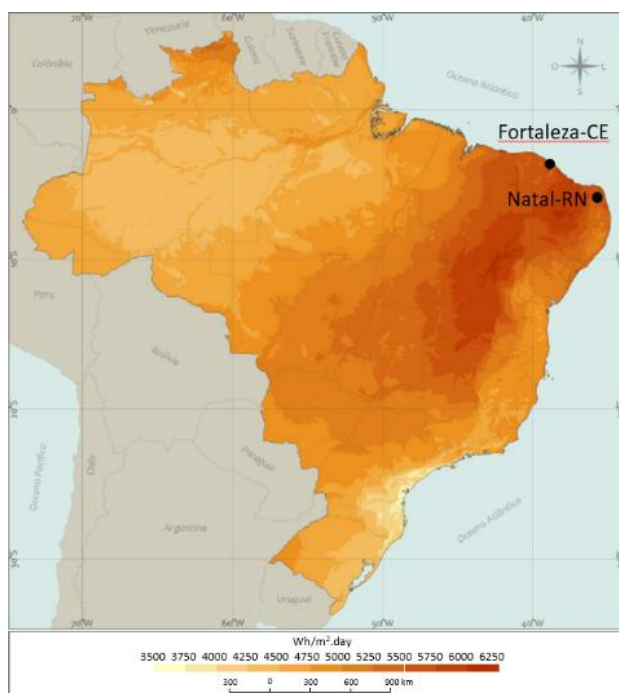


Figure 1. Annual Average Global Horizontal Irradiation in Brazil [38 adapted].

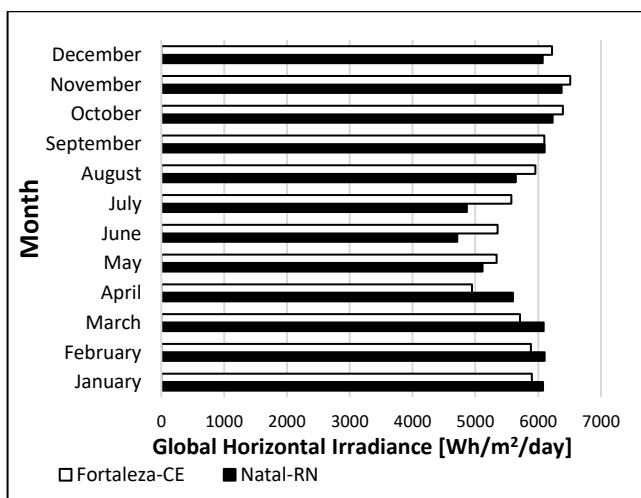


Figure 2. Monthly Average Global Horizontal Irradiation (GHI) in Natal-RN and Fortaleza-CE [39].

Table 3. Average Gravimetric Composition of MSW in Natal-RN, and Fortaleza-CE and Results of LHV.

| Waste Type | Natal-RN | | Fortaleza-CE | | LHV [kJ/kg] |
|-----------------------|-------------|--------------|---------------|------------|---------------|
| | LHV [kJ/kg] | % wt | LHV [kJ/kg] | % wt | |
| Organic Matter | 5485.2 | 33.5 | 1839.74 | 34.9 | 1914.34 |
| Paper / Cardboard | 16874.1 | 5.2 | 870.70 | 5.9 | 995.57 |
| Plastics / Tetra Pack | 26363.4 | 17.2 | 4539.77 | 18.7 | 4929.95 |
| Wood | 10543.7 | 0.7 | 73.81 | 0.2 | 21.09 |
| Textiles | 14551.9 | 2.8 | 401.64 | 3.0 | 436.56 |
| Other (recyclable) | NA | 40.6 | 0 | 37.3 | 0 |
| Total | | 100 | 7725.7 | 100 | 8297.5 |
| Reference | [43] | [44 adapted] | [45 adapted] | | |

2.2. Base Cycle, Hybrid Cycle, and Desalination Unit

The study is based on the Rankine cycle, analyzing four configurations: (a) base Rankine cycle using municipal solid waste (MSW) as the fuel (Figure 3), (b) a Rankine cycle with an external superheater fueled by biogas from MSW (Figure 4), (c) a hybrid cycle with boiler feedwater preheating using concentrated solar power (CSP) (Figure 5), and (d) a hybrid cycle using MSW as a fuel source with CSP-based boiler water preheating and a desalination unit (Figure 6).

These cycles include the following components: (A) condensing-extraction steam turbine coupled to an electrical generator, (B) mass-burning boiler fueled by MSW, (C) condensers, (D) heat exchangers, (E) cooling tower, (F) external superheater, (G) solar field, and (P) pumps.

In the base Rankine cycle (Figure 3), the working fluid is superheated in the boiler (B), expanded in the steam turbine (A), and condensed in the condenser (C1), where it is cooled to the saturated liquid state. It then passes through the pump (P2) and the heat exchanger (D1), where it is preheated using steam extracted from the turbine. After passing through pump (P1), the fluid is pressurized before returning to the boiler (B).

In the Rankine cycle with an external superheater (Figure 4), before entering the turbine, the working fluid is superheated in an external unit powered by biogas generated from MSW. This reduces the thermal load on the boiler, protecting its components by shifting the superheating process to an external device.

In the hybrid Rankine cycle (Figure 5), the boiler feedwater (B) is preheated as it passes through a heat exchanger (D2), which receives thermal energy from the solar field (G). The fluid circulating in the solar collector is thermal oil, which indirectly transfers heat to the boiler feedwater.

In the hybrid Rankine cycle with HDH desalination (Figure 6), the solar field (G) heats saline water, which can be either seawater or brackish water. The water is initially preheated in the heat exchanger (D3) using steam from the extraction-condensing turbine (A). It is then further heated and used to humidify dry air in the humidification chamber (D4). The humidified air, now carrying steam, passes through the dehumidification chamber (C2), where it meets cooled surfaces, leading to condensation and freshwater collection, while the dry air can be recirculated.

2.3. Technical Analysis

Energy and exergy analyses of cycles are accomplished for each component or system involved. The analysis of these cycles operates under the following assumptions [37], [46]: (i)

all thermodynamic processes are considered to be adiabatic (except solar collectors), and in steady state, (ii) kinetic and potential energy effects are negligible, (iii) heat loss from the pipes are negligible, (iv) at the inlet of the pumps, stream is assumed to be a saturated liquid, (v) at the inlet of the desalination process, stream from the turbine is a saturated vapor and at the outlet it is a saturated liquid, (vi) stream 14 to 15 are carried out at a constant temperature, and (vii) the water produced is pure water. The energy and exergy analyses for the cycles in Figures 3 to 6, are carried out using Scilab software and the equations provided in Table 4. Input data necessary for computational simulations are detailed in Table 5.

Table 4. Equations for the components/processes in the cycles.

| Equation |
|--|
| Extraction-condensing steam turbine (A) (* Rankine base / Rankine+ESH / Rankine+ESH+CSP) (**Rankine+ESH+CSP+Desal) |
| $\dot{m}_{in,Turb} = \dot{m}_{out,Turb} = \sum \dot{m}_{extr,Turb}$ (2) |
| $n_{pol} = (h_{in} - h_{out}) / (h_{in} - h_{out,s})$ (3) |
| $\dot{W}_{Turb} = \dot{m}_{in,Turb} (h_{in} - h_{1st\ ext}) + \sum \dot{m}_{extr,Turb} (h_{ext} - h_{out})$ (4) |
| $\dot{E}x_{in,Turb} = \dot{m}_{in,Turb} ex_{in,Turb} (*)$ (5) |
| $\dot{E}x_{out,Turb} = \dot{W}_{Turb} + \dot{m}_6 ex_6 + \dot{m}_7 ex_7 + \dot{E}x_{D,Turb} (*)$ (6) |
| $\dot{E}x_{in,Turb} = \dot{m}_{in,Turb} ex_{in,Turb} (**)$ (7) |
| $\dot{E}x_{out,Turb} = \dot{W}_{Turb} + \dot{m}_6 ex_6 + \dot{m}_7 ex_7 + \dot{m}_{14} ex_{14} + \dot{E}x_{D,Turb} (**)$ (8) |
| Mass-burning Boiler (B) |
| $\dot{Q}_B = \dot{m}_4 (h_5 - h_4) = \dot{m}_{MSW} LHV_{MSW} \eta_B + \dot{m}_{air} h_{air}$ (9) |
| $\dot{E}x_{in} = \dot{m}_4 ex_4 + \dot{m}_{MSW} LHV_{MSW} \eta_B \phi_{MSW} + \dot{m}_{air} ex_{air}$ (10) |
| $\dot{E}x_{out} = \dot{m}_{exh} ex_{exh} + \dot{m}_5 ex_5 + \dot{E}x_{D,B}$ (11) |
| Condenser (C1) |
| $\dot{Q}_{C1} = \dot{m}_6 (h_6 - h_1) = \dot{m}_9 (h_8 - h_9)$ (12) |
| $\dot{E}x_{in} = \dot{m}_6 ex_6 + \dot{m}_9 ex_9$ (13) |
| $\dot{E}x_{out} = \dot{m}_1 ex_1 + \dot{m}_8 ex_8 + \dot{E}x_{D,C1}$ (14) |
| Dehumidifier (C2) |
| $\dot{Q}_{C2} = \dot{m}_{21} h_{21} - (\dot{m}_{22} h_{22} + \dot{m}_{25} h_{25}) = \dot{m}_{cw} (h_{cw,out} - h_{cw,in})$ (15) |
| $\dot{E}x_{in} = \dot{m}_{21} ex_{21} + \dot{m}_{cw} ex_{cw}$ (16) |
| $\dot{E}x_{out} = \dot{m}_{22} ex_{22} + \dot{m}_{25} ex_{25} + \dot{m}_{cw} ex_{cw} + \dot{E}x_{D,C2}$ (17) |
| Heat Exchanger (D1) |
| $\dot{m}_7 h_2 + \dot{m}_7 h_7 = \dot{m}_3 h_3$ (18) |
| $\dot{E}x_{in} = \dot{m}_2 ex_2 + \dot{m}_7 ex_7$ (19) |
| $\dot{E}x_{out} = \dot{m}_3 ex_3 + \dot{E}x_{D,D1}$ (20) |
| Heat Exchanger (D2) |
| $\dot{Q}_{D2} = \dot{m}_{11} (h_4 - h_{11}) = \dot{m}_{12} (h_{12} - h_{13})$ (21) |
| $\dot{E}x_{in} = \dot{m}_{11} ex_{11} + \dot{m}_{12} ex_{12}$ (22) |
| $\dot{E}x_{out} = \dot{m}_4 ex_4 + \dot{m}_{13} ex_{13} + \dot{E}x_{D,D2}$ (23) |
| Heat Exchanger (D3) |
| $\dot{Q}_{D3} = \dot{m}_{14} (h_{15} - h_{14}) = \dot{m}_{19} (h_{20} - h_{19})$ (24) |
| $\dot{E}x_{in} = \dot{m}_{19} ex_{19} + \dot{m}_{14} ex_{14}$ (25) |
| $\dot{E}x_{out} = \dot{m}_{15} ex_{15} + \dot{m}_{20} ex_{20} + \dot{E}x_{D,D3}$ (26) |
| Humidifier (D4) |
| $\dot{Q}_{D4} = \dot{m}_{16} (h_{16} - h_{17}) = \dot{m}_{20} h_{20} + \dot{m}_{24} h_{24} - (\dot{m}_{21} h_{21} + \dot{m}_{23} h_{23})$ (27) |

Table 4. Equations for the components/processes in the cycles (continue).

| Equation | |
|---|------|
| SeaWater Specific Enthalpy (h_{sw}): $h_{sw} = h_w - [S(27062.623 + S) + S(4835.675 + S).T]$ | (28) |
| Validity [47]: h_{sw} and h_w in $\left(\frac{J}{kg}\right)$; $10 \leq \text{Temp } (T) \leq 120 \text{ } ^\circ\text{C}$; $0 \leq \text{Salinity } (S) \leq 0.12 \text{ kg/kg}$ | |
| SeaWater Specific Entropy (s_{sw}): $s_{sw} = s_w - S(-423.1 + 14630S - 98800S^2 + 309500S^3 + 25.62T - 0.1443T^2 + 5.879 \times 10^{-4}T^3 + 80.4S^2T + 0.3035ST^2 - 61.11ST)$ | (29) |
| Validity [47]: s_{sw} and s_w in $\left(\frac{J}{kg \cdot K}\right)$; $10 \leq \text{Temp } (T) \leq 120 \text{ } ^\circ\text{C}$; $0 \leq \text{Salinity } (S) \leq 0.12 \text{ kg/kg}$ | |
| $\dot{E}x_{in} = \dot{m}_{16}ex_{16} + \dot{m}_{20}ex_{20} + \dot{m}_{24}ex_{24}$ | (30) |
| $\dot{E}x_{out} = \dot{m}_{17}ex_{17} + \dot{m}_{21}ex_{21} + \dot{m}_{23}ex_{23} + \dot{E}x_{D,D4}$ | (31) |
| Cooling Tower (E) | |
| $\dot{m}_8h_8 + (\dot{m}_{air}h_{air})_{in} = \dot{m}_{10}h_{10} + (\dot{m}_{air}h_{air})_{out}$ | (32) |
| $\dot{E}x_{in} = \dot{m}_8ex_8 + \dot{m}_{air,in}ex_{air,in}$ | (33) |
| $\dot{E}x_{out} = \dot{m}_{10}ex_{10} + \dot{m}_{air,out}ex_{air,out} + \dot{E}x_{D,E}$ | (34) |
| Pumps (P1 / P2 / P3 / P4 / P5) | |
| $\dot{W}_P = \dot{m}_{in} v_{in}(P_{out} - P_{in}) = \dot{m}_{in} (h_{out} - h_{in}) \eta_P$ | (35) |
| $\dot{E}x_{in} = \dot{m}_{in}ex_{in} + \dot{W}_P$ | (36) |
| $\dot{E}x_{out} = \dot{m}_{out}ex_{out} + \dot{E}x_{D,P}$ | (37) |
| External Superheater (ESH) | |
| $\dot{Q}_{ESH} = \dot{m}_5(h_{5b} - h_{5a}) = \dot{m}_{bio} LHV_{bio} \eta_{ESH} + \dot{m}_{air}h_{air}$ | (38) |
| $\dot{E}x_{in} = \dot{m}_5ex_{5a} + \dot{m}_{bio} LHV_{bio} \eta_{ESH} \phi_{bio} + \dot{m}_{air}ex_{air}$ | (39) |
| $\dot{E}x_{out} = \dot{m}_{exh,g}ex_{exh} + \dot{m}_5ex_{5b} + \dot{E}x_{D,ESH}$ | (40) |
| Dehumidifier (C2) | |
| $\dot{Q}_{D2} = \dot{m}_{11}(h_4 - h_{11}) = \dot{m}_{12}(h_{12} - h_{13})$ | (41) |
| $\dot{E}x_{in} = \dot{m}_{11}ex_{11} + \dot{m}_{12}ex_{12}$ | (42) |
| $\dot{E}x_{out} = \dot{m}_4ex_4 + \dot{m}_{13}ex_{13} + \dot{E}x_{D,D2}$ | (43) |
| Solar Field (G) | |
| $\dot{Q}_{in,sun} = \eta_{col} I A_{sun}$ | (44) |
| $A_{SF} = \dot{Q}_{col} / [\eta_g DNI \cos(\theta)]$ | (45) |
| $\dot{Q}_{HTF} = \dot{m}_{HTF} C_{p,HTF} (T_{out} - T_{in})$ | (46) |
| System | |
| $\sum \dot{m}_{in} - \sum \dot{m}_{out} = 0$ | (47) |
| $ex = ex^{ph} + ex^{ch} = [(h - h_0) - T_0(s - s_0) + \sum n_i(\mu_i - \mu_{i,0})]$ | (48) |
| Thermal Efficiency (Rankine Base - R) | |
| $\eta_{th,R} = \frac{\dot{W}_{Turb} - \sum \dot{W}_P - \dot{Q}_{exh}}{\dot{Q}_{MSW}}$ | (49) |
| Thermal Efficiency (Rankine+ESH - RESH) | |
| $\eta_{th,RESH} = \frac{\dot{W}_{Turb} - \sum \dot{W}_P - \dot{Q}_{exh}}{\dot{Q}_{MSW} + \dot{Q}_{bio}}$ | (50) |
| Thermal Efficiency (Rankine + CSP - RCSP): | |
| $\eta_{th,RCSP} = \frac{\dot{W}_T - \sum \dot{W}_P - \dot{Q}_{exh}}{\dot{Q}_{MSW} + \dot{Q}_{in,sun}}$ | (51) |
| Thermal Efficiency (Rankine + CSP + Desal - RCSPD): | |
| $\eta_{th,RCSPD} = \frac{\dot{W}_T - \sum \dot{W}_P - \dot{Q}_{exh} + \dot{Q}_{D3} + \dot{Q}_{D4}}{\dot{Q}_{MSW} + \dot{Q}_{in,sun}}$ | (52) |

2.4. Economic Analysis

The levelized cost of energy (LCOE) is a key metric for evaluating and comparing energy generation methods. It represents the average total cost of building and maintaining an energy-producing system per unit of electricity generated over its expected lifetime [48].

LCOE is fundamental in the initial assessment of energy projects, helping determine feasibility and compare different energy ventures. It is calculated by dividing the present value of total project costs by the present value of electricity generated over the system's lifetime [49].

The significance of LCOE lies in its ability to assess project profitability. If the LCOE indicates unprofitability, companies may choose not to proceed with construction and consider alternative options. As a fundamental step in energy sector analysis, LCOE helps guide decision-making regarding investment and project viability [48]. The LCOE can be calculated using equation (53).

$$LCOE = \left[\sum_{t=1}^n \frac{I_t + M_t + F_t}{(1+r)^t} \right] / \left[\sum_{t=1}^n \frac{E_t + E_{DU}}{(1+r)^t} \right] \quad (53)$$

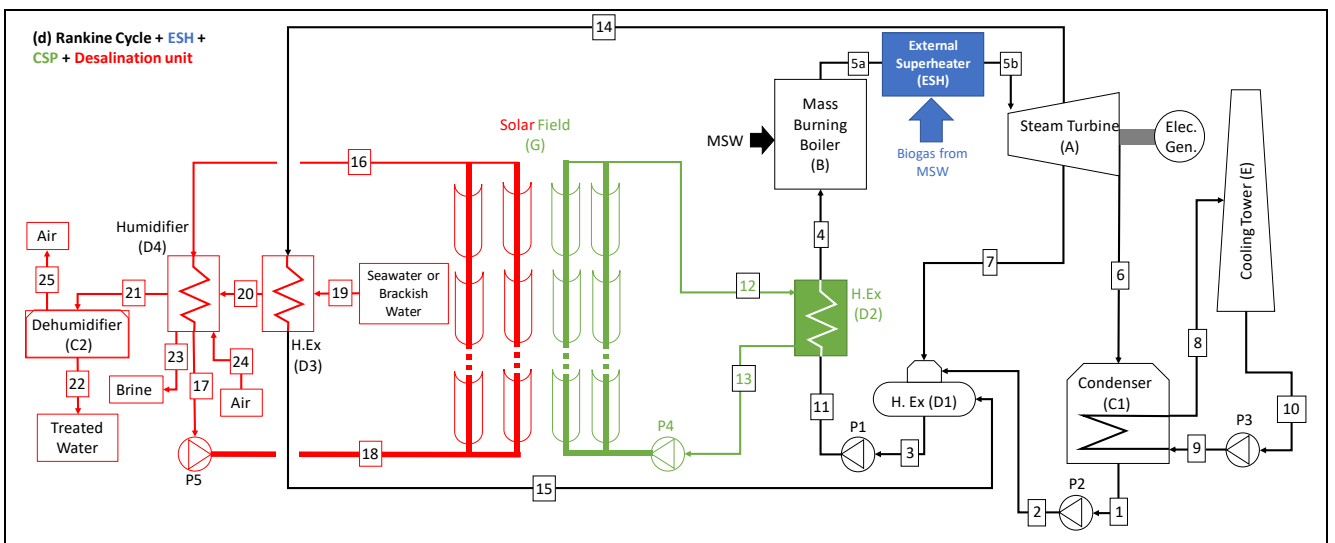
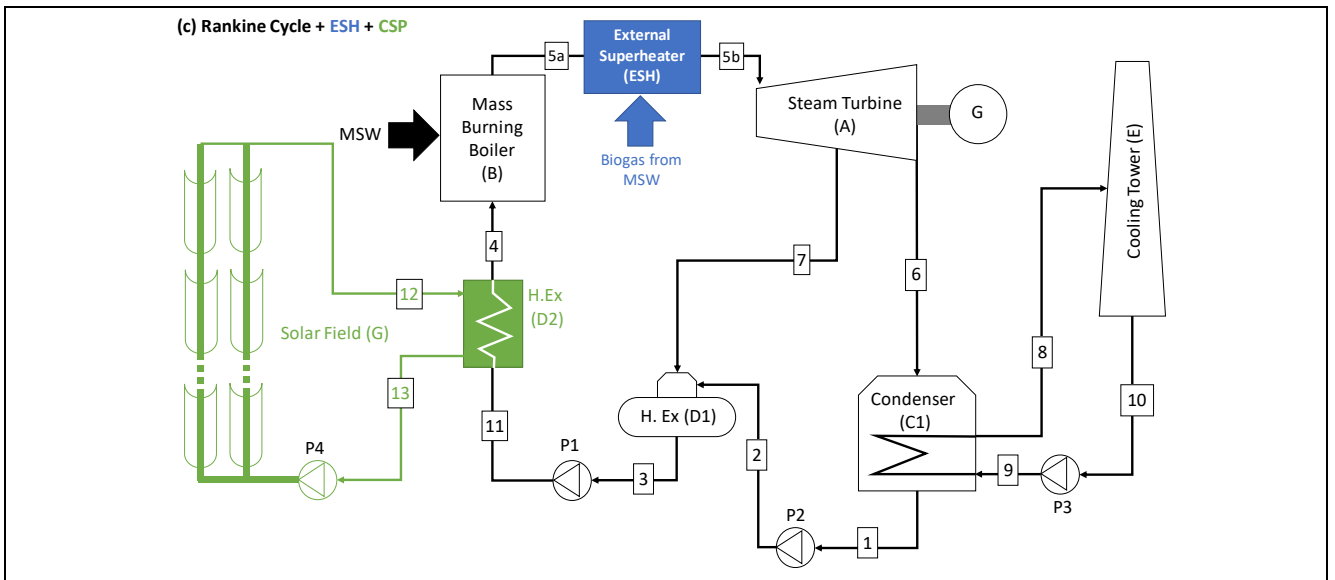
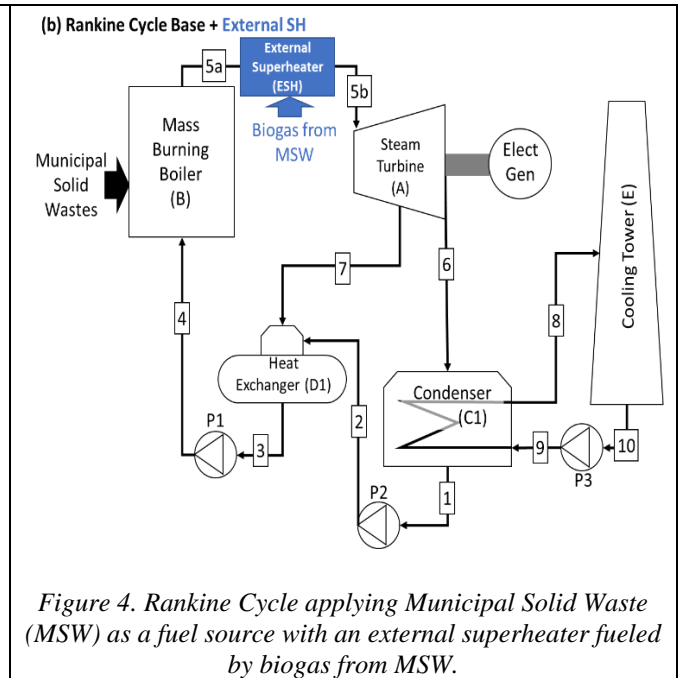
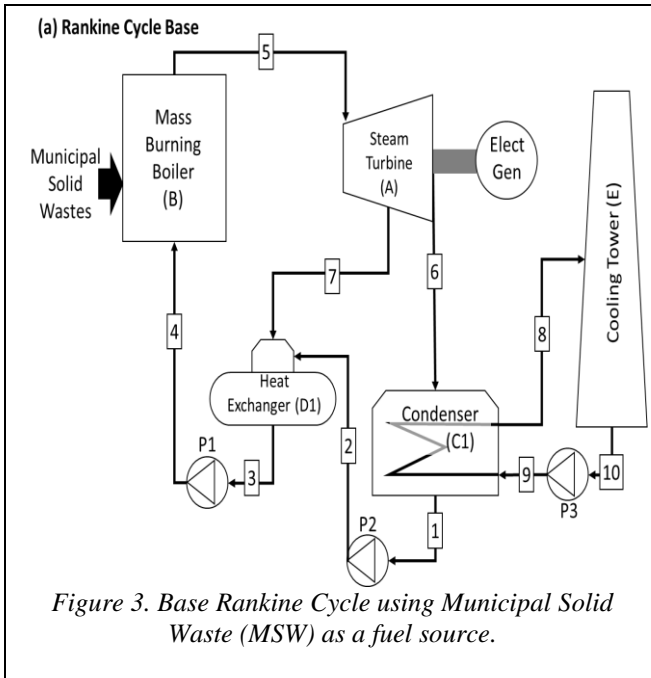
Where I_t are the investment costs in year t, comprising the initial price of the components, fuel handling equipment and installation cost, other equipment cost, balance of the plant and contingencies, M_t represents the operations and maintenance costs in year t, F_t are fuel costs in year t, E_t is the energy generation in year t, E_{DU} is the energy used in the desalination unit, r is the discount rate and n is the life of the system (25 years). In addition, the parameters for the economic analysis of the power plants are summarized in Table 6.

Table 5. Technical parameters of the system applied in the model.

| Input Data | Unit | Natal / RN | Fortaleza/ CE |
|--|------------------------|---|---|
| Municipal Solid Waste (MSW) | | | |
| Lower Heating Value (LHV) | kJ/kg | 7725.7 [44] | 8297.5 [45] |
| Biogas Lower Heating Value (LHV) | MJ/kg | 10 [51] | 10 [51] |
| Cycle Power | MW | 1 | 1 |
| Boiler efficiency (η_B) | % | 87 [52] | 87 [52] |
| Amb. temperature (reference state) | $^\circ\text{C}$ | 25 [38], [39] | 25 [38], [39] |
| Amb. pressure (reference state) | kPa | 101.325 [38], [39] | 101.325 [38], [39] |
| Solar collector efficiency | - | 0.5 [37] | 0.5 [37] |
| Global Horiz. Irrad. (GHI) | | | |
| Higher value | Wh/m ² /day | 6372 [38], [39] | 6513 [38], [39] |
| Lower value | day | 4712 [38], [39] | 4947 [38], [39] |
| Boiler feed water temperature | | | |
| Without preheating | $^\circ\text{C}$ | 50 [52] | 50 [52] |
| With preheating | | 200 [52] | 200 [52] |
| Turbine Inlet Pressure and Temperature (steam) | MPa, $^\circ\text{C}$ | 4.5 MPa, 400 $^\circ\text{C}$ 5.0 MPa, 450 $^\circ\text{C}$ 6.5 MPa, 500 $^\circ\text{C}$ | 4.5 MPa, 400 $^\circ\text{C}$ 5.0 MPa, 450 $^\circ\text{C}$ 6.5 MPa, 500 $^\circ\text{C}$ |
| Turbine condens. pressure | kPa | 10 [53] | 10 [53] |
| Turbine polytropic efficiency | | 0.85 [54] | 0.85 [54] |
| Salt content (raw seawater) | g/kg | 35 [37] | 35 [37] |
| Seawater inlet temperature | $^\circ\text{C}$ | 15 [37] | 15 [37] |

Table 6. Parameters for the economic analysis [37],[50].

| Parameter | Value |
|------------------------------------|-----------------------------|
| Analysis period | 25 years |
| Site improvement | 20 \$/m ² |
| Solar field | 300 \$/m ² |
| Desalination unit | 1500 \$/m ³ /day |
| EPC and owner cost | 10% of direct cost |
| Power plant (base) | 1150 \$/kWe |
| Power plant (base) + ESH | 1200 \$/kWe |
| Total land area | 2.470 \$/m ² |
| EPC and owner cost [% direct cost] | 10% |
| Operation and maintenance cost | 55 \$/kW-year |



2.5 Preliminary CO₂ Emission Analysis

A preliminary assessment of CO₂ emissions avoided by the hybrid biomass-solar system is conducted to evaluate its environmental benefits. The analysis considers energy contributions from the boiler and external superheater (ESH), both powered by municipal solid waste (MSW) in its raw form and as biogas. Since MSW is a renewable biomass resource, its combustion is regarded as carbon-neutral, as the CO₂ released equals the amount absorbed during biomass growth.

The avoided emissions are estimated by comparing the energy supplied by the boiler and ESH to a coal-fired power plant with an average emission factor of 0.9 kg CO₂ per kWh [55]. The methodology involves calculating the total energy produced and the corresponding CO₂ reductions achieved by substituting fossil fuels. Key assumptions include: (i) biomass energy content is based on its lower heating value (LHV), (ii) solar energy contributions are considered emission-free, and (iii) the energy consumption of auxiliary components is factored into the calculations. Equation (54) calculates the emissions avoided (E_{av}).

$$E_{av} = E_{gen} \times EF \quad (54)$$

Where: E_{gen} is the total energy generated (kWh) and EF is the emission factor for fossil fuel systems (kg CO₂ /kWh).

3. Results and Discussion

The results are divided in four sections: (i) solar concentrator, (ii) power and exergy rate, (iii) LCOE, and (iv) preliminary CO₂ emission analyses of each cycle. Figures 2 to 6, and Tables 3 to 6 are used as a base of the performed analyses.

3.1. Solar Concentrator Results

The solar concentrator model used in the analysis is a full-tracking type, with $\cos(\theta)$ assumed to be 1 [50], [56]. A heat transfer fluid (HTF) is required to collect heat from the solar field. It is a synthetic thermal oil selected for its high thermal stability (up to 400°C) and low viscosity, ensuring efficient heat transfer and pumping performance. The HTF inlet and outlet temperatures are set at 250°C and 100°C, based on typical operating ranges for synthetic thermal oils in CSP systems [58]. The thermodynamic properties of the HTF follow the XCEL THERM® MK1 catalog [59], which is chemically equivalent to DOW THERM® A and Therminol® VP-1. The solar field area, determined according to the power requirements of the CSP-integrated cycles, is showed in Table 7.

Table 7 compares different Concentrated Solar Power (CSP) cycle configurations in Natal and Fortaleza, analyzing their performance under varying Global Horizontal Irradiance (GHI) conditions. The cities exhibit different maximum and minimum GHI values, impacting CSP system efficiency.

For CSP cycles without desalination, results indicate that as pressure and temperature increase (from 4.5 MPa/400°C to 6.5 MPa/500°C), the required solar field area decreases due to improved thermodynamic efficiency. Fortaleza, with slightly higher GHI, requires a smaller solar field than Natal, demonstrating the impact of local solar insolation on field area requirements.

In CSP cycles with desalination, the solar field area is significantly larger due to the higher power demand of the desalination process. However, similar to cycles without desalination, increasing pressure and temperature reduces the required solar field area. Fortaleza, benefiting from higher GHI, requires a smaller area than Natal.

Table 7. Results of Solar Field Area based on Power Requirements for the Cycles.

| Cycle | Solar Power | Natal-RN | | Fortaleza-CE | |
|--------------------------------------|-------------|----------------------|----------------------|----------------------|----------------------|
| | | Solar Field Area (1) | Solar Field Area (2) | Solar Field Area (1) | Solar Field Area (2) |
| Rank+ESH +CSP (4.5 MPa; 400°C) | 113.57 kW | 237.6 m ² | 321.4 m ² | 232.5 m ² | 306.1 m ² |
| Rank+ESH +CSP (5.0 MPa; 450°C) | 105.24 kW | 220.2 m ² | 297.8 m ² | 215.4 m ² | 283.6 m ² |
| Rank+ESH +CSP (6.5 MPa; 500°C) | 96.28 kW | 201.5 m ² | 272.4 m ² | 197.1 m ² | 259.5 m ² |
| Rank+ESH +CSP+Desal (4.5 MPa; 400°C) | 130.70 kW | 273.5 m ² | 369.8 m ² | 267.6 m ² | 352.3 m ² |
| Rank+ESH +CSP+Desal (5.0 MPa; 450°C) | 123.07 kW | 257.5 m ² | 348.2 m ² | 251.9 m ² | 331.7 m ² |
| Rank+ESH +CSP+Desal (6.5 MPa; 500°C) | 115.03 kW | 240.7 m ² | 325.5 m ² | 235.5 m ² | 310.0 m ² |

(1) using maximum GHI value (2) using minimum GHI value
 Rank+ESH+CSP: Rankine Cycle with an External Superheater, and Concentrated Solar Power
 Rank+ESH+CSP+Desal: Rankine Cycle with an External Superheater, Concentrated Solar Power, and a Desalination unit

Power input for cycles with desalination is substantially higher, highlighting the energy-intensive nature of the process. Although efficiency improves with increased pressure and temperature, reductions in solar field area are less pronounced due to the scale of energy requirements. Both Natal and Fortaleza follow similar trends in how operating conditions influence solar field needs, while differences in solar field areas between maximum and minimum GHI values highlight the sensitivity of CSP systems to variations in solar insolation.

3.2. Power and exergy rate analyses of the cycles

Figure 7 shows the results of power, exergy rate, energy, and exergy efficiency analysis for each cycle. Figure 8 provides the exergy balance for the equipment in the hybrid system, including the desalination unit, detailing the input, output, irreversibility, and second law efficiency for each component.

Figure 7 illustrates how energy and exergy efficiencies vary with pressure, temperature, and cycle configurations. Higher efficiencies occur at 6.5 MPa and 500°C, with the best results in hybrid cycles combining ESH and CSP without desalination. The inclusion of desalination slightly decreases efficiency due to its added energy demand, but it provides the benefit of potable water production.

Net power and exergy production remain stable, peaking at 986 kW in the most efficient cycles. However, desalination cycles show lower net power output, especially at 4.5 MPa and 400°C, due to the higher energy requirements of the process.

Hybrid cycles with desalination demand higher energy and exergy inputs, but these are reduced at higher pressures and temperatures, improving energy utilization. Fortaleza-CE has a slight efficiency advantage over Natal-RN due to higher solar radiation levels, particularly in CSP-integrated cycles, where solar insolation directly impacts performance. However, both cities show similar efficiency trends, improving at higher pressures and temperatures.

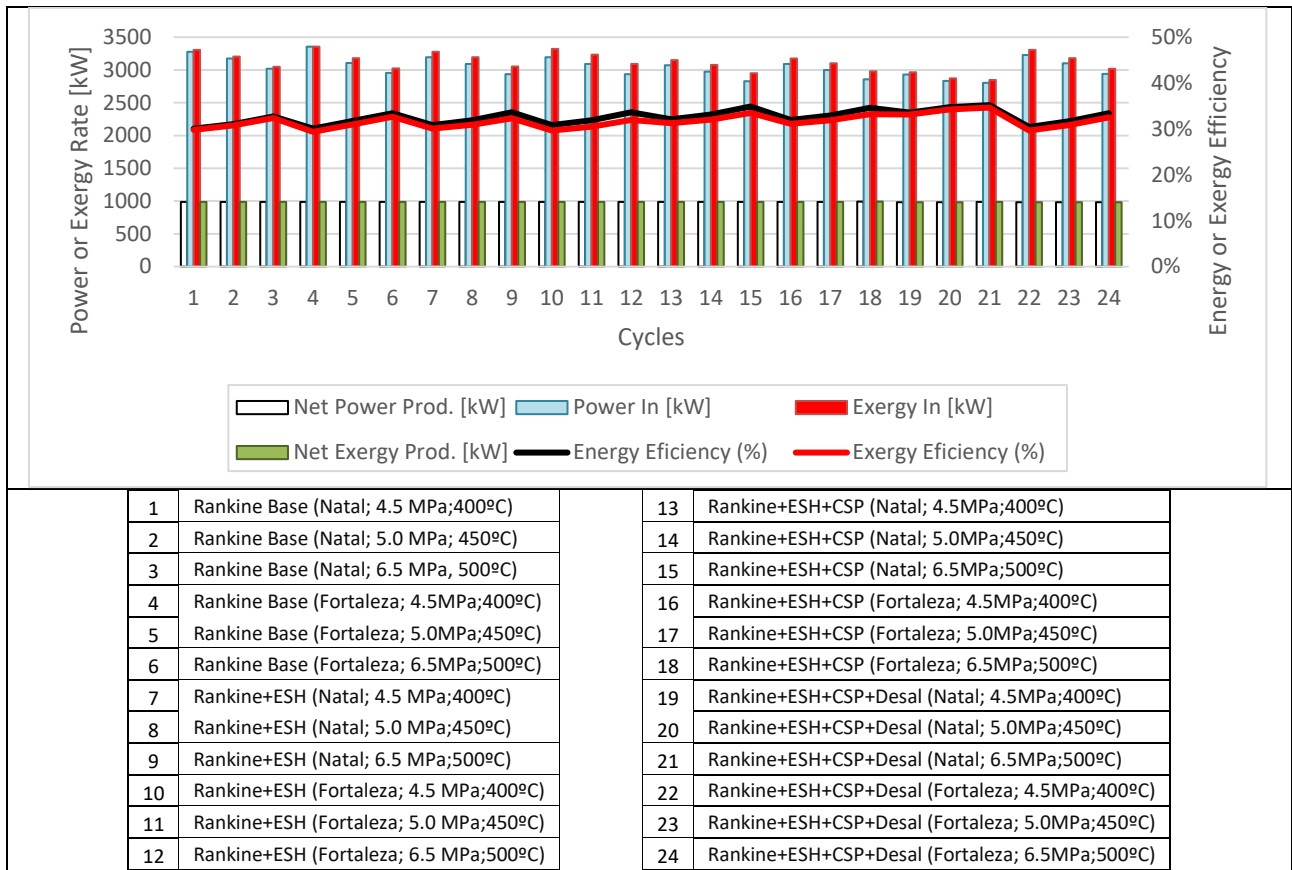


Figure 7. Results of Power, Exergy Rate, Energy, and Exergy Efficiency across the analyzed cycles.

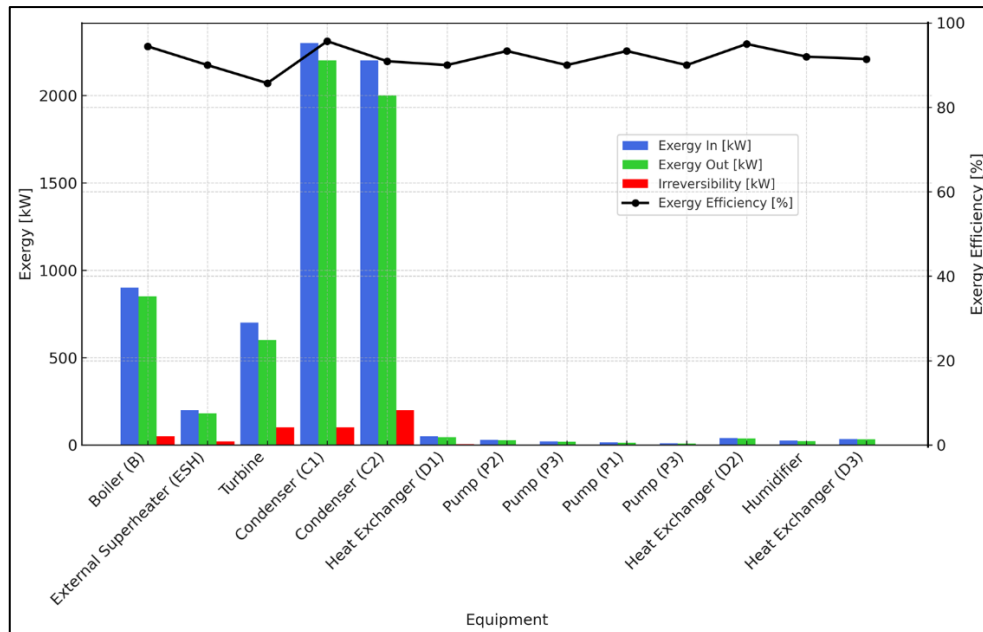


Figure 8. Results of Exergy Balance and Efficiency of the Hybrid Cycle with HDH Desalination Unit.

To enhance system performance, targeting inefficient components like the external superheater and desalination unit is decisive. Implementing advanced desalination technologies such as multi-effect distillation (MED) or reverse osmosis (RO) could reduce energy consumption and improve economic feasibility. Additionally, optimizing operating conditions and leveraging local solar potential are key to maximizing energy and exergy efficiency.

Figure 8 shows the hybrid cycle's performance, where second-law efficiency varies significantly among components. The boiler (B) has a high exergy input (~1200 kW) but operates

at a low efficiency (42.7%), indicating substantial irreversibilities that could be mitigated through thermal design improvements. Similarly, the external superheater (ESH), with an exergy input of 300 kW and an efficiency of 50%, also indicates opportunities for reducing losses. In contrast, the turbine operates at 94% efficiency, effectively converting exergy into useful work, making it a key contributor to system performance. Overall, improving the boiler and ESH would enhance the system's energy utilization.

Table 8 provides a detailed thermodynamic analysis of the hybrid cycle with HDH desalination, corresponding to the pipe

numbering in Figure 6. The variations in mass flow rate, pressure, temperature, enthalpy, entropy, and exergy demonstrate the system's complexity. High-energy points (e.g., pipes 5b, 7, and 14) indicate critical energy transformation zones, where optimization could improve overall efficiency.

The desalination unit's performance (streams 19a to 25) shows that the treated water (TW, stream 22) accounts for ~10% of the total seawater input (SW, stream 19a), indicating substantial water loss. While expected due to the technology's inherent inefficiencies, this highlights the need for optimization to improve water recovery rates.

Temperature, pressure, and enthalpy variations across streams reveal heat and energy demands of the desalination process. The brine output (stream 23) retains a significant amount of energy, suggesting potential losses. The differences in entropy and exergy between input (stream 19a) and output streams (22, 23) emphasize irreversibilities in the desalination unit.

Treated water (stream 22) emerges with low exergy, indicating a simple but inefficient process. This suggests opportunities for improvement, such as alternative desalination methods or heat integration strategies to recover energy from brine (stream 23).

Table 8. Thermodynamic Properties of the Hybrid Cycle with an HDH Desalination Unit (6.5 MPa/500°C).

| Pipe number | \dot{m} [kg/s] | P [kPa] | T [°C] | h [kJ/kg] | s [kJ/kg.K] | ex [kJ/kg] |
|-------------|------------------|---------|--------|-----------|-------------|------------|
| 1 | 0.779 | 10 | 45.81 | 191.81 | 0.6492 | 2.80 |
| 2 | 0.779 | 1200 | 45.88 | 193.15 | 0.6496 | 4.02 |
| 3 | 0.998 | 1000 | 179.89 | 762.68 | 2.1384 | 129.67 |
| 4 | 0.998 | 6950 | 200 | 854.62 | 2.3223 | 166.78 |
| 5a | 0.998 | 6500 | 300 | 2863.46 | 6.0018 | 1078.57 |
| 5b | 0.998 | 6500 | 500 | 3417.12 | 6.8397 | 1382.41 |
| 6 | 0.793 | 1000 | 248.59 | 2940.1 | 6.9206 | 881.27 |
| 7 | 0.014 | 1000 | 248.59 | 2940.1 | 6.9206 | 881.27 |
| 8 | 25.586 | 195 | 30 | 125.92 | 0.4367 | 0.27 |
| 9 | 25.586 | 200 | 15.01 | 63.20 | 0.2245 | 0.82 |
| 10 | 25.586 | 100 | 15 | 63.08 | 0.2245 | 0.70 |
| 11 | 0.998 | 100 | 181 | 770.63 | 2.1401 | 137.11 |
| 12 (HTF) | 0.378 | 150 | 250 | 738 | 1.0698 | 158.65 |
| 13 (HTF) | 0.378 | 130 | 100 | 515 | 0.7272 | 37.79 |
| 14 | 0.205 | 1050 | 254.14 | 2950.56 | 6.9189 | 892.24 |
| 15 | 0.205 | 1000 | 180 | 2777.43 | 6.5856 | 818.48 |
| 16 (HTF) | 0.107 | 150 | 250 | 439.8 | 1.3646 | 290.86 |
| 17 (HTF) | 0.107 | 130 | 100 | 153.1 | 1.0600 | 91.94 |
| 18 (HTF) | 0.107 | 200 | 105 | 523 | 0.7657 | 34.33 |
| 19a (SW) | 0.100 | 100 | 15.00 | 63.02 | 0.2244 | 0.72 |
| 19b (SW) | 0.100 | 200 | 15.04 | 63.16 | 0.2250 | 0.68 |
| 20 (SW) | 0.100 | 180 | 21.58 | 90.54 | 0.3190 | 0.07 |
| 21 (Mix) | 0.113 | 160 | 85.00 | 2299.0 | 1.2497 | 30.01 |
| 22 (TW) | 0.010 | 100 | 85.00 | 355.90 | 1.1340 | 22.30 |
| 23 (Br) | 0.090 | 100 | 85.00 | 373.85 | 1.1697 | 38.45 |
| 24 (Air) | 0.013 | 100 | 25.00 | 298.60 | 6.8630 | 0.00 |
| 25 (Air) | 0.013 | 105 | 85.00 | 359.63 | 7.0480 | 5.87 |

By reducing exergy losses and improving water recovery rates, the hybrid system could better integrate desalination, contributing to both energy and water sustainability.

3.3. LCOE analyses of the cycles

The Levelized Cost of Energy (LCOE) analysis is showed in Figure 9.

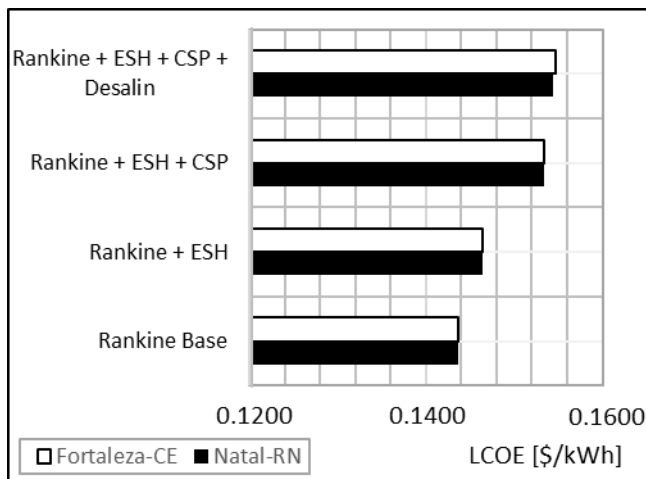


Figure 9. LCOE Comparison for Cycle Configurations in Natal and Fortaleza.

Figure 9 illustrates the Levelized Cost of Energy (LCOE) for four cycle configurations in Natal-RN and Fortaleza-CE. For the simplest cycle, Rankine Base, the LCOE is the same for both cities at 0.1436 US\$/kWh. As components are added, the LCOE gradually increases. For example, in the Rank+ESH+CSP configuration, Natal shows an LCOE of 0.1533 US\$/kWh, while Fortaleza is slightly higher at 0.1534 US\$/kWh, a difference of 0.13%. In the most complex cycle, Rankine cycle with external superheater, concentrated solar power and a desalination unit (Rank+ESH+CSP+Desal), Natal reaches 0.1544 US\$/kWh, and Fortaleza increases to 0.1546 US\$/kWh, showing a 0.10% difference. These differences highlight the consistency in costs between the two cities despite local variations in solar insolation and operational conditions.

3.4. Environmental Benefits: CO₂ Emission Reductions

The results highlight the hybrid system's potential to significantly reduce CO₂ emissions by utilizing municipal solid waste (MSW) as the primary energy source for the boiler and the external superheater (ESH). By using this biomass, which would otherwise be disposed of and potentially release greenhouse gases, the system avoids emissions correlated to conventional coal-fired power plants.

For the cities studied, the avoided emissions are approximately 2561.54 kg of CO₂ per operational hour in Fortaleza-CE and 2556.05 kg of CO₂ per operational hour in Natal-RN. These values account for the energy provided by the boiler and ESH, which collectively generate 2216.99 kW and 629.16 kW in Fortaleza-CE, and 2219.50 kW and 620.56 kW in Natal-RN, respectively. The calculations assume an average emission factor of 0.9 kg CO₂eq per kWh for coal-based power plants.

This reduction demonstrates the environmental advantages of the hybrid system, as it not only influences renewable energy sources but also promotes waste valorization by converting MSW into useful energy. Future studies could expand this analysis by including emissions interrelated to the collection, transportation, and processing of MSW, offering a more comprehensive evaluation of the system's life cycle environmental impact.

4. Conclusion

The 3E analysis highlights the potential of a hybrid biomass-solar system for addressing energy and water challenges in regions with high solar potential and agricultural residues. Higher operating pressures and temperatures improve efficiency and reduce solar field area, particularly benefiting cities with higher GHI, like

Fortaleza. Integrating desalination increases energy demand and costs but provides potable water, addressing water scarcity in arid regions. Additionally, utilizing municipal solid waste and solar energy significantly reduces CO₂ emissions compared to conventional systems. Optimizing conditions can lower the LCOE, making the system feasible for areas with limited water access.

This study provides a comprehensive evaluation of hybrid systems combining biomass and solar energy, offering novel insights into energy, exergy, and economic performance. It demonstrates the feasibility of integrating desalination with CSP, addressing dual challenges of energy production and water scarcity. The research also highlights the environmental benefits of reducing CO₂ emissions through renewable energy sources and waste valorization.

Future research should explore advanced desalination technologies, such as multi-effect distillation (MED) or reverse osmosis (RO), to improve water production efficiency. Improved thermal storage materials, including molten salts or supercritical CO₂, could enhance overall system performance. Additionally, conducting comprehensive sensitivity analyses and life-cycle assessments will help refine economic and environmental sustainability, ensuring broader applicability and optimization of hybrid systems.

Statements and Declarations

The authors declare that they have no known competing financial interests or personal relationships that could have appeared to influence the work reported in this paper.

Acknowledgements

The authors would like to acknowledge the Graduate Program of Mechanical Engineering of the Federal University of Ouro Preto.

Nomenclature

A : area (m²)
 GHI : Global Horizontal Irradiation (Wh.m⁻².day⁻¹)
 $\dot{E}x$: Exergy rate (kW)
 $\dot{E}x_D$: Destroyed exergy rate (kW)
 h : specific enthalpy (kJ.kg⁻¹)
 LHV : lower heating value (kJ.kg⁻¹)
 \dot{m} : mass flow rate (kg.s⁻¹)
 n_{pol} : polytropic efficiency (dimensionless)
 P : Pressure (kPa)
 $Pol.$: Polytropic
 \dot{Q} : heat transfer rate (kW)
 s : specific entropy (kJ.kg⁻¹.K⁻¹)
 T : temperature (K)
 v : specific volume (m³.kg⁻¹)
 \dot{W} : Power (kW)
 η : efficiency (dimensionless)
 φ : Exergy factor (dimensionless)

Subscript

air : relative to air
 amb : ambient conditions
 B : boiler
 bio : biogas fuel
 col : solar collector
 $cond$: condenser
 cw : cooling water
 des : destruction
 $desal$: desalination unit
 $extr$: extract
 exh : exhaust gases
 ESH : external superheater
 gen : generator
 HTF : heat transfer fluid (thermal oil)

$H.Ex$: heat exchanger
 in : inlet
 MSW : municipal solid wastes
 oil : relative to the thermal oil (HTF)
 out : outlet
 P : pump
 s : isentropic
 sun : relative to the sun
 SW : seawater
 SF : solar field
 $Turb$: turbine

Appendix

Table 1. Literature review on hybrid systems with solar / biomass and/or desalination.

| Investigated System | Findings | Software used | Ref. |
|--|--|-----------------------------------|------|
| Concentrated solar power (CSP)-biomass hybrid plant for combined heat and power | Design and performance of a CSP-biomass plant for combined heat and power with waste heat utilization. 16.6 MW parabolic trough collector field, 10 MW biomass boilers, 4 MW ORC, 93.6% efficiency. Successful demonstration of CSP-biomass hybridization. | TRNSYS | [8] |
| Solar-biomass hybrid power plant in Ludhiana district, Punjab | Techno-economic feasibility analysis of solar-biomass system. Utilization of hybrid systems to overcome discontinuity in solar and wind power. Potential of the available biomass is 62.73 MW. Total connected load of the village cluster under study is 97 MW. | Homer | [9] |
| Hybrid solar photovoltaic-biomass gasifier system for electricity generation | Development of electric power generation system based on hybrid solar PV and biomass gasifier for rural regions of Central and South America. System includes rice and coffee husks for syngas. | Matlab | [10] |
| Biomass-solar on-grid hybrid power generation system for Burdur Mehmet Akif Ersoy University Istiklal Campus | Optimum system: 5000 kW photovoltaic panels, 1500 kW biomass generator, grid assistance of 3000 kW. Net present cost of USD 18.8 million, cost of energy of USD 0.107/kWh, and renewable fraction is 49.4%. | RET Screen | [11] |
| Biomass steam generator integrated with linear Fresnel solar field | Evaluation of biomass steam generator at partial loads integrated with solar field. Model verification using on-site measurement data. 50 t/h superheated steam at 420°C/45 bar(a), efficiency evaluation with ASME PTC4 standard. | EES (Engineering Equation Solver) | [12] |
| Concentrated solar power (CSP)-biomass hybrid power plants | Profitability assessment of CSP-biomass hybrid plants in electricity markets. Stochastic simulations conducted to capture uncertainty. | Matlab | [13] |
| Concentrated solar power (CSP)-biomass hybrid power plants | Stochastic techno-economic assessment of CSP-biomass hybrid plants. Design variables, equations, and valuation parameters provided. 33% probability of profitability, high biomass share increases profitability, add-in tariff needed for grid parity. | Matlab | [14] |
| Hybrid wind/solar/biomass renewable energy system with biomass power trading | Hybrid system feeds 526 million kWh/year, wind contributes 57%, biomass supplies 25% of electricity. Unmet load rate reduced to 2.92%. Operators' earnings improved compared to actual operations | Homer | [15] |

Table 1. Literature review on hybrid systems with solar / biomass and/or desalination (continue).

| Investigated System | Findings | Software used | Ref |
|---|--|-----------------------------------|------|
| Solar and biomass-based cogeneration technologies | This is a chapter that has an overview of solar and biomass-based cogeneration technologies. Discussion on efficiencies and applications in combined heat and power systems. | - | [16] |
| Regional energy supply combined heat and power (RES-CHP) system integrating biomass and solar energy | Development of a regional energy supply system integrating biomass and solar energy. Energy, exergy, economy, and emissions analysis conducted. Energy efficiency of 42.57%, exergy efficiency of 39.52%, CO ₂ emissions of 4.146 kt/year (32.3% reduction). | Aspen Plus | [17] |
| Hybrid solar-biomass system for space heating and hot water supply | Optimal configuration with evacuated tube collectors: solar fraction of 57%, payback period of 4.9 years, LCOH of \$0.0642/kWh, payback period 4.9 years, annual CO ₂ avoidance of 656 tons. | TRNSYS | [18] |
| Multi-generation hybrid biomass-solar system for providing heating, cooling, electricity, fresh-water, and hydrogen | Reduction in biomass consumption and CO ₂ emissions. Sensitivity analysis indicates improvement in exergy efficiency and cost rate with increased solar radiation and biomass flow rate. | Matlab | [19] |
| Hybrid system based on wind, hydro, solar, and biomass sources for decarbonizing the energy sector | Wind and solar complement each other, hydro shows important variability. In 2018, Romania's energy mix relied significantly on hydropower (29%), with wind and solar varying seasonally but contributing consistently to meeting EU renewable energy goals (22% share), reducing CO ₂ emissions by 42%. | Homer | [20] |
| Solar-biomass on-grid hybrid system for Hattar Industrial Zone Phase (VII), Pakistan | Optimal configuration: 70,000 kW solar PV, 7000 kW biogas generator connected to the grid. Lowest COE of \$0.092/kWh. Payback period: 4.6 years. Reduction of 75% in carbon dioxide (CO ₂), 75% in sulfur oxide (SO _x), and 75% in nitrogen oxide (NO _x) emissions. | RET Screen | [21] |
| Standalone solar-wind-biomass-fuel cell energy system for rural community in Nigeria | LF-SSA algorithm optimization achieved lowest LCOE of \$0.933162/kWh and substantial cost savings compared to other algorithms and HOMER software. EMS facilitated environmentally friendly and cost-effective energy system. | Homer | [22] |
| Hybrid solar-biomass system for multi-family residential building | Advanced control reduces winter operation costs by 35%, applied in a residential building in Madrid. No significant reduction in summer costs. | Matlab | [23] |
| Biomass-solar hybrid gasification system for sustainable fuel production | Total energy conversion efficiency of 73.06%, carbon efficiency of 66.81%. Integration of solid-oxide electrolysis cells reduce electricity consumption during electrolysis by 19.30%. | Aspen Plus | [24] |
| Hybrid solar- and biomass-based energy system for electricity, freshwater, and hydrogen production | Proposal of an integrated system for renewable energy penetration, peak load flattening, and greenhouse gas reduction. Thermodynamic, exergo-economic, and environmental assessment conducted. | EES (Engineering Equation Solver) | [25] |

Table 1. Literature review on hybrid systems with solar / biomass and/or desalination (continue).

| Investigated System | Findings | Software used | Ref |
|---|---|---------------|------|
| Hybrid solar-biomass polygeneration system for power, heating, drying, oxygen, and ammonia production | Net power generation of 163 MW, heating of 150 MW, drying of 100 MW, oxygen production of 21.7 kmol/hr, and ammonia production of 23.24 kg/hr. Exergy efficiency: 70.68%, LCC: \$ 1.175×10 ⁹ , CO ₂ emissions: 381.3 kg/MWh. Optimized exergy efficiency: 51.02%, LCC: 1.16×10 ⁹ \$, CO ₂ emissions: 359.73 kg/MWh. | Matlab | [26] |
| Residential building energy supply systems combining torrefied biomass gasification and solar energy | Proposal of a hybrid energy system driven by torrefied biomass gasification and solar energy. Economic analysis shows positive NPV and energy-saving benefits. Annual income of \$72,735 with 2.89 years investment recovery; reduces CO ₂ emissions by 550.59 tons. | RET Screen | [27] |

References

- [1] D. R. Santos, E. C. M. Vieira, J. T. Rocha, Q. H. S. Eugenio, and C. M. Campos, "Challenges and solutions for renewable energy storage," *Brazil. J. Prod. Eng.*, vol. 9, no. 4, pp. 76–88, Oct. 2023, doi: 10.47456/bjpe.v9i4.42343.
- [2] M. Farghali et al., "Social, environmental, and economic consequences of integrating renewable energies in the electricity sector: a review," *Environ. Chem. Lett.*, vol. 21, pp. 1381–1418, Mar. 2023, doi: 10.1007/s10311-023-01587-1.
- [3] A. Panda et al., "Recent advances in the integration of renewable energy sources and storage facilities with hybrid power systems," *Clean Eng. Tech.*, vol. 12, Feb. 2023, Art. no. 100598, doi: 10.1016/j.clet.2023.100598.
- [4] A. Dağdeviren et al., "Effect of Al₂O₃-SiO₂/water hybrid nanofluid filled in a square enclosure on the natural convective heat transfer characteristics: A numerical study," *J. Nanofluids*, vol. 11, pp. 772–781, Aug. 2022, doi: 10.1166/jon.2022.1881.
- [5] E. Gürsoy et al., "Energy analysis of magnetite nanofluid flowing in newly designed sudden expansion tube retrofitted with dimpled fin," *Int. J. Heat Mass Transfer*, vol. 199, Dec. 2022, Art. no. 123446, doi: 10.1016/j.ijheatmasstransfer.2022.123446.
- [6] E. Gürsoy et al., "Experimental and numerical study on ferrohydrodynamic and magneto-convection of Fe₃O₄/water ferrofluid in a sudden expansion tube with dimpled fins," *J. Taiwan Inst. Chem. Eng.*, vol. 164, Nov. 2024, Art. no. 105676, doi: 10.1016/j.jtice.2024.105676.
- [7] E. Gürsoy et al., "Investigation of magneto-convection characteristics in a sudden expanding channel with convex surface geometry under thermally developing flow conditions," *Int. J. Numer. Meth. Heat Fluid Flow*, vol. 34, no. 5, pp. 1969–1994, May 2024, doi: 10.1108/HFF-11-2023-0703.
- [8] A. R. Jensen et al., "Demonstration of a concentrated solar power and biomass plant for combined heat and power," *Energy Convers. Manag.*, vol. 271, Nov. 2022, Art. no. 116207, doi: 10.1016/j.enconman.2022.116207.
- [9] H. Kaur, S. Gupta, and A. Dhingra, "Analysis of hybrid solar biomass power plant for generation of electric power," *Mater. Today: Proc.*, vol. 48, no. 5, pp. 1134–1140, 2022, doi: 10.1016/j.matpr.2021.08.080.

- [10] R. J. Macías et al., "Evaluation of the performance of a solar photovoltaic-biomass gasifier system as electricity supplier," *Energy*, vol. 260, Dec. 2022, Art. no. 125046, doi: 10.1016/j.energy.2022.125046.
- [11] E. Aykut, B. Dursun, and S. Görgülü, "Comprehensive environmental and techno-economic feasibility assessment of biomass-solar on-grid hybrid power generation system for Burdur Mehmet Akif Ersoy University Istiklal Campus," *Heliyon*, vol. 9, no. 11, Nov. 2023, doi: 10.1016/j.heliyon.2023.e22264.
- [12] A. A. Díaz Pérez, E. K. Burin, and E. Bazzo, "Part load operation analysis of a biomass steam generator integrated with a Linear Fresnel solar field," *Energy*, vol. 282, Nov. 2023, Art. no. 128590, doi: 10.1016/j.energy.2023.128590.
- [13] R. Gutiérrez-Alvarez, K. Guerra, and P. Haro, "Market profitability of CSP-biomass hybrid power plants: towards a firm supply of renewable energy," *App. Energy*, vol. 335, Apr. 2023, Art. no. 120754, doi: 10.1016/j.apenergy.2023.120754.
- [14] R. Gutiérrez-Alvarez, K. Guerra, and P. Haro, "Profitability of Concentrated Solar-Biomass hybrid power plants: Dataset of the stochastic techno-economic assessment," *Data in Brief*, vol. 48, Jun. 2023, Art. no. 109096, doi: 10.1016/j.dib.2023.109096.
- [15] Y. Huang, Q. Wang, and J. Xu, "A stackelberg-based biomass power trading game framework in hybrid-wind/solar/biomass system: From technological, economic, environmental and social perspectives," *J. Clean. Prod.*, vol. 403, Jun. 2023, Art. no. 136806, doi: 10.1016/j.jclepro.2023.136806.
- [16] A. N. Srivastava, A. Kaviti, S. Chakma, and V. S. Sikarwar, "Solar and Biomass-Based Cogeneration Technologies," *Encycl. Renew. En. Sustain. Environ.*, vol. 4, pp. 263-272, 2024, doi: 10.1016/B978-0-323-93940-9.00036-0.
- [17] Z. Li, X. Zhu, X. Huang, Y. Tian, and B. Huang, "Sustainability design and analysis of a regional energy supply CHP system by integrating biomass and solar energy," *Sustain. Prod. Consum.*, vol. 41, pp. 228-241, Oct. 2023, doi: 10.1016/j.spc.2023.08.011.
- [18] M. Krarouch, A. Allouhi, H. Hamdi, and A. Outzourhit, "Energy, exergy, environment and techno-economic analysis of hybrid solar-biomass systems for space heating and hot water supply: Case study of a Hammam building," *Renew. Energy*, vol. 222, Feb. 2024, Art. no. 119941, doi: 10.1016/j.renene.2024.119941.
- [19] M. Korpeh, P. Asadbagi, A. Lotfollahi, A. Ghaemi, and A. A-Moghaddam, "4E analysis and optimization of a novel hybrid biomass-solar system: Focusing on peak load management and environmental emissions," *Process Saf. Environ. Prot.*, vol. 181, pp. 452-468, Jan. 2024, doi: 10.1016/j.psep.2023.11.035.
- [20] P. Spuru, "Assessment of renewable energy generated by a hybrid system based on wind, hydro, solar, and biomass sources for decarbonizing the energy sector and achieving a sustainable energy transition," *Energy Reports*, vol. 9, no. 8, pp. 167-174, Sep. 2023, doi: 10.1016/j.egy.2023.04.316.
- [21] A. Zahid, M.K. Shahzad, S.R. Jamil, and N. Iqbal, "Futuristic feasibility analysis and modelling of a solar-biomass on-grid hybrid system for Hattar Industrial Estate Phase (VII), Pakistan," *Cleaner Energy Systems*, vol. 4, Apr. 2023, Art. no. 100053, doi: 10.1016/j.cles.2023.100053.
- [22] B. Modu, Md. P. Abdullah, A. L. Bukar, M. F. Hamza, and M. S. Adewolu, "Operational strategy and capacity optimization of standalone solar-wind-biomass-fuel cell energy system using hybrid LF-SSA algorithms," *Intern. J. Hydr. Energy*, vol. 50(B), pp. 92-106, Jan. 2024, doi: 10.1016/j.ijhydene.2023.07.215.
- [23] G. Zsembinski, C. Fernández, E. Borri, and L. F. Cabeza, "Application of deep learning techniques to minimize the cost of operation of a hybrid solar-biomass system in a multi-family building," *En. Conv. Manag.*, vol. 288, Jul. 2023, Art. no. 117152, doi: 10.1016/j.enconman.2023.117152.
- [24] Y. Xin, X. Xing, X. Li, and H. Hong, "A biomass-solar hybrid gasification system by solar pyrolysis and PV-Solid oxide electrolysis cell for sustainable fuel production," *App. Energy*, vol. 356, Feb. 2024, Art. no. 22419, doi: 10.1016/j.apenergy.2023.122419.
- [25] T. Hai, F. M. Alhomayani, P. Ghodrallah, B. S. Chauhan, H. Rajab, S. F. Almojil, A. I. Almohana, and U. Mirzat, "Proposal and ANN-assisted optimization of a hybrid solar- and biomass-based energy system for electricity, freshwater, and hydrogen production" *Int. J. Hydr. Energy*, early access, Feb. 2024, doi: 10.1016/j.ijhydene.2024.02.126.
- [26] A. Nouri, A. Chitsaz, M. Khalilian, and A. Hasanzadeh, "Analysis and optimization of a sustainable hybrid solar-biomass polygeneration system for production of power, heating, drying, oxygen and ammonia," *App. Therm. Eng.*, vol. 246, Jun. 2024, Art. no. 122867, doi: 10.1016/j.applthermaleng.2024.122867.
- [27] Y. Liu, D. Bi, M. Yin, K. Zhang, H. Liu, and S. Liu, "Modeling and exergy-economy analysis of residential building energy supply systems combining torrefied biomass gasification and solar energy," *Therm. Sci. Eng. Prog.*, vol. 50, May 2024, Art. no. 102584, doi: 10.1016/j.tsep.2024.102584.
- [28] H. Xu, S. Jiang, M. X. Xie, T. Jia, and Y. J. Dai "Technical improvements and perspectives on humidification-dehumidification desalination - a review," *Desalin.*, vol. 541, Nov. 2022, Art. no. 116029, doi: 10.1016/j.desal.2022.116029.
- [29] C. Fritzmann, J. Löwenberg, T. Wintgens, T. Melin, "State-of-the-art of reverse osmosis desalination," *Desalin.*, vol. 216, no. 1-3, pp. 1-76, Oct. 2007. doi: 10.1016/j.desal.2006.12.009.
- [30] A. P. Nicolás, A. Molina-García, J. T. García-Bermejo, and F. Vera-García, "Desalination, minimal and zero liquid discharge powered by renewable energy sources: Current status and future perspectives," *Renew. Sustain. En. Reviews*, vol. 187, Nov. 2023, Art. no. 113733, doi: 10.1016/j.rser.2023.113733.
- [31] A. Yadav, P. K. Labhasetwar, and V. K. Shahi, "Membrane distillation using low-grade energy for desalination: A review," *J. Env. Chem. Eng.*, vol. 9, no. 5, Oct. 2021, Art. no. 105818, doi: 10.1016/j.jece.2021.105818.
- [32] M. Sedighi, M. M. B. Usefi, A. F. Ismail, and M. Ghasemi, "Environmental sustainability and ions removal through electro dialysis desalination: Operating conditions and process

- parameters,” *Desalination*, vol. 549, Mar. 2023, Art. no. 116319, doi: 10.1016/j.desal.2022.116319.
- [33] M. M. Rashidi, I. Mahariq, N. Murshid, S. Wongwises, O. Mahian, M. A. Nazari, “Applying wind energy as a clean source for reverse osmosis desalination: A comprehensive review,” *Alex. Eng. J.*, vol. 61, no. 12, pp. 12977-12989, Dec. 2022, doi: 10.1016/j.aej.2022.06.056.
- [34] K. Wang, and J. W. Tester, “Sustainable management of unavoidable biomass wastes,” *Green. En. Res.*, vol. 1, no. 1, Mar. 2023, Art. no. 100005, doi: 10.1016/j.gerr.2023.100005.
- [35] F. A. M. Lino, K. A. R. Ismail, and J. A. Castañeda-Ayarza, “Municipal solid waste treatment in Brazil: A comprehensive review,” *Energy Nexus*, vol. 11, Sep. 2023, Art. no. 100232, doi: 10.1016/j.nexus.2023.100232.
- [36] S. Vyas, P. Prajapati, A. V. Shah, V. K. Srivastava, and S. Varjani, “Opportunities and knowledge gaps in biochemical interventions for mining of resources from solid waste: A special focus on anaerobic digestion,” *Fuel*, vol. 311, Mar. 2022, Art. no. 122625, doi: 10.1016/J.FUEL.2021.122625.
- [37] A. Khosravi, S. Santasalo-Aarnio, and S. Syri, “Optimal technology for a hybrid biomass/solar system for electricity generation and desalination in Brazil,” *Energy*, vol. 234, Nov. 2021, Art. no. 121309, doi: 10.1016/j.energy.2021.121309.
- [38] E. B. Pereira et al., *Brazilian Atlas of Solar Energy*, 2nd ed., São José dos Campos, Brazil: INPE, 2017, p. 80, doi: 10.34024/978851700089.
- [39] Labren, “Brasil-SR Model,” Accessed: Aug. 5, 2024. [Online]. Available: <https://labren.ccst.inpe.br/brasil-sr.html>
- [40] ABREMA, “Panorama of Solid Waste in Brazil,” Accessed: Oct. 5, 2024. [Online]. Available: <https://abrelpe.org.br/panorama/>
- [41] A. Calbry-Muzyka, H. Madi, F. Rüsç-Pfund, M. Gandiglio, and S. Biollaz, “Biogas composition from agricultural sources and organic fraction of municipal solid waste,” *Renew. Energy*, vol. 181, pp. 1000-1007, Jan. 2022, doi: 10.1016/j.renene.2021.09.100.
- [42] A. Kumar, and S. R. Samadder, “Development of lower heating value prediction models and estimation of energy recovery potential of municipal solid waste and RDF incineration,” *Energy*, vol. 274, Jul. 2023, Art. no. 127273, doi: 10.1016/j.energy.2023.127273.
- [43] M. Ioelovich, “Energy Potential of Natural, Synthetic Polymers and Waste Materials - A Review,” *Academ. J. Polym. Sci.*, vol. 1, no. 1, May 2018 doi: 10.19080/AJOP.2018.01.555553.
- [44] C. Bispo, C. Colombo, R. Braz, M. Medeiros, and F. Souza, “Selective collection in Natal/RN: scenario of recyclable materials cooperatives,” *Metrop. J. Sustain.*, vol. 7, no. 1, pp. 141-160, Jan./Apr. 2017, (in Portuguese).
- [45] G. O. Santos, and F. B. S. Mota, “Gravimetric composition of household solid waste in Fortaleza - CE disposed at the Caucaia/CE landfill,” *Technol. J.*, vol. 31, no. 1, pp. 39-50, (in Portuguese), Jun 2010.
- [46] G. P. Narayan, K. H. Mistry, M. H. Sharqawy, S. M. Zubair, and J. H. Lienhard, “Energy effectiveness of simultaneous heat and mass exchange devices,” *Front. Heat and Mass Trans.*, vol. 1, no. 2, pp. 1-13, Jul. 2010, doi: 10.5098/hmt.v1.2.3001.
- [47] M. H. Sharqawy, J. H. Lienhard, and S. M. Zubair, “Thermophysical properties of seawater: A review of existing correlations and data,” *Desalin. and Water Treat.*, vol. 16, no. 1-3, pp. 354-380, Aug. 2012, doi:10.5004/dwt.2010.1079.
- [48] L. Pagnini, S. Bracco, F. Delfino, and M. Simón-Martin, “Levelized cost of electricity in renewable energy communities: Uncertainty propagation analysis,” *Appl. Energy*, vol. 366, Jul. 2024, Art. no. 123278, doi: 10.1016/j.apenergy.2024.123278.
- [49] M. J. B. Kabeyi, and O. A. Olanrewaju, “The levelized cost of energy and modifications for use in electricity generation planning,” *Energy Rep.*, vol. 9, Supp 9, pp. 495-534, Sep. 2023, doi: 10.1016/j.egy.2023.06.036.
- [50] A. H. Alami et al., “Concentrating solar power (CSP) technologies: Status and analysis,” *Int. J. Thermofluids*, vol. 18, May 2023, Art. no. 100340, doi: 10.1016/j.ijft.2023.100340.
- [51] M. D. Rey, R. Font, and I. Aracil, “Biogas from MSW landfill: Composition and determination of chlorine content with the AOX (adsorbable organically bound halogens) technique,” *Energy*, vol. 63, pp. 161-167, Dec. 2013, doi: 10.1016/j.energy.2013.09.017.
- [52] N. Dadario et al., “Waste-to-energy recovery from municipal solid waste: Global scenario and prospects of mass burning technology in Brazil,” *Sustainability*, vol. 15, no. 6, Mar. 2023, Art. no. 5397, doi: 10.3390/su15065397.
- [53] M. S. Riaz, K. J. Barb, and A. Engeda, “A Novel Technique for Steam Turbine Exhaust Pressure Limitation Using Dynamic Pressure Sensors,” *Proc. of the Inst. of Mech. Eng., Part C: J. Mech. Eng. Sci.*, vol. 219, no. 9, pp. 925-932, Sep. 2005, doi:10.1243/095440605X31805.
- [54] V. Mrzljak, T. Senčić, and B. Žarković, “Turbogenerator Steam Turbine Variation in Developed Power: Analysis of Exergy Efficiency and Exergy Destruction Change,” *Modell. Simul. Eng.*, vol. 2018, no. 1, Jul. 2018, Art. no. 2945325, doi: 10.1155/2018/2945325.
- [55] IPCC, Chapter 2: Stationary Combustion, in *2006 IPCC Guidelines for National Greenhouse Gas Inventories*, vol. 2: Energy. Accessed: Oct. 1, 2024. [Online]. Available: <https://www.ipcc-nggip.iges.or.jp>
- [56] Q. Liu et al., “Thermodynamics investigation of a solar power system integrated oil and molten salt as heat transfer fluids,” *App. Therm. Eng.*, vol. 93, pp. 967-977, Jan. 2016, doi: 10.1016/j.applthermaleng.2015.10.071.
- [57] T. P. van der Stelt, E. Casati, N. Chan, and P. Colonna, “Technical equation of state models for heat transfer fluids made of biphenyl and diphenyl ether and their mixtures,” *Fluid Phase Equilibria*, vol. 393, pp. 64-77, May 2015, doi: 10.1016/j.fluid.2015.02.025.
- [58] V-E. Cenușă et al., “Energetic and exergetic analysis of Rankine cycles for solar power plants with parabolic trough and thermal storage,” *Renew. Energy Environ. Sustain.*, vol. 1, May 2016, doi: 10.1051/rees/2016010.
- [59] Eastman, “Therminol VP-1 Technical Bulletin 7239115B,” Accessed: June 3, 2024. [Online]. Available: https://www.therminol.com/sites/therminol/files/documents/TF09A_Therminol_VP1.pdf

Research Article

General Thermodynamically Unification of the First and Second Laws of Thermodynamics

¹*S. Shahsavari , ²S. M. A. Boutorabi 

^{1,2}School of Metallurgy and Material Engineering, Iran University of Science and Technology, Tehran, Iran
E-mail: ¹*s.shahsavari@alumni.iut.ac.ir

Received 6 November 2024, Revised 1 December 2024, Accepted 17 December 2024

Abstract

The unification of the first and second laws of thermodynamics into a single equation has long been a key goal in thermodynamic research. However, significant mathematical and physical challenges have hindered its achievement. In this paper, we go a step further and seek a general as well as completely thermodynamically unification of these laws. The generality, energy fundamental-based and statistical perspective of the Boltzmann entropy equation can provide a valuable solution to unify the first and second laws of classical thermodynamics. Here, “entropy generation function” is considered as a function that takes a measure of lost available work of any thermodynamic energy conversion system, and also “integrator function” is considered as a function that is applied for the mathematical unification. Also, the quasi-statistical approach of entropy is considered as an approach that studies macroscopic energy components instead of studying the energy of individual particles. So, in this paper, by applying the entropy generation function g , as a novel integrator function, we consider the second law as an equality. In the following, using a new quasi-statistical approach to the entropy with the same base as Boltzmann entropy equation, function g is derived. Finally, we extract two innovative general thermodynamically equations resulting from unification of the first and second laws of classical thermodynamics as well as a novel general thermodynamically unified second law equation is established. Contrary to what is common in classical thermodynamics, the established unified equations are sufficient for the thermodynamically analysis of physical processes, and there is no need to add any additional condition relation or non-thermodynamic quantity. In fact, we are looking for a general thermodynamically unification of the first and second laws, which is one of the highlights of this paper. Finally, a general mathematical-physical validation is presented and in the general case, it is shown that there are no contradictions in the established unified equations.

Keywords: *Unified thermodynamically equation; general unified thermodynamics; entropy; statistical approach; integrator function.*

1. Introduction

First, it is necessary to state that what we mean by general thermodynamically unification of the first and second laws of thermodynamics is that the relevant integration is studied without any additional assumptions rather than well-known expressions of these laws, or the existence of non-thermodynamic quantities or even thermodynamic quantities that are not directly present on the well-known expressions of the first and second laws. This is one of the main highlights that we are going to address in this paper.

The unification of scientific laws has special importance among scientists [1-8]. The unification of the first and second laws of thermodynamics can directly apply the second law into the thermodynamically analysis. However, due to the mathematical and physical challenges involved, the subject is known as an important challenge for scientists yet. Usually, the first law of thermodynamics is known as internal energy definition and the second law is known as definition of entropy [9-13]. Although by establishment of more advanced scientific theories, such as quantum mechanics theory and statistical mechanics theory, the first law is still used in its classical form to a significant extent, but due to

the expansion of different definitions and criteria for entropy, the second law is available in different formulations. So, we may be at the peak of confusion related to the second law, or in other words, classical thermodynamics [14-18]. In the perspective of classical thermodynamics, the second law is provided by an inequality, and is not directly used in the analysis of problems, and it is proposed as a condition relation for the results of the first law. It is important to note that the Gibbs function, as a function that has energy and entropy in its definition, can be considered as one of the first attempts to integrate energy and entropy in a single quantity. While it does not provide specific information on the integration of these laws into a single law, and does not address this issue. In fact, Gibb’s function has the necessary condition needed by an integrator function in the subject.

Although the unification of the first and second laws of thermodynamics can provide further achievements of the basic aspects of these two fundamental laws, success in this case depends on establishing the relationship between entropy and internal energy. While the classical perspective does not provide such as this connection, it is necessary to use other scientific theories and perspectives. It is thought

that the perspective of statistical mechanics as well as Boltzmann entropy equation gives the most general and accepted approach of entropy at present [19-20]. Considering that the basis of Boltzmann entropy equation is related to the energy of substructures by Einstein, Maxwell or Fermi-Dirac equations, applying Boltzmann point of view can provide the fundamental conditions for this unification. However, considering that the direct relationship between classical thermodynamics and Boltzmann entropy equation cannot be analyzed, it is necessary to use other approaches with a common basis as the Boltzmann entropy equation [21-29].

The quasi-statistical approach to entropy has a common basis with Boltzmann entropy equation, and is also written based on the activated components of energy in the physical processes [29, 34]. So, in terms of the physical concepts and mathematical tools required, the quasi-statistical approach to entropy meets the requirements set forth. More details about the conditions, concepts, and mathematical tools needed to integrate scientific laws across different perspectives can be found in the references [30-31].

In this paper, we are working towards a general thermodynamically unification of the first and second laws of thermodynamics. The goal of general thermodynamically unification is to study the unification of these laws without any additional assumptions or the addition of quantities that are not directly present in the first and second laws of thermodynamics. For this purpose, by considering the entropy generation function as a novel integrator function, the second law of thermodynamics is written as an equality. In the following, using the quasi-statistical perspective of entropy, the novel integrator function is calculated, and the desired general thermodynamically unified equations are extracted. Also, using novel established unified equations, the general thermodynamically unified second law is also established. The general thermodynamically unified equations will be sufficient independently for the thermodynamically analysis of physical processes, and there is no need to check any other additional conditions. In fact, as expected, the general established unified equations have the effects of the first and second laws simultaneously.

2. Theoretical Background

Combining the laws of thermodynamics and presenting them with a single equation is not an attempt that has "not been done so far". The question of whether there is a unifying framework for related theories in the same discipline is a common question for the authors of the references [1-31] have been cited in the introduction. However, there are several sections where individual theorem sets are exceptional cases of a single unifying result or where a single perspective on how to proceed as a field of mathematics develops can be applied fruitfully on the many branches of the subject.

The macroscopic scale values of energy are independent of the macroscopic scale values of entropy [32]. However, the Gibbs function G is a beautiful relation combining energy and entropy in a single term as follows:

$$G = H - TS \quad (1)$$

Where H is enthalpy, T is temperature and S is entropy. In fact, the Gibbs equation (the Gibbs function) provides an early cornerstone (as an integrator function) for combining the first and second laws of thermodynamics. However, for

this case, it uses a new function that does not exist directly in the first or second law of thermodynamics. So, a new function will be added. Also, the basis of the definition of the Gibbs function are not related to the unification of the laws of thermodynamics and do not make any attempt in this subject. In fact, the Gibbs function only gives a combined function of energy and entropy. So, it can be considered as an integrator function to the draft subject.

As an example, in the context of trying to unify the first and second laws of thermodynamics, reference [33] develops a combined of the first and second laws of thermodynamics using the principles of classical statistical mechanics. Figure 1 takes the physical concepts as well as mathematical tools used to derivation of the combined equation of the first and second laws of thermodynamics in reference [33]:

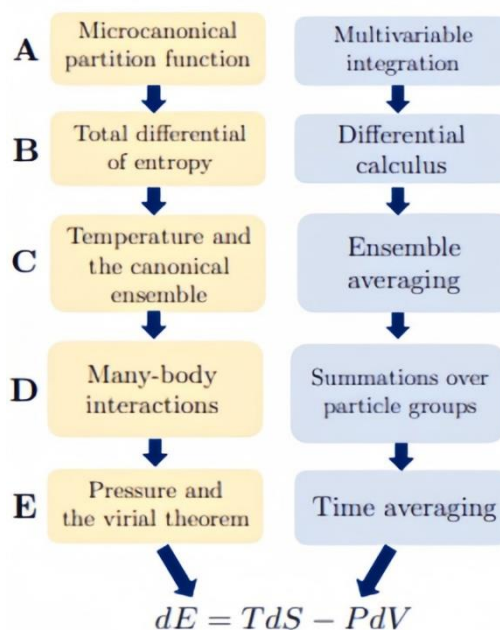


Figure 1. The physical concepts (left) and mathematical tools (right) used to derivation of the combined equation of the first and second laws of thermodynamics [33].

So, classical thermodynamics as well as statistical mechanics are used in reference [33] to derivation a combined equation of the first and second laws of thermodynamics. More details can be reached in the old or new versions of reference [33]. It can be deduced that using the principles and concepts of statistical mechanics alongside thermodynamics provides the needed conditions for unification the first and second laws of thermodynamics. In fact, thermodynamics alone cannot be unified and it is necessary to use appropriate physical concepts and mathematical tools.

3. Methodology

Given what we know on the nature of entropy produced in physical processes, in this paper we intend to use the entropy generation as an integrator function. So, considering entropy generation function g , as a novel integrator function, Eqs. (2)-(3) gives the first and second laws of thermodynamics:

$$\dot{U} = \dot{Q} - \dot{W} \quad (2)$$

$$\dot{S} = \frac{\dot{Q}}{T} + g \quad (3)$$

Where U is internal energy, \dot{Q} is rate of the heat exchange, \dot{W} is rate of the work done, S is entropy, and T is temperature. So, two equations can be derived as follows:

$$\dot{U} = T\dot{S} - \dot{W} + h \quad (4)$$

$$T\dot{S} = \dot{Q} - h \quad (5)$$

That $h \equiv -Tg$. So, it is necessary to derive the novel integrator function h first. In fact, considering the innovative completely thermodynamically approach, the main challenge on unification the first and second laws is the deriving of this novel integrator function. Here it is necessary to use the existing perspectives on entropy. Clearly, classical thermodynamics cannot provide such conditions to derive the function h , neither from the fundamentals nor from the mathematical point of view. In fact, the general views on entropy, either mathematically or physically, do not provide the necessary conditions for the general unification of the first and second laws of classical thermodynamics. From the perspective of the physical foundations, the Boltzmann entropy equation provides the necessary physical conditions for the desired unification. Although from a mathematical point of view, it is not applicable to derive the function h . Therefore, it is necessary to use other approaches related to entropy with a common basis as Boltzmann entropy equation [16, 21, 23-29]. This approach will be discussed in the following.

3.1 Quasi-Statistical Approach to the Entropy

Figure 2 takes the energy component's approach has been established by Energy Structure Theory [29, 34]:

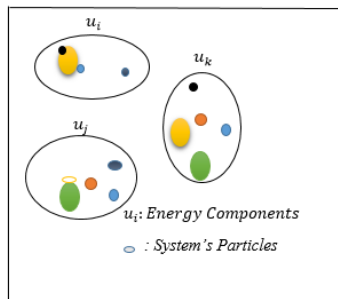


Figure 2. Energy Component's Approach [29].

Where u_i are known as energy components of the system. Each particle may participate in the several of energy components. Using energy component's approach and energy structure equation as well as a novel energy conservation principle, Energy Structure Theory establishes a quasi-statistical equation to entropy as follows:

$$\delta S = K_{MS} \delta[\ln(W_U)] \quad (6)$$

That K_{MS} is known as a universal constant. As discussed in reference [29, 34], the quasi-statistical perspective to entropy has common foundations to the Boltzmann entropy equation. And also:

$$W_U = \prod_{j=1}^m w_{u_j} \quad (7)$$

That:

$$w_{u_j} = \dot{U}_j \quad (8)$$

Considering path $1 \rightarrow 2$ as a quasi-static path, as well as path $1 \rightarrow 2'$ as a general path, Figure 3 takes the variation of \dot{U}_j as difference between two different paths as follows [29, 34]:

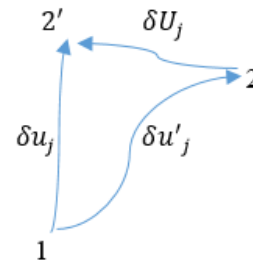


Figure 3. Difference between two different paths [34].

In fact, figure 3 illustrates the difference in entropy, S_{gen} , between a quasi-static path ($P_{quasi-1} \rightarrow 2$) and a general path ($P_{gen-1} \rightarrow 2'$). This comparison is based on the energy structure equation and the entropy generation function, which are grounded in the Boltzmann entropy framework. Finally, given the necessary physical and mathematical conditions discussed, the quasi-statistical approach to entropy provides a suitable solution for the general thermodynamically unification of the first and second laws. In fact, the quasi-statistical approach to entropy provides the necessary physical and mathematical conditions for deriving the considered integrator function (the generated entropy function). In the following, we will discuss the general thermodynamically calculation of this function.

3.2 Mathematical Development: Two Innovative General Thermodynamically Unified Equations

So, using quasi-statistical approach to the entropy with the same base as Boltzmann entropy equation has been established by Energy Structure Theory:

$$\delta S = K_{MS} \delta[\ln(W_U)] \quad (9)$$

$$\dot{S} = K_{MS} \frac{\dot{W}_U}{W_U} = K_{MS} \frac{\dot{U}}{U} \quad (10)$$

So:

$$\dot{S} = K_{MS} \left(\frac{\dot{T}\dot{S} + T\ddot{S} - \dot{W} - h}{T\dot{S} - \dot{W} + h} \right) \quad (11)$$

Therefore, Eq. (11) can be rewritten as follows:

$$\dot{h} - \frac{\dot{S}}{K_{MS}} h = -\dot{T}\dot{S} - T\ddot{S} + \dot{W} + \frac{T}{K_{MS}} \dot{S}^2 - \frac{\dot{S}\dot{W}}{K_{MS}} \quad (12)$$

Eq. (12), in its current expression, is a general thermodynamically equation. Finally, function h is extracted as follows:

$$h = \frac{1}{e^{\int \left(\frac{\dot{S}}{K_{MS}} \right) dt + C_1}} \int \left[\left(e^{\int \left(\frac{\dot{S}}{K_{MS}} \right) dt + C_1} \right) \cdot \left(-\dot{T}\dot{S} - T\ddot{S} + \dot{W} + \frac{T}{K_{MS}} \dot{S}^2 - \frac{\dot{S}\dot{W}}{K_{MS}} \right) dt + C_2 \right] \quad (13)$$

It is necessary to state here that the function h satisfies the necessary and sufficient energy structure conditions discussed in references [29, 34]. So, entropy generation function (considered novel integrator function) is extracted as follows:

$$g = -\frac{h}{T} = \frac{-1}{T e^{\int \left(\frac{\dot{s}}{K_{MS}}\right) dt + C_1}} \int \left[\left(e^{\int \left(\frac{\dot{s}}{K_{MS}}\right) dt + C_1} \right) \cdot \left(-\dot{T}\dot{S} - T\ddot{S} + \dot{W} + \frac{T}{K_{MS}}\dot{S}^2 - \frac{\dot{S}\dot{W}}{K_{MS}} \right) \right] dt + C_2 \quad (14)$$

Eq. (14) takes the entropy generation function (the considered integrator function). In fact, it gives the thermodynamically structure of the function g . Therefore, as can be deduced from Eq. (14), the entropy generation function, both physically and mathematically, is a suitable function for use as an integrator function in general thermodynamically unifying the first and second laws of thermodynamics.

So, two novel general thermodynamically unified equations are established as follows:

$$\dot{U} = T\dot{S} - \dot{W} + \frac{1}{e^{\int \left(\frac{\dot{s}}{K_{MS}}\right) dt + C_1}} \int \left[\left(e^{\int \left(\frac{\dot{s}}{K_{MS}}\right) dt + C_1} \right) \cdot \left(-\dot{T}\dot{S} - T\ddot{S} + \dot{W} + \frac{T}{K_{MS}}\dot{S}^2 - \frac{\dot{S}\dot{W}}{K_{MS}} \right) \right] dt + C_2 \quad (15)$$

And also:

$$T\dot{S} = \dot{Q} - \frac{1}{e^{\int \left(\frac{\dot{s}}{K_{MS}}\right) dt + C_1}} \int \left[\left(e^{\int \left(\frac{\dot{s}}{K_{MS}}\right) dt + C_1} \right) \cdot \left(-\dot{T}\dot{S} - T\ddot{S} + \dot{W} + \frac{T}{K_{MS}}\dot{S}^2 - \frac{\dot{S}\dot{W}}{K_{MS}} \right) \right] dt + C_2 \quad (16)$$

Eq. (15) includes the internal energy, while in Eq. (16), internal energy is not directly observed. This issue does not make a difference in the foundations of these equations. In fact, the foundations of the general thermodynamically novel established unified Eqs. (15)-(16) are based on the statistical approach to entropy and the entropy generation function g . Mathematically, the unified Eq. (16) can be described as including fewer thermodynamically quantities, which may can achieve more unification.

4. Novel General Thermodynamically Unified Second Law

The general thermodynamically unified second law is a rewrite of Clausius formulation in the equality formulation considering the first law of thermodynamics as well as Boltzmann approach to the entropy to apply irreversibility effects on the Clausius formulation of the second law. So, Eq. (5) takes an initial unified second law equation considering entropy generation function as the needed integrator function. Therefore, by replacing entropy generation function g , the novel general thermodynamically unified second law equation is established as follows:

$$\dot{S} = \frac{\dot{Q}}{T} - \frac{1}{T} \left[\frac{1}{e^{\int \left(\frac{\dot{s}}{K_{MS}}\right) dt + C_1}} \int \left[\left(e^{\int \left(\frac{\dot{s}}{K_{MS}}\right) dt + C_1} \right) \cdot \left(-\dot{T}\dot{S} - T\ddot{S} + \dot{W} + \frac{T}{K_{MS}}\dot{S}^2 - \frac{\dot{S}\dot{W}}{K_{MS}} \right) \right] dt + C_2 \right] \quad (17)$$

Eq. (14) gives a new very important perspective on the second law. In the established general thermodynamically unified equation of the second law, in addition to the second derivative of entropy, terms related to the way of doing work are also seen, which are related to the effects of irreversibility. In the following, the validity of Eqs. (10)-(14) is discussed from the perspective of structure and required conditions.

5. Results and Discussion

The unified Eqs. (15)-(17) are both mathematically and physically equivalent. In this part, a physical-mathematical discussion is presented on the general verification of the established unified equations (step by step). The unified Eqs. (15)-(17) were extracted from the unification of first and second laws of thermodynamics. The entropy generation function g was considered as the integrator function, and was then calculated mathematically. In the following, using entropy generation function g as well as well-known formulations of the first and second laws of thermodynamics, the unified equations were established.

At first, it is necessary to be noted that the unification carried out in this paper, is in the general thermodynamic case and no additional assumptions are made. In fact, the calculations are based directly on the sufficiently well-known expressions of the first and second laws of thermodynamics as well as using sufficiently validated and accepted mathematical tools. So, from a mathematical point of view, the discussion of the calculations of extracting the integrator function g , Eq. (13) is the main topic to validation discussion. Differential Eq. (12) is written in such a way that it falls into the category of first-order linear differential equations [35]. Therefore, if it satisfies the conditions of uniqueness of the response over its entire required domain as an integrator function for unification the first and second laws of thermodynamics, the mathematical validation is complete. In order to study Eq. (12), it is initially considered that:

$$p \equiv -\frac{\dot{s}}{K_{MS}} \quad (18)$$

$$q \equiv -\dot{T}\dot{S} - T\ddot{S} + \dot{W} + \frac{T}{K_{MS}}\dot{S}^2 - \frac{\dot{S}\dot{W}}{K_{MS}} \quad (19)$$

As can be seen, the functions p and q are fully defined in the domain of thermodynamic values and also have no singular points. Therefore, function h calculated in Eq. (13) is fully defined in the domain of thermodynamic values of the first and second laws of thermodynamics, is valid, and is also acceptable as an integrator function. So, all the calculation steps performed to extract the unified equations can also be concluded and performed reversibly. This means that Eqs. (15)-(17) completely encompass the first and second laws of thermodynamics. Also, just as these equations can be derived from the combination of the first and second laws of thermodynamics, the reverse calculations can also be completed and the first and second laws can be derived. Therefore, all necessary and sufficient conditions are satisfied in the established equations.

Although the discussion presented is complete, it can be stated that from another perspective, it is clearly deduced that Eqs. (15)-(17) satisfy the necessary and sufficient energy structure and the compatibility conditions established by energy structure theory. The energy structure equation as

well as the corresponding compatibility conditions are fully developed in references [26, 29, 34].

6. Conclusions

The attempt to unify scientific theories as a matter of great importance has a long history among scientists. The physical meaning of unification in scientific theories (or physical laws as well as principles) is to add the effects of different laws to each other, and extract the desired unified equation. Considering that in the unifications it is necessary to use an additional model, perspective or equation, therefore, it is seriously necessary to emphasize that the unifications in different ways do not necessarily lead to a similar equation. In fact, applying the effects of scientific laws on each other using different approaches can lead to different unified equations. In fact, part of the features, mathematics and applications of the unified equation goes back to the additional perspective used in the unification. Physical and mathematical challenges are the main challenges from the perspective of the possibility of unification scientific laws. From the physical point of view, it is necessary to establish the foundations required by the additional perspective used in unification, and from the mathematical point of view, it must be also possible to apply the additional perspective by mathematical operators.

The pursuit of unification in thermodynamics occupies a great special place. In other words, the first law of thermodynamics uses the quantity of internal energy to express the conservation of energy based on work done and heat exchanged in thermodynamic processes. Meanwhile, the second law of thermodynamics by defining the entropy quantity provides a necessary condition for the processes to be carried out. By the expansion of different definitions on the entropy, the expressions of the second law have also been expanded. It is in this situation that the unification of the first and second laws of thermodynamics becomes more important. The perspective of classical thermodynamics cannot get a specific idea in line with this unification. Also, the extended definitions on the entropy are generally not applicable either mathematically or physically for the purpose of unification. In the meantime, the statistical physics approach to entropy, which provides the Boltzmann entropy equation, provides the necessary physical foundations to unify the first and second laws of thermodynamics. From the mathematical point of view, Boltzmann entropy equation cannot be applied in the unification of classical thermodynamics. For this reason, it is necessary to use other views of entropy that have a common basis with Boltzmann entropy equation. The quasi-statistical approach, which has a common basis as the Boltzmann entropy equation, also provides the necessary conditions from a mathematical point of view. In this case, the unification of the first and second laws of thermodynamics using Boltzmann statistical perspective leads to the formation of a deep link between the classical expressions of the first and second laws with the approach of statistical physics. Also, the unified expression of the second law rewrites it as an equality, which brings a direct place in the analysis of problems for this law.

Since we were looking for a general thermodynamically unification of the first and second laws of classical thermodynamics, we considered the energy generation function as the integrator function, and also extracted the considered integrator function in a general and completely thermodynamically expression using the quasi-statistical

perspective of entropy. Finally, two innovative general thermodynamically unified equations were extracted from the unification of first and second laws of classical thermodynamics. In the following, the very important issue of the general thermodynamically expression of the second law was pursued, and in fact, the second law in its general thermodynamically unified expression was established as an equality. Finally, it is important to be noted that the unified Eqs. (15)-(17) are both mathematically and physically equivalent, and depending on our needs for analyzing a particular problem, either of them can be used.

Established novel Eqs. (15)-(17) have the general structure of unified thermodynamics. According to energy structure theory, these equations are required to satisfy the necessary and sufficient conditions of energy structure equation as well as the compatibility conditions. Eqs. (15)-(17) clearly satisfy the desired conditions in references [29, 34].

Acknowledgements:

We sincerely thank Dr. Mehran Moradi and Dr. Mahmoud Hemami, from Department of Mechanical Engineering of Isfahan University of Technology, for their countless scientific and research support. We would also like to thank Dr. HP. Beyranvand, from Faculty of Chemistry of University of Kashan, for her sincere cooperation. Finally, we would like to express our best appreciation to Mrs. Zahra Amini, from Department of Mathematics of Andishmand-Lahijan Non-profit Institution as a branch of Gilan University, for her best possible cooperation in the field of relevant mathematical equations and also in compiling the results presented here.

Nomenclature

U : Internal energy [J]

Q : Heat transfer [J]

W : Work [J]

k_{MS} : Universal constant of quasi-statistical entropy

T : Temperature [K]

s : Entropy of the system [J/K]

Greek Letters

g : Entropy generation function [J/K]

h : Irreversibility [J/K]

References:

- [1] R. Talman, *Geometric Mechanics: Toward a Unification of Classical Physics*, John Wiley & Sons, New York, 2007.
- [2] I. Dmytro, et al., "Mechanical properties of magneto-sensitive elastomers: unification of the continuum-mechanics and microscopic theoretical approaches," *Soft Matter*, vol. 10, no. 13, pp. 2213-2225, 2014.
- [3] M. Prugovecki, *Stochastic quantum mechanics and quantum spacetime: A consistent unification of relativity and quantum theory based on stochastic spaces*, vol. 4, Dordrecht, Netherlands: Kluwer Academic, 1984.
- [4] A. Rajat, and A. Acharya, "A unification of finite deformation J2 Von-Mises plasticity and quantitative dislocation mechanics," *Journal of the Mechanics and Physics of Solids*, vol. 143, 2020, Art. no 104050.
- [5] E. Haug, "Rethinking the foundation of physics and its

- relation to quantum gravity and quantum probabilities: Unification of gravity and quantum mechanics," *Preprints*, Dec. 24, 2020. [Online]. Available: <https://www.preprints.org/manuscript/202012.0483/v2>
- [6] KH. Anthony, "Unification of Continuum-Mechanics and Thermodynamics by Means of Lagrange-Formalism—Present Status of the Theory and Presumable Applications," *Arch. Mech.*, vol. 41, no. 4, pp. 511-534, 1989.
- [7] N. Patrizio, et al., "A unifying perspective: the relaxed linear micromorphic continuum," *Continuum Mechanics and Thermodynamics*, vol. 26, pp. 639-681, 2014.
- [8] P. Edvige, and G. Saccomandi, "On universal relations in continuum mechanics," *Continuum Mechanics and Thermodynamics*, vol. 9, pp. 61-72, 1997.
- [9] L. Boltzmann, "The second law of thermodynamics," *Theoretical physics and philosophical problems: selected writings*, Springer, Dordrecht, vol. 5, pp. 13-32, 1974.
- [10] L. Elliott, and J. Yngvason, "The physics and mathematics of the second law of thermodynamics," *Physics Reports*, vol. 310, no. 1, pp. 1-96, 1999.
- [11] V. Čápek, and D. P. Sheehan, *Challenges to the second law of thermodynamics*, Dordrecht: Springer, vol. 146, 2005.
- [12] S. Udo, "First and second law of thermodynamics at strong coupling," *Physical review letters*, vol. 116, no. 2, p. 020601, 2016.
- [13] B. Fernando, et al., "The second laws of quantum thermodynamics," *Proceedings of the National Academy of Sciences*, vol. 112, no. 11, pp. 3275-3279, 2015.
- [14] T. Z. Kalanov, "On the correct formulation of the first law of thermodynamics," *APS April Meeting Abstracts*, pp. D1-055, 2006.
- [15] J. Srinivasan, "Sadi Carnot and the second law of thermodynamics," *Resonance*, vol. 6, no. 11, pp. 42-48, 2001.
- [16] T. W. Xue, and Z. Y. Guo, "What is the real Clausius statement of the second law of thermodynamics?," *Entropy*, vol. 21, no. 10, 2019, Art. no. 926.
- [17] M. J. Klein, "Gibbs on Clausius," *Historical Studies in the Physical Sciences*, vol. 1, pp. 127-149, 1969.
- [18] G. Yongwan, W. Kim, and SH. Yi, "The first law of thermodynamics in Lifshitz black holes revisited," *Journal of High Energy Physics*, vol. 2014, no. 7, pp. 1-15, 2014.
- [19] S. Goldstein, et al., "Gibbs and Boltzmann entropy in classical and quantum mechanics," *Statistical mechanics and scientific explanation: Determinism, indeterminism and laws of nature*, pp. 519-581, 2020.
- [20] T. Constantino, "Entropy," *Encyclopedia*, vol. 2, no. 1, pp. 264-300, 2022.
- [21] H-J. Borchers, "Some remarks on the second law of thermodynamics," *Reports on mathematical physics*, vol. 22, no. 1, pp. 29-48, 1985.
- [22] Y. Hsu-Chieh, "Remark on the second law of thermodynamics," *American Journal of Physics*, vol. 52, no. 8, pp. 720-723, 1984.
- [23] S. Goldstein, et al., "Gibbs and Boltzmann entropy in classical and quantum mechanics," *Statistical mechanics and scientific explanation: Determinism, indeterminism and laws of nature*, pp. 519-581, 2020.
- [24] A. Wehrl, "General properties of entropy," *Rev. Mod. Phys.*, vol. 50, no. 2, pp. 221-260, 1978.
- [25] S. Shahsavari, and M. Moradi, "A New Approach to the Energy Conservation Principle and Physical Systems," Ph.D. dissertation, Department of Mechanical Engineering, Isfahan University of Technology, Isfahan, Iran, 2022.
- [26] S. Shahsavari, and M. Moradi, "A General Solution to the Different Formulations of the Second Law of Thermodynamics," *Journal of Advanced Research in Fluid Mechanics and Thermal Sciences*, vol. 82, no. 2, pp. 61-71, 2021.
- [27] T. Constantino, "Some comments on Boltzmann-Gibbs statistical mechanics," *Chaos, Solitons & Fractals*, vol. 6, pp. 539-559, 1995.
- [28] G. Sheldon, and J. L. Lebowitz, "On the (Boltzmann) entropy of non-equilibrium systems," *Physica D: Nonlinear Phenomena*, vol. 193, no. 1, pp. 53-66, 2004.
- [29] S. Shahsavari, et al. "A Quasi-Statistical Approach to the Boltzmann Entropy Equation Based on a Novel Energy Conservation Principle," *Journal of Advanced Research in Fluid Mechanics and Thermal Sciences*, vol. 101, no. 2, pp. 99-110, 2023.
- [30] N. Henmei, "Unified Mechanics on Thermodynamics, Classical Mechanics, Quantum Mechanics," 2024, *arXiv:2408.06005*.
- [31] G. N. Hatsopoulos, and E. P. Gyftopoulos, "A unified quantum theory of mechanics and thermodynamics. Part IIa. Available energy," *Foundations of Physics*, vol. 6, no. 2, pp. 127-141, 1976.
- [32] J. R. Tame, *Approaches to entropy*, Springer Singapore, pp. 115-138, 2019.
- [33] A. G. Rajan, "Microcanonical Statistical Mechanics of a Nonideal Fluid: A Pedagogical Approach to Obtain the Combined First and Second Law of Thermodynamics," *ChemRxiv*, 10.26434/chemrxiv-2021-3kmnc-v2, 2021. [Online]. Available: <https://doi.org/10.26434/chemrxiv-2021-3kmnc-v2>. [Accessed: Feb. 25, 2025].
- [34] S. Shahsavari and S. M. A. Boutorabi, "Energy Structure Theory: A General Unified Thermodynamics Theory," *International Journal of Thermodynamics*, vol. 26, no. 3, pp. 47-62, 2023.
- [35] M. Van der and M. F. Singer, *Galois theory of linear differential equations*. Berlin, Germany: Springer, 2012.